Topology and Symmetry in Weakly and Strongly Correlated Electronic Systems

by

Heqiu Li

A dissertation submitted in partial fulfillment
of the requirements for the degree of
Doctor of Philosophy
(Physics)
in The University of Michigan
2021

Doctoral Committee:

Associate Professor Kai Sun, Chair
Associate Professor Emanuel Gull
Professor Lu Li
Associate Professor Xiaoming Mao
Assistant Professor Serife Tol

Heqiu Li

heqiuli@umich.edu

ORCID iD: 0000-0003-3580-5506

ACKNOWLEDGEMENTS

First of all, I would like to express my gratitude to my supervisor Professor Kai Sun, for his generous support and guidance in my research over the past five years. He is a great supervisor who is willing to spend hours of time discussing with his students. His insightful ideas and comments in the discussion motivated me greatly. He has a broad knowledge of many different topics in condensed matter, which broadens my view and has a profound impact on me. During the research projects that I worked with him, even if I find a negative result that does not support our initial idea, with his broad knowledge he can find useful implications from this result on another field of physics in which the result becomes valuable. In this way the negative result is turned positive, and my research does not run into a dead end. His guidance and advice are crucial for me to proceed through the doctoral program.

My sincere thanks are also given to Dr. Shizeng Lin at Los Alamos National Laboratory. The collaboration with him opens up a new research area for me, and it greatly enhanced my knowledge and skills. Many thanks are also given to Professor Liuyan Zhao at University of Michigan, Ann Arbor. I learned a lot of knowledge about experiments through the discussions with her. Her group seminar provides a wonderful opportunity for me to practice introducing my work to people in a different area of physics, which improves my skills of presentation. I also thank Dr. Chen Fang at the Institute of Physics, Chinese Academy of Sciences. His creative works inspired me greatly in my research, and I benefited a lot through the discussion with him.

I am grateful to Professor Emanuel Gull, Lu Li, Xiaoming Mao and Serife Tol

for being the members of my dissertation committee. Through the discussion and collaboration with Professor Tol and the people in her group, Hrishikesh Danawe and Hasan Al Ba'ba'a, I gained more knowledge on topological elastic systems, which has broadened my knowledge and benefited me greatly. I also thank Umesh Kumar at Los Alamos National Laboratory. I learned many useful numerical techniques through the discussion and collaboration with him.

I also thank my high school physics teachers, Meiqing Deng, Wenli Cheng and Fuguo Lü. I found my interest in physics through their guidance in the early days, and they played important roles in my career path.

Finally, I would like to sincerely thank my parents for their selfless care and support in my life. Their love and support shaped who I am, and made it possible for me to pursuit my dream in physics.

TABLE OF CONTENTS

LIST OF FIGURES

Figure

LIST OF APPENDICES

Appendix

ABSTRACT

This thesis studies topological phases in various electronic crystalline systems with a focus on the interplay between symmetry and topology, including the non-interacting topological insulators, higher-order topological insulators, topological semimetals as well as the strongly correlated systems with intrinsic topological order. First, we show that when the symmetry of the system is low, the symmetry representation of energy bands may not be sufficient to determine the topological index, but the symmetry can still be utilized to define a gauge-invariant quantity, which provides a gauge-independent way to compute the Z_2 topological index of topological insulators. Second, we proposed a generalization of the famous Fu-Kane-Mele Pfaffian formula from Z_2 topological insulators to higher-order topological insulators, which allows many important conclusions that have been well known for Z_2 topological insulators to be generalized to higher-order topological insulators. This generalization is made possible via a linear superposition of symmetry operator. Third, we proposed a diagnosis scheme for topological nodal lines with nontrivial monopole charge based on point group representations. This method predicts novel cage-like nodal structures around high-symmetry lines in the Brillouin zone beyond previous diagnosis schemes which require high-symmetry lines to be gapped. Lastly, we studied strongly correlated topological phases in twisted Moire systems and proposed to realize fractional Chern insulators in twisted bilayer transition metal dichalcogenides.

CHAPTER I

Introduction

Topology characterizes the properties that are invariant under continuous deformation. Symmetry is an important ingredient in the study of topological materials. The Hamiltonian of topological insulators cannot be adiabatically deformed to the atomic insulators without closing the band gap or breaking the symmetry. In this chapter, I will give an introduction to these basic knowledge on weakly correlated topological phases. The strongly correlated topological phases are discussed in Chapter V.

1.1 Bloch waves in tight-binding approximation

The topological properties of crystals with negligible electron interaction can be described within band theory. In this section I will formulate the band structure using the tight-binding approximation. Consider a lattice with discrete translational symmetry whose unit cells are labeled by Bravais lattice vector $\boldsymbol{R}$. Suppose there are M distinct electronic states $\varphi_j(\boldsymbol{r}-\boldsymbol{R}-\boldsymbol{\delta}_j)$ inside each unit cell located at sites $\boldsymbol{R}+\boldsymbol{\delta}_j$ respectively, where $1 \leq j \leq M$ and $\boldsymbol{\delta}_j$ is inside the unit cell. Here the index j contains all the degrees of freedom inside a unit cell including sublattice, orbit, spin, etc. Each atomic orbital φ_j is an eigenstate of atomic Hamiltonian at site $\boldsymbol{R}+\boldsymbol{\delta}_j$. In the crystalline environment, with the finite overlap between different atomic orbits,

electrons can tunnel through different sites and the atomic energy levels evolve into energy bands. Since the atomic orbitals φ_j are not orthogonal in general, we need to orthogonalize them to construct the building blocks of tight-binding model. This is achieved by the Löwdin functions ϕ_j defined as [1, 2]:

$$\phi_j\left(\boldsymbol{r}-\boldsymbol{R}-\boldsymbol{\delta}_j\right)=\sum_{j',\boldsymbol{R}'}\varphi_{j'}\left(\boldsymbol{r}-\boldsymbol{R}'-\boldsymbol{\delta}_{j'}\right)\left[\Delta^{-1/2}\right]_{j'\boldsymbol{R}',j\boldsymbol{R}}. \tag{1.1}$$

$$\Delta_{j'\boldsymbol{R}',j\boldsymbol{R}}=\int d^dr\varphi^*_{j'}\left(\boldsymbol{r}-\boldsymbol{R}'-\boldsymbol{\delta}_{j'}\right)\varphi_j\left(\boldsymbol{r}-\boldsymbol{R}-\boldsymbol{\delta}_j\right). \tag{1.2}$$

The Löwdin functions ϕ_j are localized as well, and they satisfy the orthogonality condition:

$$\int d^dr\phi^*_{j'}\left(\boldsymbol{r}-\boldsymbol{R}'-\boldsymbol{\delta}_{j'}\right)\phi_j\left(\boldsymbol{r}-\boldsymbol{R}-\boldsymbol{\delta}_j\right)=\delta_{\boldsymbol{R},\boldsymbol{R}'}\delta_{j,j'}. \tag{1.3}$$

To construct tight-binding model, We can define a set of Bloch-like functions $\eta_{\boldsymbol{k},j}(\boldsymbol{r})$ from Löwdin functions:

$$\eta_{k,j}(\boldsymbol{r})=\frac{1}{\sqrt{N_c}}\sum_{\boldsymbol{R}}\phi_j(\boldsymbol{r}-\boldsymbol{R}-\boldsymbol{\delta}_j)e^{i\boldsymbol{k}\cdot(\boldsymbol{R}+\boldsymbol{\delta}_j)} \tag{1.4}$$

$$\int d^dr\eta^*_{\boldsymbol{k}'j'}\left(\boldsymbol{r}\right)\eta_{\boldsymbol{k},j}\left(\boldsymbol{r}\right)=\delta_{\boldsymbol{k},\boldsymbol{k}'}\delta_{j,j'}. \tag{1.5}$$

Here the summation is over all unit cells, and N_c is the number of unit cells. Eq.(1.5) comes from the orthogonality of Löwdin functions in Eq.(1.3). The η functions are eigenstates of lattice translation operator satisfying

$$\eta_{\boldsymbol{k},j}(\boldsymbol{r}+\boldsymbol{R})=\eta_{\boldsymbol{k},j}(\boldsymbol{r})e^{i\boldsymbol{k}\cdot\boldsymbol{R}}, \tag{1.6}$$

but they are not the eigenstates of Hamiltonian. The electron creation operators $c^\dagger$ for the tight-binding model in real and momentum space can be defined by:

$$\begin{aligned}
\langle \boldsymbol{r}|c^\dagger_{\boldsymbol{R}j}|0\rangle &= \langle \boldsymbol{r}|\phi_{\boldsymbol{R}j}\rangle = \phi_j(\boldsymbol{r}-\boldsymbol{R}-\boldsymbol{\delta}_j) && (1.7)\\
\langle \boldsymbol{r}|c^\dagger_{\boldsymbol{k}j}|0\rangle &= \langle \boldsymbol{r}|\eta_{\boldsymbol{k}j}\rangle = \eta_{\boldsymbol{k},j}(\boldsymbol{r}) && (1.8)\\
\{c_{\boldsymbol{R}j}, c^\dagger_{\boldsymbol{R}'j'}\} &= \delta_{\boldsymbol{R}\boldsymbol{R}'}\delta_{jj'},\ \{c_{\boldsymbol{k}j}, c^\dagger_{\boldsymbol{k}'j'}\} = \delta_{\boldsymbol{k}\boldsymbol{k}'}\delta_{jj'} && (1.9)
\end{aligned}$$

Here $|0\rangle$ is the vacuum state, $c^\dagger_{\boldsymbol{R}j}$ and $c^\dagger_{\boldsymbol{k}j}$ are related by Fourier transformation, and the momentum $\boldsymbol{k}$ is inside the first Brillouin zone (BZ). Note that the validity of the anticommutation in Eq.(1.9) requires the orthogonality in Eq.(1.3) and (1.5). With the definition of creation operators above, we are in position to construct the second-quantized Hamiltonian for the tight-binding model:

$$\begin{aligned}
\hat{H} &= \sum_{\boldsymbol{k},j,j'} c^\dagger_{\boldsymbol{k}j} H(\boldsymbol{k})_{jj'} c_{\boldsymbol{k}j'} && (1.10)\\
&= \sum_{\boldsymbol{R},\boldsymbol{R}',j,j'} c^\dagger_{\boldsymbol{R}j} H^{\boldsymbol{R}\boldsymbol{R}'}_{jj'} c_{\boldsymbol{R}'j'} && (1.11)\\
H^{\boldsymbol{R}\boldsymbol{R}'}_{jj'} &= \langle \phi_{\boldsymbol{R}j}|\hat{H}|\phi_{\boldsymbol{R}'j'}\rangle && (1.12)\\
H(\boldsymbol{k})_{jj'} &= \langle \eta_{\boldsymbol{k}j}|\hat{H}|\eta_{\boldsymbol{k}j'}\rangle && (1.13)
\end{aligned}$$

The Hamiltonian is diagonal in $\boldsymbol{k}$ because $\hat{H}$ preserves lattice translational symmetry. The $H(\boldsymbol{k})$ in Eq.(1.13) is an $M \times M$ matrix defined in the first BZ. It can be diagnonalized to give the energy levels and eigenstates. Denote the nth eigenstate of $H(k)$ as a $M \times 1$ column vector $u_n(k)$ satisfying

$$H(\boldsymbol{k})u_n(\boldsymbol{k}) = E_{\boldsymbol{k},n}u_n(\boldsymbol{k}), \tag{1.14}$$

and let $u_n(k)_j$ be the jth component of this vector. The Hamiltonian can be rewritten as:

$$H(\boldsymbol{k})_{jj'} = \sum_n u_n(\boldsymbol{k})_j E_{\boldsymbol{k},n} u_n^*(\boldsymbol{k})_{j'} \tag{1.15}$$

$$\hat{H} = \sum_{\boldsymbol{k},j,j',n} c_{\boldsymbol{k}j}^\dagger u_n(\boldsymbol{k})_j E_{\boldsymbol{k},n} u_n^*(\boldsymbol{k})_{j'} c_{\boldsymbol{k}j'} \tag{1.16}$$

$$= \sum_{\boldsymbol{k},n} \psi_{\boldsymbol{k}n}^\dagger E_{\boldsymbol{k},n} \psi_{\boldsymbol{k}n} \tag{1.17}$$

Here $\psi_{\boldsymbol{k}n}^\dagger = \sum_j c_{\boldsymbol{k}j}^\dagger u_n(\boldsymbol{k})_j$ is the creation operator for Bloch states which are eigenstates of the Hamiltonian. The Bloch wave functions in real space are

$$\psi_{\boldsymbol{k},n}(\boldsymbol{r}) = \langle \boldsymbol{r}|\psi_{\boldsymbol{k},n}\rangle = \langle \boldsymbol{r}|\psi_{\boldsymbol{k}n}^\dagger|0\rangle = \sum_j \eta_{\boldsymbol{k}j}(\boldsymbol{r}) u_n(\boldsymbol{k})_j, \tag{1.18}$$

which satisfiy

$$\psi_{\boldsymbol{k},n}(\boldsymbol{r}+\boldsymbol{R}) = e^{i\boldsymbol{k}\cdot\boldsymbol{R}} \psi_{\boldsymbol{k},n}(\boldsymbol{r}). \tag{1.19}$$

To study the topological properties of the system, it is important to investigate its behaviour when momentum $\boldsymbol{k}$ is increased by a reciprocal lattice vector $\boldsymbol{G}$. The Hamiltonian $\hat{H}$ is invariant under the group of lattice translation $\{\hat{T}_{\boldsymbol{R}}\}$, hence each eigenstate of $\hat{H}$ can be labeled by a crystalline momentum $\boldsymbol{k}$ with translation eigenvalue $e^{i\boldsymbol{k}\cdot\boldsymbol{R}}$. The number of distinct $\boldsymbol{k}$ is the same as the number of elements in group $\{\hat{T}_{\boldsymbol{R}}\}$, which is also the number of distinct $\boldsymbol{k}$ points in the BZ. Therefore, the Bloch states with $\boldsymbol{k}$ outside BZ are not distinct from those with momentum $\boldsymbol{k}' = \boldsymbol{k} + \boldsymbol{G}$ inside BZ, and we have the freedom to identify the states at $\boldsymbol{k}$ and $\boldsymbol{k}+\boldsymbol{G}$, leading to

$$\psi_{\boldsymbol{k},n}(\boldsymbol{r}) = \psi_{\boldsymbol{k}+\boldsymbol{G},n}(\boldsymbol{r}) \tag{1.20}$$

The transformation of the other quantities under a shift by $\boldsymbol{G}$ can be inferred from their definitions:

$$\begin{aligned} \eta_{\boldsymbol{k}+\boldsymbol{G},j}(\boldsymbol{r}) &= e^{i\boldsymbol{G}\cdot\boldsymbol{\delta}_j}\eta_{\boldsymbol{k}}(\boldsymbol{r}) \\ H(\boldsymbol{k}+\boldsymbol{G}) &= V(\boldsymbol{G})H(\boldsymbol{k})V^{\dagger}(\boldsymbol{G}) \\ u_n(\boldsymbol{k}+\boldsymbol{G}) &= V(G)u_n(\boldsymbol{k}) \\ V(\boldsymbol{G})_{jj'} &= e^{-i\boldsymbol{G}\cdot\boldsymbol{\delta}_j}\delta_{jj'} \end{aligned} \tag{1.21}$$

The above equations show that the matrix of Hamiltonian $H(\boldsymbol{k})$ is not periodic in the BZ. However, to investigate the topological properties it is desirable to formulate the Hamiltonian as a periodic function in the BZ torus. This can be achieved by redefining the η function in Eq.(1.4) by multiplying $e^{-i\boldsymbol{k}\cdot\boldsymbol{\delta}_j}$:

$$\eta_{\boldsymbol{k},j}(\boldsymbol{r}) = \langle \boldsymbol{r}|c^{\dagger}_{\boldsymbol{k},j}|0\rangle = \frac{1}{\sqrt{N_c}}\sum_{\boldsymbol{R}}\phi_j(\boldsymbol{r}-\boldsymbol{R}-\boldsymbol{\delta}_j)e^{i\boldsymbol{k}\cdot\boldsymbol{R}} \tag{1.22}$$

This amounts to a transformation in the orbital space $c^{\dagger}_{\boldsymbol{k}j} \rightarrow c^{\dagger}_{\boldsymbol{k}j}e^{-i\boldsymbol{k}\cdot\boldsymbol{\delta}_j}$. Using this new definition, all the equations between Eq.(1.5) and (1.20) remain the same, and the only change is in Eq.(1.21), which becomes:

$$\begin{aligned} \eta_{\boldsymbol{k}+\boldsymbol{G},j}(\boldsymbol{r}) &= \eta_{\boldsymbol{k}}(\boldsymbol{r}) \\ H(\boldsymbol{k}+\boldsymbol{G}) &= H(\boldsymbol{k}) \\ u_n(\boldsymbol{k}+\boldsymbol{G}) &= u_n(\boldsymbol{k}) \end{aligned} \tag{1.23}$$

Therefore, the Hamiltonian $H(\boldsymbol{k})$ and wave functions $u_n(\boldsymbol{k})$ becomes periodic in the BZ. This enables us to regard the space spanned by wave functions together with the Brillouin zone as a fibre bundle whose base space is the BZ torus. Then the classification of topological phases can be converted to the study of topology in fibre bundles.

Both the conventions in Eq.(1.21) and (1.23) are widely used in the literature. For the discussion of topological phases, we usually require the Hamiltonian to be periodic in the Brillouin zone, and it will be more convenient to work in the convention of Eq.(1.22) and (1.23). We will use this convention unless otherwise mentioned.

1.2 Symmetry in band theory

There are many symmetries that can protect a topological phase, such as time-reversal symmetry, particle-hole symmetry, and many crystalline symmetries, etc. When the system has a symmetry $\hat{S}$, the symmetry operator commutes with the second-quantized Hamiltonian $\hat{H}$:

$$\hat{S}\hat{H}\hat{S}^{-1} = \hat{H} \tag{1.24}$$

The symmetry will put a constraint to the form of allowed Hamiltonian and wave functions, which has significant effects on the topological classification of the system.

1.2.1 Time-reversal symmetry

Time-reversal symmetry $\hat{T}$ has the effect of flipping the direction of time evolution, i.e., $\hat{T}\hat{U}(t)\hat{T}^{-1} = \hat{U}(-t),\ \hat{U}(t) = e^{-i\hat{H}t}$. If the system has time-reversal symmetry, then the Hamiltonian $\hat{H}$ in Eq.(1.10) satisfies

$$\hat{T}\hat{H}\hat{T}^{-1} = \hat{H} \tag{1.25}$$

These requirements show that time-reversal is an antiunitary operator that changes i to $-i$. The action of time-reversal operator on the electron creation/annihilation

operators are given by [3]

$$\hat{T}c^{\dagger}_{\boldsymbol{k},j}\hat{T}^{-1}=\sum_{j'}c^{\dagger}_{-\boldsymbol{k},j'}(U_T)_{j'j},\quad \hat{T}c_{\boldsymbol{k},j}\hat{T}^{-1}=\sum_{j'}(U^{\dagger}_T)_{jj'}c_{-\boldsymbol{k},j'},\quad \hat{T}i\hat{T}^{-1}=-i \tag{1.26}$$

Here U_T is an $M\times M$ unitary matrix. According to Eq.(1.10), time-reversal symmetry put a constraint on the first-quantized Hamiltonian $H(\boldsymbol{k})$:

$$U_T H(\boldsymbol{k})^* U_T^{\dagger}=H(-\boldsymbol{k}) \tag{1.27}$$

We can also define the first-quantized time-reversal operator $T=U_T K$ that acts on $H(\boldsymbol{k})$, where K is complex conjugation. Then Eq.(1.27) can be written compactly as

$$TH(\boldsymbol{k})T^{-1}=H(-\boldsymbol{k}) \tag{1.28}$$

It can be further shown that the square of time-reversal operator can only be ± 1. By definition, when time-reversal is acted twice on any quantum state it should produce the same quantum state up to a phase. Therefore, $T^2=U_T U_T^*=e^{i\theta}\mathbf{1}$. Then $e^{i\theta}T=T^2T=T^3=TT^2=Te^{i\theta}=e^{-i\theta}T$, which leads to $e^{i\theta}=e^{-i\theta}$ and $e^{i\theta}=\pm 1$.

The square of time-reversal operator being ± 1 is deeply related to the spin of the system. If the system has half-odd integer spin, then $T^2=-1$. If the system is spinless or has integer spin, then $T^2=+1$. Therefore, for electronic materials with significant spin-orbit coupling, we have $T^2=-1$. However, when spin-orbit coupling is weak and the splitting between the two spin bands are negligible, we can neglect the spin degree of freedom and get an effective $T^2=+1$ system. This scenario occurs for the topological semimetals.

1.2.2 Particle-hole symmetry

The particle-hole symmetry exchanges the particle- and hole-space, and it can be formulated in a similar way as time-reversal. The action of particle-hole symmetry $\hat{\mathcal{C}}$ on the fermion creation/annihilation operators are [3]

$$\hat{\mathcal{C}} c^\dagger_{\boldsymbol{k},j} \hat{\mathcal{C}}^{-1} = \sum_{j'} (U_C^\dagger)_{jj'} c_{-\boldsymbol{k},j'}, \quad \hat{\mathcal{C}} c_{\boldsymbol{k},j} \hat{\mathcal{C}}^{-1} = \sum_{j'} c^\dagger_{-\boldsymbol{k},j'} (U_C)_{j'j}, \quad \hat{\mathcal{C}} i \hat{\mathcal{C}}^{-1} = i \tag{1.29}$$

U_C is an $M \times M$ unitary matrix. If the system has particle-hole symmetry, then following the similar procedure we have

$$\hat{\mathcal{C}} \hat{H} \hat{\mathcal{C}}^{-1} = \hat{H}, \quad \mathcal{C} H(-\boldsymbol{k}) \mathcal{C}^{-1} = -H(\boldsymbol{k}), \quad \mathcal{C} = U_C K \tag{1.30}$$

Here we have used the fact that $H(k)$ is Hermitian and the negative sign comes from the anticommutation of fermion operators. Note that unlike time-reversal, the second-quantized particle-hole operator $\hat{\mathcal{C}}$ is unitary and commutes with $\hat{H}$, but its first-quantized version $\mathcal{C}$ is antiunitary and it flips the sign of first-quantized Hamiltonian.

1.2.3 Crystalline symmetries

Crystalline symmetries are ubiquitous in solid state materials. Unlike time-reversal and particle-hole symmetries, the crystalline symmetries are unitary for both its first-quantized and second-quantized versions. They include elements of various point groups and space groups, such as rotation, mirror reflection, glide reflection, etc. They act on the real space and they can be broken by the presence of a boundary of the lattice. The collection of all the crystalline symmetries of a system forms a group, which is the system's space group $\mathcal{G}$. Every element $g \in \mathcal{G}$ can be written as $\{R|\boldsymbol{t}\}$, where R is an operation that leaves at least one point fixed, such as rotation or space inversion, and $\boldsymbol{t}$ is a pure translation. The action of g on the real space is $g\boldsymbol{r} = R\boldsymbol{r} + \boldsymbol{t}$,

and its action on a function $f(\boldsymbol{r})$ of position $\boldsymbol{r}$ is $gf(\boldsymbol{r}) = f(g^{-1}\boldsymbol{r})$. When R is the null operation E, the element $\{E|\boldsymbol{t}\}$ is a pure translation and $\boldsymbol{t}$ can only be a lattice vector. The subgroup with $\boldsymbol{t} = 0$ is a point group. If the original space group is a direct product of this point group and the group of pure lattice translation, the space group is called symmorphic, and otherwise it is called nonsymmorphic.

To study the effect of crystalline symmetries on the Hamiltonian, one can represent the symmetry by a unitary operator $\hat{g}$ that acts on the electronic creation/annihilation operators defined in Eq.(1.8):

$$\hat{g}c^\dagger_{\boldsymbol{k},j}\hat{g}^{-1} = \sum_{j'} c^\dagger_{g\boldsymbol{k},j'}(U^{\boldsymbol{k}}_g)_{j'j}, \quad \hat{g}c_{\boldsymbol{k},j}\hat{g}^{-1} = \sum_{j'}(U^{\boldsymbol{k}}_g)^\dagger_{jj'}c_{g\boldsymbol{k},j'}, \quad \hat{g}i\hat{g}^{-1} = i \tag{1.31}$$

Here $g\boldsymbol{k} = R\boldsymbol{k}$ for $g = \{R|\boldsymbol{t}\}$, and $U^{\boldsymbol{k}}_g$ is an $M \times M$ unitary matrix. When the system has $\hat{g}$ as a symmetry operation, the Hamiltonian satisfies:

$$\hat{g}\hat{H}\hat{g}^{-1} = \hat{H}, \quad U^{\boldsymbol{k}}_g H(\boldsymbol{k}) U^{\boldsymbol{k}\dagger}_g = H(g\boldsymbol{k}) \tag{1.32}$$

Eq.(1.32) imposes a relation between the wave functions at $\boldsymbol{k}$ and $g\boldsymbol{k}$. If $|u_n(\boldsymbol{k})\rangle$ is an eigenstate of $H(\boldsymbol{k})$ such that $H(\boldsymbol{k})|u_n(\boldsymbol{k})\rangle = E_{n\boldsymbol{k}}|u_n(\boldsymbol{k})\rangle$, then $U^{\boldsymbol{k}}_g|u_n(\boldsymbol{k})\rangle$ is an eigenstate of $H(g\boldsymbol{k})$ with the same energy:

$$H(g\boldsymbol{k})U^{\boldsymbol{k}}_g|u_n(\boldsymbol{k})\rangle = U^{\boldsymbol{k}}_g H(\boldsymbol{k})U^{\boldsymbol{k}\dagger}_g U^{\boldsymbol{k}}_g|u_n(\boldsymbol{k})\rangle = E_{n\boldsymbol{k}}U^{\boldsymbol{k}}_g|u_n(\boldsymbol{k})\rangle \tag{1.33}$$

This shows that the energy spectrum at symmetry-related momenta are identical. Furthermore, because $U^{\boldsymbol{k}}_g|u_n(\boldsymbol{k})\rangle$ is a normalized eigenstate at $g\boldsymbol{k}$, it can be written as a linear superposition of eigenstates at $g\boldsymbol{k}$

$$U^{\boldsymbol{k}}_g|u_n(\boldsymbol{k})\rangle = \sum_m |u_m(g\boldsymbol{k})\rangle B(\boldsymbol{k})_{mn} \tag{1.34}$$

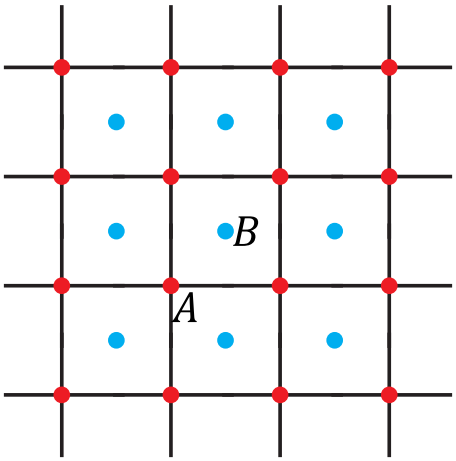

Figure 1.1: A lattice model with fourfold rotational symmetry. There are two atoms A and B in each unit cell. The atomic orbitals at A and B have C_4 eigenvalues λ_1 and λ_2 respectively.

with the coefficient matrix $B(\boldsymbol{k})$ being unitary. This means the matrix defined by $B(\boldsymbol{k})_{mn} = \langle u_m(g\boldsymbol{k})|U_g^{\boldsymbol{k}}|u_n(\boldsymbol{k})\rangle$ is unitary. This is the definition of sewing matrix, which will play an important role in the following chapters.

The explicit matrix form $U_g^{\boldsymbol{k}}$ of symmetry operator $\hat{g}$ is determined by the Löwdin functions [2]. As an example, we consider a system invariant under fourfold rotation C_4 to demonstrate how is the matrix form of symmetry operator determined by microscopic atomic orbitals. As shown in Fig.(1.1), this is a 2D square lattice with two sets of nonequivalent atomic sites at $A = \{m\hat{x}+n\hat{y}\}$ and $B = \{(m+\frac{1}{2})\hat{x}+(n+\frac{1}{2})\hat{y}\}$ respectively, where m, n are integers and the lattice constant is set to 1. The system has fourfold rotational symmetry at each atomic sites. The position of A and B sublattices within each unit cell is $\boldsymbol{\delta}_1 = 0$ and $\boldsymbol{\delta}_2 = (\frac{1}{2}, \frac{1}{2})$. Suppose the atomic states at site A (B) has C_4 eigenvalue $\lambda_1(\lambda_2)$ respectively:

$$C_4\phi_1(\boldsymbol{r}) = \phi_1(C_4^{-1}\boldsymbol{r}) = \lambda_1\phi_1(\boldsymbol{r}) \tag{1.35}$$

$$C_4\phi_2(\boldsymbol{r}) = \phi_2(C_4^{-1}\boldsymbol{r}) = \lambda_2\phi_2(\boldsymbol{r}) \tag{1.36}$$

Now we focus on the C_4 at site A, so that $C_4\boldsymbol{r} = C_4(x,y) = (-y,x)$. The action of C_4 on electron creation operators $c^\dagger_{\boldsymbol{k}j}$ in Eq.(1.8) can be derived from its action on the η function in Eq.(1.4) or Eq.(1.22). If we choose the convention in Eq.(1.4), the computation for $\eta_{\boldsymbol{k},2}$ is as follows:

$$\begin{aligned} C_4\eta_{\boldsymbol{k},2}(\boldsymbol{r}) &= C_4\frac{1}{\sqrt{N_c}}\sum_{\boldsymbol{R}}\phi_2(\boldsymbol{r}-\boldsymbol{R}-\boldsymbol{\delta}_2)e^{i\boldsymbol{k}\cdot(\boldsymbol{R}+\boldsymbol{\delta}_2)} \\ &= \frac{1}{\sqrt{N_c}}\sum_{\boldsymbol{R}}\phi_2(C_4^{-1}\boldsymbol{r}-\boldsymbol{R}-\boldsymbol{\delta}_2)e^{i\boldsymbol{k}\cdot(\boldsymbol{R}+\boldsymbol{\delta}_2)} \\ &= \frac{1}{\sqrt{N_c}}\sum_{\boldsymbol{R}}\phi_2(C_4^{-1}(\boldsymbol{r}-C_4\boldsymbol{R}-C_4\boldsymbol{\delta}_2))e^{i\boldsymbol{k}\cdot(\boldsymbol{R}+\boldsymbol{\delta}_2)} \\ &= \lambda_2\frac{1}{\sqrt{N_c}}\sum_{\boldsymbol{R}}\phi_2(\boldsymbol{r}-C_4\boldsymbol{R}-C_4\boldsymbol{\delta}_2)e^{i\boldsymbol{k}\cdot(\boldsymbol{R}+\boldsymbol{\delta}_2)} \\ &= \lambda_2\frac{1}{\sqrt{N_c}}\sum_{\boldsymbol{R}}\phi_2(\boldsymbol{r}-\boldsymbol{R}-C_4\boldsymbol{\delta}_2)e^{i(C_4\boldsymbol{k})\cdot(\boldsymbol{R}+C_4\boldsymbol{\delta}_2)}, \end{aligned} \tag{1.37}$$

where the last step replaces $\boldsymbol{R}$ by $C_4^{-1}\boldsymbol{R}$ in the summation and utilizes the identity $\boldsymbol{k}\cdot\boldsymbol{R} = C_4\boldsymbol{k}\cdot C_4\boldsymbol{R}$. Notice that $C_4\boldsymbol{\delta}_2 = \boldsymbol{\delta}_2 + \boldsymbol{R}_C$, where $\boldsymbol{R}_C = (-1,0) \in \{R\}$ is a lattice vector. Therefore, we can replace $\boldsymbol{R}$ by $\boldsymbol{R}-\boldsymbol{R}_C$ to get

$$\begin{aligned} C_4\eta_{\boldsymbol{k},2}(\boldsymbol{r}) &= \lambda_2\frac{1}{\sqrt{N_c}}\sum_{\boldsymbol{R}}\phi_2(\boldsymbol{r}-\boldsymbol{R}-\boldsymbol{\delta}_2)e^{i(C_4\boldsymbol{k})\cdot(\boldsymbol{R}-\boldsymbol{R}_C+C_4\boldsymbol{\delta}_2)} \\ &= \lambda_2\frac{1}{\sqrt{N_c}}\sum_{\boldsymbol{R}}\phi_2(\boldsymbol{r}-\boldsymbol{R}-\boldsymbol{\delta}_2)e^{i(C_4\boldsymbol{k})\cdot(\boldsymbol{R}+\boldsymbol{\delta}_2)} \\ &= \lambda_2\eta_{C_4\boldsymbol{k},2}(\boldsymbol{r}) \end{aligned} \tag{1.38}$$

The action for η_1 can be obtained similarly, leading to

$$C_4\eta_{\boldsymbol{k},1}(\boldsymbol{r}) = \lambda_1\eta_{C_4\boldsymbol{k},1}(\boldsymbol{r}), \quad C_4\eta_{\boldsymbol{k},2}(\boldsymbol{r}) = \lambda_2\eta_{C_4\boldsymbol{k},2}(\boldsymbol{r}) \tag{1.39}$$

Because $\langle\boldsymbol{r}|c^\dagger_{\boldsymbol{k},j}|0\rangle = \eta_{\boldsymbol{k},j}(\boldsymbol{r})$, Eq.(1.39) shows $\hat{g}c^\dagger_{\boldsymbol{k},1}\hat{g}^{-1} = \lambda_1 c^\dagger_{g\boldsymbol{k},1}$ and $\hat{g}c^\dagger_{\boldsymbol{k},2}\hat{g}^{-1} = \lambda_2 c^\dagger_{g\boldsymbol{k},2}$

for $g = C_4$. Then Eq.(1.31) immediately gives

$$U_g^{\boldsymbol{k}} = \begin{pmatrix} \lambda_1 & 0 \\ 0 & \lambda_2 \end{pmatrix}, \quad g = C_4, \tag{1.40}$$

which is the same as the action of symmetry g on the atomic orbitals.

We make several remarks here. Note that the $U_g^{\boldsymbol{k}}$ above is independent of $\boldsymbol{k}$, this corresponds to our choice of convention for η function in Eq.(1.4). If we have chosen another convention in Eq.(1.22), $U_g^{\boldsymbol{k}}$ will be changed to

$$\tilde{U}_g^{\boldsymbol{k}} = \begin{pmatrix} \lambda_1 & 0 \\ 0 & \lambda_2 e^{i\boldsymbol{k}\cdot\boldsymbol{R}_{g,2}} \end{pmatrix}, \tag{1.41}$$

where $\boldsymbol{R}_{g,2} = g\boldsymbol{\delta}_2 - \boldsymbol{\delta}_2 = (-1, 0) \in \{R\}$ is a lattice vector. Then $U_g^{\boldsymbol{k}}$ will become $\boldsymbol{k}$-dependent. However, with the latter convention the first-quantized Hamiltonian $H(\boldsymbol{k})$ will be periodic in the BZ satisfying $H(\boldsymbol{k}) = H(\boldsymbol{k} + \boldsymbol{G})$ according to Eq.(1.23), whereas in the former convention in Eq.(1.4) $H(\boldsymbol{k})$ is not periodic $H(\boldsymbol{k} + \boldsymbol{G}) = V(\boldsymbol{G})H(\boldsymbol{k})V^\dagger(\boldsymbol{G})$, as in Eq.(1.21). This conflict of making $H(\boldsymbol{k})$ periodic in the BZ and making $U_g^{\boldsymbol{k}}$ $\boldsymbol{k}$-independent for point group elements g is a consequence of the incompatibility in the lattice structure: for the lattice in Fig.(1.1) we are not able to find a unit cell that preserves the symmetry and does not contain any atoms at its boundary.

Furthermore, if g is a nonsymmorphic symmetry such as glide reflection, then $U_g^{\boldsymbol{k}}$ will contain a $\boldsymbol{k}$-dependent factor that is not invariant under $\boldsymbol{k} \to \boldsymbol{k} + \boldsymbol{G}$. This non-periodic factor comes from the fractional lattice translation, and it can lead to protected gap closing, such as the hourglass fermions [4].

1.3 Topology in weakly correlated gapped phases

Having described the formulation of band theory and symmetry operators, I will introduce the concept of topological phases. In this section I will focus on systems of weakly interacting electrons with an energy gap, e.g., topological insulators and superconductors. The notion of topology for gapless phases such as topological semimetals will be introduced in Chapter IV, and the topology for strongly correlated phases based on topological order will be introduced in Chapter V.

1.3.1 Symmetry-preserved adiabatic deformation and atomic limits

There are two important ingredients in the definition of gapped topological phases, adiabatic deformation and atomic limits. The band structure for a crystal with lattice translational symmetry can be described by the Hamiltonian $\hat{H}$ in Eq.(1.10). The system can have some symmetries that form a group $\{\hat{S}\}$ so that $\hat{S}\hat{H}\hat{S}^{-1} = \hat{H}$ as in Section 1.2 for $\hat{S} \in \{\hat{S}\}$. Let M be the total number of bands and the number of filled bands is p. Label the energies $E_n(\boldsymbol{k})$ at each momentum $\boldsymbol{k}$ in increasing order in n. If the system has a direct energy gap then $E_p(\boldsymbol{k}) < E_{p+1}(\boldsymbol{k})$ for any $\boldsymbol{k}$ in the BZ. Consider two gapped systems with Hamiltonian $\hat{H}_1$ and $\hat{H}_2$ that have the same number of bands M and filled bands p and the same symmetry $\{\hat{S}\}$. A symmetry-preserved adiabatic deformation between the two systems means a continuous map $f : [0,1] \to \{\hat{H}\}$ such that $f(0) = \hat{H}_1$ and $f(1) = \hat{H}_2$, and for any $t \in (0,1)$ the gap in Hamiltonian $f(t)$ remains finite and $f(t)$ preserves the same symmetry $\hat{S}f(t)\hat{S}^{-1} = f(t)$ for all $\hat{S} \in \{\hat{S}\}$. Symmetry-preserved adiabatic deformation defines equivalence classes. For a given set of symmetries, different Hamiltonians that can be related by symmetry-preserved adiabatic deformation are considered topologically equivalent.

The symmetry-preserved adiabatic deformation defines the criterion for topological equivalence. To distinguish between topological and trivial systems, we still need

a "trivial" reference phase so that the other phases that are not topologically equivalent to it are defined to be topological. This reference phase is the atomic limits. The atomic limits are characterized by Wannier functions $w_{\boldsymbol{R},n}(\boldsymbol{r})$ [5], which are the Fourier transform of Bloch wave functions $\psi_{\boldsymbol{k},n}(\boldsymbol{r})$ in Eq.(1.18):

$$w_{\boldsymbol{R},n}(\boldsymbol{r}) = \langle \boldsymbol{r}|w_{\boldsymbol{R},n}\rangle = \frac{1}{\sqrt{N_c}} \sum_{\boldsymbol{k}\in BZ} e^{-i\boldsymbol{k}\cdot\boldsymbol{R}} \psi_{\boldsymbol{k},n}(\boldsymbol{r}) \tag{1.42}$$

Here N_c is the number of unit cells. Wannier states are orthogonal $\langle w_{\boldsymbol{R},n}|w_{\boldsymbol{R}',n'}\rangle = \delta_{\boldsymbol{R}\boldsymbol{R}'}\delta_{nn'}$ and it satisfies $w_{\boldsymbol{R},n}(\boldsymbol{r}) = w_{0,n}(\boldsymbol{r}-\boldsymbol{R})$. For a fixed Hamiltonian, the Wannier functions are not unique because they depend on the gauge choice for the Bloch wave functions. For example, if we have chosen a different phase for each Bloch state $|\psi_{\boldsymbol{k},n}\rangle \to |\psi_{\boldsymbol{k},n}\rangle e^{i\theta_{\boldsymbol{k},n}}$, the resulting Wannier states will be changed. The maximally localized Wannier functions that are exponential localized in real space can be obtained if we can find a gauge to make the Bloch states smooth and periodic with $\boldsymbol{k}$ in the whole BZ [6].

For a given set of N Bloch bands that are isolated in energy from the other bands, if there exists a U(N) gauge transformation for these bands so that the Wannier functions obtained by them are exponentially localized in real space and preserve the symmetries, this set of bands are called Wannierizable. For a gapped system with p occupied bands, if these occupied bands are Wannierizable, then the system is in an atomic limit.

We can make a comparison between the Wannier functions and the atomic orbitals, which are also localized in real space. By the definition of Bloch functions in Eq.(1.18) and choosing the convention of η function as in Eq.(1.22) so that $H(\boldsymbol{k})$ is periodic in

the BZ, the Wannier functions can be written as

$$w_{\boldsymbol{R},n}(\boldsymbol{r}) = \langle \boldsymbol{r}|w_{\boldsymbol{R},n}\rangle = \frac{1}{\sqrt{N_c}}\sum_{\boldsymbol{k},j} e^{-i\boldsymbol{k}\cdot\boldsymbol{R}}\eta_{\boldsymbol{k},j}(\boldsymbol{r})u_n(\boldsymbol{k})_j \tag{1.43}$$

$$= \frac{1}{N_c}\sum_{\boldsymbol{k},\boldsymbol{R}',j} e^{-i\boldsymbol{k}\cdot(\boldsymbol{R}-\boldsymbol{R}')}\phi_j(\boldsymbol{r}-\boldsymbol{R}'-\boldsymbol{\delta}_j)u_n(\boldsymbol{k})_j \tag{1.44}$$

Here ϕ is the Löwdin function in Eq.(1.1) which is the orthogonalized atomic orbitals. $u_n(\boldsymbol{k})$ is the eigenvector of the first-quantized Hamiltonian $H(\boldsymbol{k})$, which is a M-component column vector satisfying $H(\boldsymbol{k})u_n(\boldsymbol{k}) = E_{\boldsymbol{k},n}u_n(\boldsymbol{k})$ as in Eq.(1.14). In a fully atomic limit where there is no coupling between different atomic orbitals at all, $H(\boldsymbol{k})$ will be diagonal and its eigenstates can be chosen to be $u_n(\boldsymbol{k})_j = \delta_{nj}$. Then Eq.(1.44) leads to $w_{\boldsymbol{R},n}(\boldsymbol{r}) = \phi_n(\boldsymbol{r}-\boldsymbol{R}-\boldsymbol{\delta}_n)$, i.e., the Wannier function reduces to atomic orbitals in the zero-coupling limit. However, in a generic system with finite hopping between orbitals, the wave function $u_n(\boldsymbol{k})$ acquires $\boldsymbol{k}$-dependence to make Wannier functions distinct from atomic orbitals. In particular, if the $\boldsymbol{k}$-dependence in $u_n(\boldsymbol{k})$ is nontrivial so that it can no longer be chosen to be smooth and periodic in the BZ, the Wannier function will no longer be exponentially localized in real space. This happens when the system is topologically nontrivial.

1.3.2 Definition of topological phases

The definition of topologically nontrivial phase given by Ref. [7] is: if a gapped system cannot be connected to any atomic limits by a symmetry-preserved adiabatic deformation (continuous deformation of Hamiltonian without closing the gap or breaking the symmetry), then this system is topological.

Much information can be obtained from this definition. It indicates the robustness of topological phases: a topological phase will remain topological after a small perturbation is added, unless the perturbation is large enough to close the energy gap, or the perturbation breaks the symmetry. Therefore the topology is protected

by this symmetry. If one try to construct maximally localized Wannier functions for the filled bands of a topological phase, the obstructions can occur in two ways: (1) the Wannier functions fail to be exponentially localized in real space, or (2) the Wannier functions are exponentially localized by they break the symmetry.

The phases that are not topological can be adiabatically deformed to an atomic limit in which the electron Wannier functions are exponentially localized in a symmetry-preserving way. However, the atomic limits are not unique, and different atomic limits cannot be connected to each other by a symmetry-preserved adiabatic deformation. In some atomic limits the Wannier functions can be localized in positions away from the atomic orbitals, and therefore they cannot be adiabatically deformed back to the zero-coupling limit in which the Wannier functions coincide with atomic orbitals. This is the obstructed atomic limits. Although this phase is not topological by definition, in the presence of symmetry it can have unique features such as quantized polarization and fractionalized corner charges [8].

1.3.3 Conditions for topology in momentum space

We can quantitatively exam in momentum space what are the conditions needed for the system to be topological. From the definition of topological phases, a trivial phase need to support exponentially localized Wannier functions that preserve the symmetries. Consider gapped M-band system with N filled bands ($N < M$). Because topological properties are not affected by the detailed dispersion relation, we can construct a flattened Hamiltonian $H_f(\boldsymbol{k})$ in which all the filled bands have the same energy while the eigenstates $u_n(\boldsymbol{k})$ of the flattened Hamiltonian remain the same as the original Hamiltonian $H(\boldsymbol{k})$, where $u_n(\boldsymbol{k})$ is a M-component column vector that represents the nth eigenstate as in Eq.(1.14). Here we choose the convention in Eq.(1.22) and (1.23) so that $H_f(\boldsymbol{k})$ and $u_n(\boldsymbol{k})$ satisfy the periodic boundary condition

in the BZ. A gauge transformation in the space of filled bands is given by

$$u_n(\boldsymbol{k}) \to u'_n(\boldsymbol{k}) = \sum_{n'=1}^{N} u_{n'}(\boldsymbol{k}) U(\boldsymbol{k})_{n'n}, \tag{1.45}$$

where $U(\boldsymbol{k})$ is any U(N) matrix. After gauge transformation, $\{u'_n(\boldsymbol{k})\}$ is also a set of well-defined eigenstates of the flattened Hamiltonian, but the Wannier functions corresponding to will be different. If there is a gauge transformation to make $\{u_n(\boldsymbol{k})\}$ smooth and periodic in the BZ, the Wannier functions will be exponentially localized, as seen from Eq.(1.43). Therefore, the absence of exponentially localized Wannier functions that preserve symmetry indicates the absence of a gauge to make $\{u_n(\boldsymbol{k})\}$ smooth and periodic in the BZ. In the language of fibre bundle, this means the vector bundle $\mathcal{E} = \bigcup_{\boldsymbol{k}\in BZ} \mathrm{Span}\,\{u_1(\boldsymbol{k}) \dots u_N(\boldsymbol{k})\}$ formed by the N filled bands is nontrivial [9].

In some symmetry-protected topological phases the construction of exponentially localized Wannier functions are possible, but they break the symmetries, i.e., they do not form a representation of the symmetry group. Therefore we need to know in what situation will the Wannier states preserve the symmetry and what are corresponding conditions in momentum space. Each Wannier state $|w_{\boldsymbol{R},n}\rangle$ has a Wannier center at $\boldsymbol{R}+\boldsymbol{r}_n$, where $\boldsymbol{R}$ is a lattice vector and r_n is within a unit cell. Consider a simple case in which the Wannier label n for $|w_{\boldsymbol{R},n}\rangle$ is not changed under some spacial symmetry S. If the Wannier states preserve symmetry S, the set $\{\boldsymbol{R}+\boldsymbol{r}_n\}$ needs to be invariant under S. Therefore S transforms $\boldsymbol{R}+\boldsymbol{r}_n$ to $\boldsymbol{R}+\boldsymbol{r}_n+\boldsymbol{R}_S$ for some lattice vector $\boldsymbol{R}_S$, i.e., $S(\boldsymbol{R}+\boldsymbol{r}_n) = \boldsymbol{R}+\boldsymbol{r}_n+\boldsymbol{R}_S$. When the Wannier label n is invariant under S, the condition that Wannier states form a representation of symmetry S is:

$$\hat{S}|w_{\boldsymbol{R},n}\rangle = \lambda_n |w_{\boldsymbol{R}+\boldsymbol{R}_S,n}\rangle \tag{1.46}$$

where λ_n is an eigenvalue of symmetry S and the hat in $\hat{S}$ means it is an opera-

tor acting on the Fock space. From Section 1.2, the action of $\hat{S}$ on electronic creation/annihilation operators and Hamiltonian is:

$$\hat{S}c^{\dagger}_{\boldsymbol{k},j}\hat{S}^{-1} = \sum_{j'} c^{\dagger}_{S\boldsymbol{k},j'}(U^{\boldsymbol{k}}_S)_{j'j} \tag{1.47}$$

Here $U^{\boldsymbol{k}}_S$ is the $M \times M$ matrix representation of symmetry S. Using Eq.(1.8), (1.43), (1.46) and (1.47) we get

$$\sum_{\boldsymbol{k},j,j'} e^{-i\boldsymbol{k}\cdot\boldsymbol{R}}\langle \boldsymbol{r}|c^{\dagger}_{S\boldsymbol{k},j'}|0\rangle (U^{\boldsymbol{k}}_S)_{j'j} u_n(\boldsymbol{k})_j \quad = \quad \lambda_n \sum_{\boldsymbol{k},j} e^{-i\boldsymbol{k}\cdot(\boldsymbol{R}+\boldsymbol{R}_S)}\langle \boldsymbol{r}|c^{\dagger}_{\boldsymbol{k},j}|0\rangle u_n(\boldsymbol{k})_j \tag{1.48}$$

The orthogonality of $c^{\dagger}_{\boldsymbol{k},j}$ leads to

$$U^{\boldsymbol{k}}_S u_n(\boldsymbol{k}) = \lambda_n e^{i\boldsymbol{k}\cdot\overline{\boldsymbol{R}}} u_n(S\boldsymbol{k}), \tag{1.49}$$

where $\overline{\boldsymbol{R}} = \boldsymbol{R} - S^{-1}\boldsymbol{R} - S^{-1}\boldsymbol{R}_S$ is some lattice vector.

Three important implications can be seen from Eq.(1.49). (1) If the Wannier functions preserve the symmetry, then the arbitrary overall phase of wave functions at $\boldsymbol{k}$ and $S\boldsymbol{k}$ are no longer independent, i.e., they need to satisfy Eq.(1.49). (2) At symmetry-invariant $\boldsymbol{k}$ points where $S\boldsymbol{k} = \boldsymbol{k}$, the wave functions are eigenvectors of symmetry operator. (3) All distinct symmetry-invariant $\boldsymbol{k}$ points share the same λ_n. This means the symmetry representations at different high-symmetry momenta are not independent, and they are related in a fixed number of ways determined by $\overline{\boldsymbol{R}}$, otherwise the Wannier functions cannot preserve the symmetry. It turns out that different $\overline{\boldsymbol{R}}$ correspond to different atomic limits, as we can see in Section(1.4.1).

We make some remarks here. Eq.(1.49) applies when label n is invariant under symmetry. In the more general cases when there are multiple symmetries that do not commute with each other, Wannier functions will form representations of the symmetry group. But the generic feature of Eq.(1.49) remains: to make the Wannier

functions preserve symmetries, the representations at high-symmetry momenta are related to each other in some fixed ways determined by the atomic limits. If the representations are incompatible with any atomic limit and the system is gapped, then the system has to be topological. This shows symmetry representations at high-symmetry momenta can be utilized to detect topological phases [7, 10].

1.4 Examples of topologically trivial and nontrivial phases

Topological phases can be characterized by topological indices, which are numbers defined for each phase that can only take discrete values. Topological indices are invariant when the Hamiltonian of the system is adiabatic deformed without closing the gap or breaking the symmetries. Therefore, if two phases have different topological indices, they cannot be topologically equivalent. In this section I will give some examples on how topological indices can be utilized to distinguish between different phases.

1.4.1 1D Polarization quantized by inversion

Consider a simple example of 1D atomic chain which has two atoms in each unit cell with alternating hopping strength, as in Fig.(1.2). This model is known as the SSH model [11]. Note that the lattice constant a is the distance between two atoms of the same type. Set the lattice constant $a = 1$ for simplicity. This system has inversion symmetry with inversion centers in the middle between two neighbouring atoms. We can choose the unit cell to preserve inversion symmetry, such as the blue or the green rectangles. If we choose the green rectangle to be the unit cell, then t is the hopping inside unit cell and t' is that between unit cells. Then the Hamiltonian

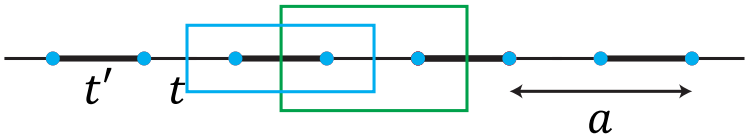

Figure 1.2: The SSH atomic chain model with two atoms in a unit cell. Inversion-symmetric unit cells can be chosen to be the green or blue rectangles.

is

$$\begin{aligned} \hat{H} &= \sum_R t c^\dagger_{R,A} c_{R,B} + t' c^\dagger_{R,B} c_{R+1,A} + h.c. \\ &= \sum_{k,j,j'} c^\dagger_{kj} H(k)_{jj'} c_{kj'} \end{aligned} \tag{1.50}$$

$$H(k) = \begin{pmatrix} 0 & t + t' e^{-ik} \\ t + t' e^{ik} & 0 \end{pmatrix} = \begin{pmatrix} 0 & h(k)^* \\ h(k) & 0 \end{pmatrix} \tag{1.51}$$

Here periodic boundary in the real space is assumed, and $h.c.$ is Hermitian conjugate. We have used the convention in Eq.(1.22) so that $H(k)$ is periodic under $k \to k + 2\pi$. The system has inversion symmetry P and chiral symmetry S:

$$P = \sigma_x, \quad PH(k)P^{-1} = H(-k) \tag{1.52}$$

$$S = \sigma_z, \quad SH(k)S^{-1} = -H(k) \tag{1.53}$$

The energy and eigenstates are

$$H(k)u_\pm(k) = E_\pm(k)u_\pm(k), \tag{1.54}$$

$$E_\pm(k) = \pm\sqrt{t^2 + t'^2 + 2tt' \cos k} \tag{1.55}$$

$$u_\pm(k) = \frac{1}{\sqrt{2}} \begin{pmatrix} t + t' e^{-ik} \\ \pm\sqrt{t^2 + t'^2 + 2tt' \cos k} \end{pmatrix} \tag{1.56}$$

Therefore, when $|t| \neq |t'|$, the system is gapped at half filling. The gapped system allows the definition of topological indices. Define the Berry connection $\mathcal{A} = -i\langle u_-(k)|\partial_k|u_-(k)\rangle$, where $|u_-(k)\rangle$ is the wave function of the lower band. With inversion and chiral symmetries, two topological indices can be defined:

$$\nu_p = \frac{1}{2\pi}\int \mathcal{A}(k)dk \mod 1 \tag{1.57}$$

$$\nu_w = \frac{1}{2\pi i}\int \partial_k \log(h(k))dk = \frac{1}{2\pi i}\int \partial_k \log(t + t'e^{ik})dk \tag{1.58}$$

Here the integral is over the 1D BZ. ν_p is the polarization of the 1D system, i.e., the physical electronic polarization in the crystal is $\boldsymbol{P} = \nu_p e\boldsymbol{a}$, where e is the electron charge. ν_p is defined module 1 because the polarization in a periodic crystal is well-defined module $e\boldsymbol{a}$. This can also be seen from the fact that under a gauge transform $u_-(k) \to u_-(k)e^{ik}$, ν_p is changed by 1 from Eq.(1.57), therefore only the module 1 part of ν_p is gauge-invariant. When the system has inversion symmetry, ν_p is quantized to 0 or $\frac{1}{2}$, hence its value cannot be changed under adiabatic deformation of the Hamiltonian without closing the gap. Without the inversion symmetry, ν_p can take any value and is no longer quantized. Therefore, ν_p is a topological index for this system that is protected by inversion symmetry. A direct computation of ν_p using Eq.(1.56) shows $\nu_p = 0$ when $|t'| < |t|$ and $\nu_p = \frac{1}{2}$ when $|t'| > |t|$.

ν_w is a winding number quantized to integers. It is well-defined for the gapped phase in which $|t| \neq |t'|$. It represents the number of times that the phase of $h(k)$ circulates the origin. $\nu_w = 1$ when $|t'| > |t|$ and $\nu_w = 0$ when $|t'| < |t|$. ν_w is a topological index only when the system has chiral symmetry. Otherwise, an additional term $b\sigma_z$ will be allowed in $H(k)$ and the spectrum will be gapped as long as $b \neq 0$. In this case, although the value of ν_w in Eq.(1.58) is still quantized to integers, it can be changed from 0 to 1 without closing the band gap when we tune the value of $|t|$ across $|t'|$. Therefore, without chiral symmetry, ν_w is not a well-defined topological

index.

1.4.1.1 Are these phases topological?

To determine whether these phases are topological, we need to exam whether they allow exponentially localized Wannier functions that preserve symmetry. When inversion and chiral symmetries are both present, ν_p and ν_w are not independent in this two-band model and they satisfy $2\nu_p = \nu_w \mod 2$. Now we will only focus on ν_p and study its implication on topology. The previous discussion has shown there are two phases that are not topologically equivalent, i.e., the $|t| > |t'|$ phase with $\nu_p = 0$ and the $|t| < |t'|$ phase with $\nu_p = \frac{1}{2}$. Note that when we write the wave functions as in Eq.(1.56), we have already chosen the wave function to be both smooth and periodic in the BZ. Therefore, the filled band in this system allows exponentially localized Wannier functions. For the Wannier functions to preserve inversion, Eq.(1.49) needs to be satisfied, which is

$$Pu_-(k) = \lambda e^{ik\overline{R}} u_-(-k) \tag{1.59}$$

for all k in the BZ and for some integer $\overline{R}$, where $\overline{R}$ is the distance that the Wannier center will be shifted under inversion. This means the eigenvalue of inversion P at high-symmetry momenta $k = 0$ and π are not independent. Suppose t and t' are positive. Denote the inversion eigenvalue for the filled band at $k = 0$ and $k = \pi$ as P_0 and P_π respectively, then Eq.(1.59) requires $P_0 = \lambda$ and $P_\pi = \lambda e^{i\pi\overline{R}}$. A direct computation using Eq.(1.56) and $P = \sigma_x$ shows

$$\begin{aligned} &P_0 = P_\pi = -1, \quad \text{if } t > t' \\ &P_0 = -1, \ P_\pi = 1, \quad \text{if } t < t' \end{aligned} \tag{1.60}$$

Therefore, for $t > t'$ Eq.(1.59) can be satisfied by $\lambda = -1, \ \overline{R} = 0$ and for $t < t'$ it can be satisfied by $\lambda = -1, \ \overline{R} = 1$. This means in both cases $t < t'$ and $t > t'$ the

Wannier functions preserve the inversion symmetry. Therefore, both of these phases are topologically trivial, and they correspond to different atomic limits. In particular, the atomic limit for $t > t'$ has a Wannier function with inversion eigenvalue $\lambda = -1$ sitting at $x = 0$ at the center of unit cell, and for $t < t'$ the Wannier function also has inversion eigenvalue -1, but it is located at $x = \frac{1}{2}$ so that under inversion its position will be shifted by $\overline{R} = 1$. This is also consistent with the physical meaning of the polarization ν_p that it is the position of Wannier center.

1.4.1.2 Unit cell dependence and edge states

The fact that the phases with $\nu_p = 0$ and $\nu_p = \frac{1}{2}$ are not fundamentally different can also be seen from the unit cell dependence of ν_p. If we chose the blue rather than the green rectangle in Fig.(1.2) as the unit cell, then the roles of t and t' will be exchanged in the new Hamiltonian $H_{new}(k)$, i.e., t' will be the hopping inside unit cells. Therefore the phases with $\nu_p = 0$ and $\frac{1}{2}$ will be flipped. However, the physical position of the Wannier center is independent of our choice of unit cell. If $t < t'$, then for the green unit cell choice we get $\nu_p = \frac{1}{2}$ so that the Wannier center is on the boundary of green unit cell; for the blue unit cell choice we will get $\nu_p = 0$ so that the Wannier center will be at the center of blue unit cells. In both cases the Wannier center is in the middle of the bounds with stronger hopping. This Wannier center polarization can lead to edge modes and edge charges when the lattice has a boundary. Assume $t < t'$ without lost of generality. Consider a lattice that is terminated on its left side, as shown in Fig.(1.3). The Wannier centers will be located in the middle of t' bounds, which are labeled in red. In Fig.(1.3) (a) there is a Wannier center outside the lattice. Because each Wannier center is shared by two unit cells, this will lead to an edge mode inside the bulk gap and a fractional charge quantized to $e/2$ located at the edge. This is an example of fractional charge protected by inversion symmetry [8]. However, in Fig.(1.3) (b) there will not be fractional charge at the edge because the

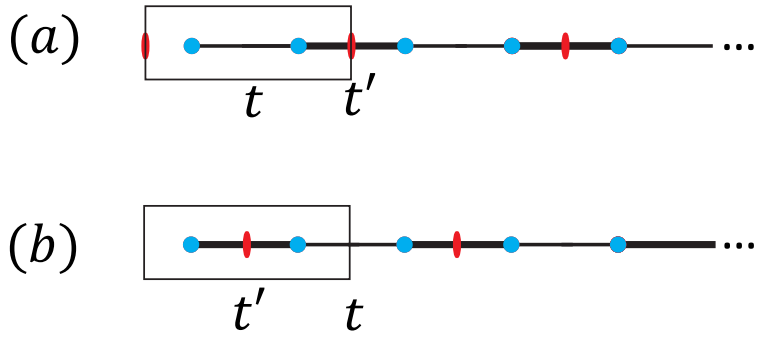

Figure 1.3: SSH model with lattice terminated at the left side. The black rectangles are unit cells and the red dots represent the position of Wannier centers. When $t < t'$, there is a edge state in (a) but not in (b).

Wannier center is fully inside the edge unit cell.

1.4.2 Chern insulators

Chern insulator is a 2D topological phase whose topology does not need any symmetries to protect. The topological index is the Chern number C whose value is quantized to integers. Chern number was originally introduced to describe the integer quantum Hall effect [12, 13] in which a 2D electronic system is under a strong magnetic field. When Chern number is nonzero, the system has gapless chiral edge modes with quantized Hall conductance $\sigma_{xy} = C\frac{e^2}{h}$. C can be nonzero only when time-reversal symmetry is broken. The strong magnetic field in the integer quantum Hall effect naturally breaks time-reversal. Without an external magnetic field, if there is other magnetic order that breaks time-reversal, quantized Hall conductance can also emerge in the quantum anomalous Hall effect [14], which can be described by Chern number as well. For a gapped system with N filled bands, the Chern number

C is defined by

$$C = \sum_{n\in occ} \frac{1}{2\pi} \int_{BZ} d^2k \mathcal{B}_n(\boldsymbol{k}) \tag{1.61}$$

$$\mathcal{B}_n(\boldsymbol{k}) = \partial_x \mathcal{A}_{y,n}(\boldsymbol{k}) - \partial_y \mathcal{A}_{x,n}(\boldsymbol{k}) \tag{1.62}$$

$$\mathcal{A}_{\mu,n}(\boldsymbol{k}) = -i\langle u_n(\boldsymbol{k})|\partial_\mu|u_n(\boldsymbol{k})\rangle,\ \mu = x, y \tag{1.63}$$

Here *occ* means the occupied bands, the partial derivatives are derivatives to momentum k_x or k_y. $\mathcal{A}$ is the Berry connection and $\mathcal{B}$ is the Berry curvature [15]. $\mathcal{A}(\boldsymbol{k})$ and $\mathcal{B}(\boldsymbol{k})$ are both periodic in the Brillouin zone. The definitions of them involve derivatives of wave functions to momentum $\boldsymbol{k}$. Since $u_n(\boldsymbol{k})$ depends on the gauge which needs not be continuous in $\boldsymbol{k}$, it is always required that when we take derivative to $\boldsymbol{k}$ we need to use a gauge that is smooth at $\boldsymbol{k}$. The value of $\mathcal{A}$ will change under a guage transform but the value of $\mathcal{B}$ is invariant:

$$|u_n(\boldsymbol{k})\rangle \to |u_n(\boldsymbol{k})\rangle e^{i\theta_{n\boldsymbol{k}}},\ \mathcal{A}_n(\boldsymbol{k}) \to \mathcal{A}_n(\boldsymbol{k}) + \nabla_{\boldsymbol{k}}\theta_{n\boldsymbol{k}},\ \mathcal{B}_n(\boldsymbol{k}) \to \mathcal{B}_n(\boldsymbol{k}) \tag{1.64}$$

Therefore C is invariant under gauge transformation. The right hand side of Eq.(1.61) is quantized to an integer as long as the integral is over a closed compact manifold without boundary and the bands inside the summation are isolated in energy with other bands. This means C is quantized to an integer as long as the energy gap separating the occupied bands and other bands remains finite. Therefore, C is a well-defined topological index that can distinguish between topologically distinct phases.

Importantly, as long as $C \neq 0$, the system cannot be adiabatically deformed to an atomic limit without closing the gap. This is because if the filled bands can be adiabatically connected to atomic limits, then there exists a gauge to make the wave functions smooth and periodic in the Brillouin zone to make the Wannier functions exponentially localized in real space. The Berry curvature can be rewritten as $\mathcal{B}_n(\boldsymbol{k}) =$

$\nabla \times \mathcal{A}_n(\boldsymbol{k})$. In the smooth gauge the Stokes theory is applicable, which leads to $C = \sum_{n\in occ} \int_{\partial BZ} \mathcal{A}_n(\boldsymbol{k}) \cdot d\boldsymbol{k}$, where ∂BZ is the boundary of Brillouin zone. However, the Brillouin zone is a torus without boundary, and this leads to $C = 0$. Therefore, atomic limits always have $C = 0$, and if $C \neq 0$ then the system is topological.

1.4.3 Z_2 topological insulator with time-reversal symmetry

For a gapped spin 1/2 system with time-reversal symmetry T in two or three dimension, the Fu-Kane-Mele (FKM) Z_2 topological index can be defined [16, 17], which characterizes the Z_2 classification of topological insulators protected by time-reversal symmetry [16, 17, 18, 19, 20, 21, 22, 23]. This index can be nontrivial in the presence of strong spin-orbit coupling. When it is nontrivial, there are topologically protected gapless boundary states that preserve time-reversal symmetry. In 2D there will be gapless helical edge state pairs where the two states in each pair propagate in opposite directions with opposite spin direction. If the spin component perpendicular to the 2D plane is conserved, the nontrivial Z_2 index leads to the quantum spin Hall effect [18, 24, 25, 26] with quantized spin Hall conductance. For 3D systems, the nontrivial Z_2 index leads to gapless surface Dirac cones in the surface Brillouin zone [19].

The definition of this index requires time-reversal symmetry. From Eq.(1.26) and (1.28), the Hamiltonian of a time-reversal-symmetric spin 1/2 system with M bands satisfies

$$TH(\boldsymbol{k})T^{-1} = H(-\boldsymbol{k}),\ T = U_T K,\ T^2 = -1 \tag{1.65}$$

Here U_T is an $M \times M$ matrix. This means if $|u_n(\boldsymbol{k})\rangle$ is an eigenstate of $H(\boldsymbol{k})$, then $T|u_n(\boldsymbol{k})\rangle$ will be an eigenstate of $H(-\boldsymbol{k})$. Therefore, $T|u_n(\boldsymbol{k})\rangle$ can be written as the superposition of eigenstates at $-\boldsymbol{k}$: $T|u_n(\boldsymbol{k})\rangle = \sum_m |u_m(-\boldsymbol{k})\rangle \omega(\boldsymbol{k})_{mn}$ and $\omega(\boldsymbol{k})$ is a unitary matrix. For a gapped system, the occupied and unoccupied bands are separated in energy, then if band n is occupied, the summation of m can be restricted

to occupied bands as well. If N bands are occupied ($N < M$), we can define a unitary $N \times N$ sewing matrix $\omega(\boldsymbol{k})$:

$$\begin{aligned} \omega(\boldsymbol{k})_{mn} &= \langle u_m(-\boldsymbol{k})|T|u_n(\boldsymbol{k})\rangle & (1.66) \\ T|u_n(\boldsymbol{k})\rangle &= \sum_{m\in occ} |u_m(-\boldsymbol{k})\rangle\omega(\boldsymbol{k})_{mn} & (1.67) \end{aligned}$$

The FKM Z_2 topological index is defined through this sewing matrix. To define the index we still need two properties of the sewing matrix. First, the sewing matrix can be made smooth and periodic in the BZ by a gauge transform. This is because the Chern number of the system is zero as enforced by time-reversal symmetry, hence exists a gauge to make the wave function smooth and periodic in the BZ. Then the sewing matrix $\omega(\boldsymbol{k})$ will be smooth and periodic as well. The second property needed for the sewing matrix is:

$$\omega(\boldsymbol{k})_{mn} = -\omega(-\boldsymbol{k})_{nm}, \tag{1.68}$$

which can be seen by

$$\begin{aligned} \omega(\boldsymbol{k})_{mn} &= \langle u_m(-\boldsymbol{k})|T|u_n(\boldsymbol{k})\rangle \\ &= \langle T^2 u_n(\boldsymbol{k})|T|u_m(-\boldsymbol{k})\rangle \\ &= -\langle u_n(\boldsymbol{k})|T|u_m(-\boldsymbol{k})\rangle \\ &= -\omega(-\boldsymbol{k})_{nm} & (1.69) \end{aligned}$$

Therefore, $\omega(\boldsymbol{k})$ is anti-symmetric when $\boldsymbol{k} = -\boldsymbol{k}+\boldsymbol{G}$, i.e., $\boldsymbol{k}$ is one of the time-reversal-invariant-momenta (TRIM). This allows us to define the Pfaffian for the sewing matrix at TRIM. The Pfaffian of an anti-symmetric matrix is a polynomial of matrix elements whose square is the determinant of that matrix. It can only be defined only for anti-symmetric matrices. Denote Pfaffian as Pf. The FKM topological index ν for the Z_2

topological insulator protected by time-reversal symmetry is given by [16, 17]

$$(-1)^{\nu} = \prod_{\boldsymbol{K}\in TRIM} \frac{\mathrm{Pf}[\omega(\boldsymbol{K})]}{\sqrt{\det[\omega(\boldsymbol{K})]}}, \tag{1.70}$$

where ν can be of 0 or 1. Eq.(1.70) requires that the gauge has been chosen such that $\omega(\boldsymbol{k})$ is smooth and periodic in the Brillouin zone, and the same branch of square root needs to be chosen for all the TRIM. Otherwise the sign ambiguity of square root will make this formula ill-defined. Because $\omega(\boldsymbol{k})$ is unitary, its determinant is always nonzero. Therefore the factor $\Delta_{\boldsymbol{K}} = \frac{\mathrm{Pf}[\omega(\boldsymbol{K})]}{\sqrt{\det[\omega(\boldsymbol{K})]}}$ is well-defined for each $\boldsymbol{K}$ and can only be ± 1.

Now we show that if $\nu = 1$ then the system is topological, i.e., it does not allow exponentially localized Wannier functions that preserve time-reversal symmetry. Due to the vanishing Chern number, one can obtain a smooth and periodic gauge so that the Wannier functions are exponentially localized. $T^2 = -1$ imposes Kramers degeneracy so that the Wannier functions should appear in pairs. To preserve time-reversal symmetry, the two Wannier functions in each pair have opposite spin orientation, and they satisfy

$$T|w_{\boldsymbol{R},1}\rangle = |w_{\boldsymbol{R},2}\rangle, \quad T|w_{\boldsymbol{R},2}\rangle = -|w_{\boldsymbol{R},1}\rangle \tag{1.71}$$

Following the same procedure that lead to Eq.(1.49), Eq.(1.71) imposes a condition on wave functions:

$$T|u_1(\boldsymbol{k})\rangle = |u_2(-\boldsymbol{k})\rangle, \quad T|u_2(\boldsymbol{k})\rangle = -|u_1(-\boldsymbol{k})\rangle, \tag{1.72}$$

where $|u_1(\boldsymbol{k})\rangle$ and $|u_2(\boldsymbol{k})\rangle$ are two bands that form each Kramers pair. Comparing with Eq.(1.66), this requires the sewing matrix $\omega(\boldsymbol{k})$ to be constant in momentum space. In this case we can always choose the branch of square root in Eq.(1.70) to make $\frac{\mathrm{Pf}[\omega(\boldsymbol{K})]}{\sqrt{\det[\omega(\boldsymbol{K})]}} = +1$ for all TRIM, then the Z_2 index will be trivial $\nu = 0$. Therefore,

to make the Wannier functions preserve time-reversal symmetry, the index must be trivial, and when $\nu = 1$ the system must be topological.

1.5 Challenges in obtaining a smooth gauge

The computation of Chern number from Eq.(1.61) requires the wave functions to be smooth so that the derivatives to $\boldsymbol{k}$ are well-defined. The Z_2 topological index protected by time-reversal symmetry in Eq.(1.70) requires the wave functions to be smooth and satisfy the periodic boundary condition $u_n(\boldsymbol{k}) = u_n(\boldsymbol{k} + \boldsymbol{G})$ in the Brillouin zone (BZ), where $\boldsymbol{G}$ is any reciprocal lattice vector. However, it is usually challenging to obtain such a smooth and periodic gauge. The challenge comes from two aspects. First, for a system with multiple occupied bands with protected band crossing, even if the crossing happens only at several $\boldsymbol{k}$ points, a smooth gauge cannot be obtained by simply adjusting the U(1) phase of each band, and it generally requires the superposition of multiple bands in the whole BZ. Second, although a smooth gauge can be obtained locally in a contractible open set using parallel transport, this gauge is generally not smooth in the BZ torus. I will illustrate this by an example as follows.

Consider a gapped one-dimensional system with two occupied bands, and the Hamiltonian is

$$H(k) = \begin{pmatrix} 3 & 0 & 0 \\ 0 & 0 & 1 - e^{ik} \\ 0 & 1 - e^{-ik} & 0 \end{pmatrix} \tag{1.73}$$

This Hamiltonian is block diagonal, and the form of its lower block is the gap closing point of the SSH model in Section 1.4.1 with $t = -t'$. The energies and the

corresponding eigenstates are given by:

$$E_1(k) = 2\sin\frac{k}{2},\ u_1(k) = \frac{e^{i\phi_1(k)}}{\sqrt{2}}\begin{pmatrix} 0 \\ 1 \\ e^{-ik/2} \end{pmatrix}$$

$$E_2(k) = -2\sin\frac{k}{2},\ u_2(k) = \frac{e^{i\phi_2(k)}}{\sqrt{2}}\begin{pmatrix} 0 \\ -1 \\ e^{-ik/2} \end{pmatrix}$$

$$E_3(k) = 3,\ u_3(k) = \begin{pmatrix} e^{i\phi_3(k)} \\ 0 \\ 0 \end{pmatrix} \tag{1.74}$$

The system has two occupied bands $E_1(k)$ and $E_2(k)$ that cross at $k = 0$, and are separated in energy with the unoccupied band E_3. $\phi_{1,2,3}(k)$ represents the arbitrary overall U(1) phase for each wave function.

Now suppose we want to find a gauge that is smooth and periodic in the BZ for the two occupied bands. We can choose $\phi_1(k)$ and $\phi_2(k)$ to be smooth in k so that each wave function will be smooth as well. However, at the band crossing point $k = 0$, we will face different choices when deciding which band does each wave function belong to. The dispersion of the two occupied bands are shown in Fig.(1.4). Four wave functions near $k = 0$ are labeled in Fig.(1.4) (a), where ϵ is a small positive number. To make the wave functions smooth at $k = 0$, we need to assign A and D in Fig.(1.4) (a) to be in one band, and assign B and C to be in another band. This results in the gauge choice in Fig.(1.4) (b), which is smooth at $k = 0$ but it does not satisfy the periodic boundary condition in the BZ. If we have made the other choice to assign A and B in one band, then it leads to Fig.(1.4) (c) in which the bands satisfy the periodic boundary condition but they are not smooth at $k = 0$. Therefore, a smooth and periodic gauge cannot be obtained by adjusting the U(1)

phase of each wave function. However, if we allow the superposition of the two bands and choose $\phi_1(k) = \phi_2(k) = 0$, a smooth and periodic gauge with $\tilde{u}_1(k)$ and $\tilde{u}_2(k)$ can be obtained:

$$\begin{aligned} \tilde{u}_1(k) &= \frac{e^{ik/2}}{\sqrt{2}}(u_1(k) + u_2(k)) = (0\ 0\ 1)^{\mathrm{T}} \\ \tilde{u}_2(k) &= \frac{1}{\sqrt{2}}(u_1(k) - u_2(k)) = (0\ 1\ 0)^{\mathrm{T}} \end{aligned} \tag{1.75}$$

Therefore, when there is a crossing in the occupied bands, a smooth and periodic gauge generally requires the superposition of multiple bands. Note that even though the two bands are only degenerate at one point $k = 0$, for all momentum points the smooth gauge requires a superposition of two bands, including the $\boldsymbol{k}$ points where the bands are not degenerate. For a system with N occupied bands, this amounts to finding a U(N) transformation at each momentum to make the new wave functions $\tilde{u}_n(k) = \sum_{m\in occ} u_m(k)U(k)_{mn}$ smooth and periodic in the BZ, where $U(k)$ is a unitary $N \times N$ matrix. This is the reason why in Eq.(1.45) we require the gauge transform to be U(N) rather than U$(1)^N$.

Due to the superposition of bands, the new wave functions $\tilde{u}_n(k)$ are no longer eigenstates of the original Hamiltonian. Therefore these new bands are also called quasi-bands. Equivalently we can think about the flattened Hamiltonian in which the wave functions are the same as the original Hamiltonian but all the occupied bands have the same energy. In this case the gauge transform is naturally U(N) and the new wave functions $\tilde{u}_n(k)$ are still eigenstates of the flattened Hamiltonian.

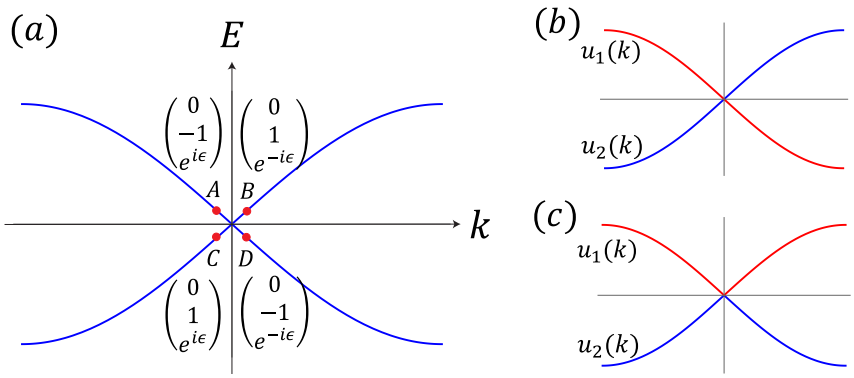

Figure 1.4: Dispersion of the two occupied bands in Eq.(1.74). Four wave functions at two momentum points near $k = 0$ are shown, where ϵ is a small positive number.

CHAPTER II

Diagnosis of Topological Insulators Beyond Symmetry Representations

In the previous chapter, I have introduced the notion of topology in electronic structure, and provided some examples of topological indices. The system's topological properties are encoded in the wave functions. To compute the topological index from wave functions, in many cases a smooth gauge is needed so that the wave functions are smooth with respect to crystal momentum $\boldsymbol{k}$ in the Brillouin zone (BZ), such as the Chern number in Section 1.4.2 and the time-reversal protected FKM Z_2 topological index in Section 1.4.3. However, as mentioned in Section 1.5, it is challenging to obtain a smooth gauge in the Brillouin zone which is a torus, especially in high dimensions and when the number of occupied bands is large. Therefore, the requirement of a smooth gauge in the Brillouin zone is an obstacle to efficient diagnosis of topological phases.

In the presence of symmetries, the process of topological diagnosis can be significantly simplified. The relation between symmetry and topology has been extensively studied in various topological states and has lead to many important results [7, 10, 27, 28, 29, 30, 31, 32, 33, 34, 35, 36, 37, 38, 39, 40, 41, 42, 43, 44]. With sufficient symmetries, whether the system is topological or trivial can be determined by the symmetry representations of the wave functions at high-symmetry momenta

using the framework of topological quantum chemistry or symmetry indicator [7, 10]. With n-fold rotational symmetry the Chern number module n can be determined by rotation eigenvalues [27], and with inversion symmetry the FKM Z_2 topological index can be determined by the parity of wave functions at TRIM [22].

However, not all symmetries are able to provide such simplification. The above symmetry-representation-based diagnosis may not be applicable in systems whose symmetry is too low such that the symmetry representations are the same for both topological and trivial phases. For example, with a twofold rotation symmetry in addition to time-reversal symmetry, the FKM Z_2 index in Section 1.4.3 cannot be simply obtained from rotation eigenvalues. Therefore, in this case whether the additional symmetry can still provide simplification to the diagnosis of topological phases remains an open question.

Our work [45] gives a positive answer to this question by showing that the additional symmetry can still simplify the index even though the symmetry representations are not sufficient to determine the index. In this work, we show that if the system has an additional twofold rotational symmetry or mirror symmetry, the FKM Z_2 index can be simplified so that only one-dimensional lines in the BZ need to be evaluated in the index computation. This method works for both two and three dimensions. This result extends the topological diagnosis methods based on high-symmetry-momenta from 0D points to 1D lines. It is convenient for the computation of the index in practice, because the original definition of the index requires establishing a smooth gauge in at least two dimensions. This simplification is achieved through introducing a gauge-invariant quantity $g(\widetilde{\boldsymbol{k}_a\boldsymbol{k}_b})$ defined on arbitrary curves in the BZ.

2.1 Gauge-invariant line quantity

In this section we introduce the line quantity $g(\widetilde{\boldsymbol{k}_a\boldsymbol{k}_b})$ in our work [45] defined on arbitrary curves in the BZ of a time-reversal symmetric system and discuss some generic properties of it. Consider a gapped system with time-reversal symmetry T and $T^2=-1$. It has N occupied bands and the total number of bands is N_{tot}. Denote $\widetilde{\boldsymbol{k}_a\boldsymbol{k}_b}$ as an arbitrary curve in the BZ with end points at $\boldsymbol{k}_a$ and $\boldsymbol{k}_b$. Some preliminary steps are needed towards our definition of $g(\widetilde{\boldsymbol{k}_a\boldsymbol{k}_b})$ in Eq.(2.9). First, for an arbitrary curve $\widetilde{\boldsymbol{k}_a\boldsymbol{k}_b}$ we can define a Wilson line matrix for the occupied bands:

$$W_{mn}(\widetilde{\boldsymbol{k}_a\boldsymbol{k}_b}) = \langle u_m(\boldsymbol{k}_a)| \prod_{\boldsymbol{k}_i\in\widetilde{\boldsymbol{k}_a\boldsymbol{k}_b}}^{\boldsymbol{k}_a\leftarrow\boldsymbol{k}_b} P_{\boldsymbol{k}_i}|u_n(\boldsymbol{k}_b)\rangle \tag{2.1}$$

$$P_{\boldsymbol{k}} = \sum_{m\in occ} |u_m(\boldsymbol{k})\rangle\langle u_m(\boldsymbol{k})| \tag{2.2}$$

Here $P_{\boldsymbol{k}}$ is a projection operator to the occupied bands at $\boldsymbol{k}$. $|u_n(\boldsymbol{k})\rangle$ is the eigenstate of Hamiltonian $H(\boldsymbol{k})$, which is a N_{tot}-component column vector with its jth component denoted as $u_n(\boldsymbol{k})_j$. The product in the definition of W is the path-ordered along the curve $\widetilde{\boldsymbol{k}_a\boldsymbol{k}_b}$. Under a gauge transformation $|u_m(\boldsymbol{k})\rangle \to \sum_{n\in occ}|u_n(\boldsymbol{k})\rangle U_{nm}(\boldsymbol{k})$, W transforms as

$$W(\widetilde{\boldsymbol{k}_a\boldsymbol{k}_b}) \to U^\dagger(\boldsymbol{k}_a)W(\widetilde{\boldsymbol{k}_a\boldsymbol{k}_b})U(\boldsymbol{k}_b) \tag{2.3}$$

$$\det[W(\widetilde{\boldsymbol{k}_a\boldsymbol{k}_b})] \to \det[W(\widetilde{\boldsymbol{k}_a\boldsymbol{k}_b})]\det[U(\boldsymbol{k}_b)]\det[U(\boldsymbol{k}_a)]^* \tag{2.4}$$

When $\boldsymbol{k}_a$ and $\boldsymbol{k}_b$ are the same point, i.e., the curve $\widetilde{\boldsymbol{k}_a\boldsymbol{k}_b}$ is closed, W is the Wilson loop [2, 46] and $\det[W]$ is a gauge-invariant quantity, but for a generic curve it is not. To construct a gauge-invariant quantity, we need another factor to cancel out the factor $\det[U(\boldsymbol{k}_b)]\det[U(\boldsymbol{k}_a)]^*$ in Eq.(2.4). This is achieved by the anti-symmetric matrix $M(\boldsymbol{k})$:

$$M(\boldsymbol{k}) = \langle u_m(\boldsymbol{k})|T|u_n(\boldsymbol{k})\rangle \tag{2.5}$$

When $\boldsymbol{k}$ is one of the TRIM so that $\boldsymbol{k} = -\boldsymbol{k} + \boldsymbol{G}$, $M(\boldsymbol{k})$ is the same as the sewing matrix defined in Eq.(1.66). The anti-symmetric property of $M(\boldsymbol{k})$ for a generic $\boldsymbol{k}$ can be seen by:

$$\begin{aligned} M(\boldsymbol{k})_{mn} &= \langle u_m(\boldsymbol{k})|T|u_n(\boldsymbol{k})\rangle \\ &= \langle T^2 u_n(\boldsymbol{k})|T|u_m(\boldsymbol{k})\rangle \\ &= -\langle u_n(\boldsymbol{k})|T|u_m(\boldsymbol{k})\rangle \\ &= -M(\boldsymbol{k})_{nm} \end{aligned} \tag{2.6}$$

Therefore we can define the Pfaffian for the anti-symmetric matrix $M(\boldsymbol{k})$ for any $\boldsymbol{k}$ in the BZ. Under the gauge transformation, using $\mathrm{Pf}[BAB^{\mathrm{T}}] = \mathrm{Pf}[A]\det[B]$ and the fact that T is an antiunitary operator, the M matrix and its Pfaffian transform as:

$$M(\boldsymbol{k}) \rightarrow U^{\dagger}(\boldsymbol{k})M(\boldsymbol{k})U^{*}(\boldsymbol{k}) \tag{2.7}$$

$$\mathrm{Pf}[M(\boldsymbol{k})] \rightarrow \mathrm{Pf}[M(\boldsymbol{k})]\det[U(\boldsymbol{k})]^{*} \tag{2.8}$$

Therefore, we can define the gauge-invariant line quantity $g(\widetilde{\boldsymbol{k}_a\boldsymbol{k}_b})$ by:

$$g(\widetilde{\boldsymbol{k}_a\boldsymbol{k}_b}) = \frac{\mathrm{Pf}[M(\boldsymbol{k}_b)]}{\mathrm{Pf}[M(\boldsymbol{k}_a)]}\det[W(\widetilde{\boldsymbol{k}_a\boldsymbol{k}_b})] \tag{2.9}$$

This quantity is gauge-invariant because the factors induced by gauge transform in the Pfaffian and determinant cancel each other:

$$g(\widetilde{\boldsymbol{k}_a\boldsymbol{k}_b}) \rightarrow \frac{\mathrm{Pf}[M(\boldsymbol{k}_b)]\det[U(\boldsymbol{k}_b)]^{*}}{\mathrm{Pf}[M(\boldsymbol{k}_a)]\det[U(\boldsymbol{k}_a)]^{*}}\det[W(\widetilde{\boldsymbol{k}_a\boldsymbol{k}_b})]\det[U(\boldsymbol{k}_b)]\det[U(\boldsymbol{k}_a)]^{*} = g(\widetilde{\boldsymbol{k}_a\boldsymbol{k}_b}) \tag{2.10}$$

This property of gauge invariance is important, because it means $g(\widetilde{\boldsymbol{k}_a\boldsymbol{k}_b})$ is smooth in any gauge as long as the Hamiltonian itself is smooth. In the special case when $\widetilde{\boldsymbol{k}_a\boldsymbol{k}_b}$ is the straight line connecting different TRIM, for example when $\boldsymbol{k}_a = \Gamma = (0,0,0)$ and

$\boldsymbol{k}_b = X = (\pi, 0, 0)$, $g(\widetilde{\boldsymbol{k}_a\boldsymbol{k}_b})$ is related to the partial polarization ν_{1D} [17, 39, 40, 42, 43]:

$$\begin{aligned} \nu_{1D} &= \frac{1}{\pi}\left[\int_{\Gamma}^{X} dk\, \mathrm{Tr}\, \mathcal{A}(k) + i \log \frac{\mathrm{Pf}[\omega(X)]}{\mathrm{Pf}[\omega(\Gamma)]}\right] \mod 2 \\ &= \frac{1}{\pi} i \log[g(\overline{\Gamma X})] \mod 2, \end{aligned} \tag{2.11}$$

For a generic curve $\widetilde{\boldsymbol{k}_a\boldsymbol{k}_b}$ in the BZ, $g(\widetilde{\boldsymbol{k}_a\boldsymbol{k}_b})$ has a physical meaning that it measures the change in phase between the Pfaffian at $\boldsymbol{k}_a$ and $\boldsymbol{k}_b$. To illustrate this point, we define the parallel transport gauge [47] at path $\widetilde{\boldsymbol{k}_a\boldsymbol{k}_b}$ so that for each $\boldsymbol{k} \in \widetilde{\boldsymbol{k}_a\boldsymbol{k}_b}$,

$$|u_m(\boldsymbol{k})\rangle = \prod_{\boldsymbol{k}_i \in \widetilde{\boldsymbol{k}\boldsymbol{k}_a}}^{\boldsymbol{k}\leftarrow\boldsymbol{k}_a} P_{\boldsymbol{k}_i} |u_m(\boldsymbol{k}_a)\rangle \tag{2.12}$$

Here the product is path-ordered from $\boldsymbol{k}_a$ to $\boldsymbol{k}$ along $\widetilde{\boldsymbol{k}_a\boldsymbol{k}_b}$. In the limit where the points $\{\boldsymbol{k}_i\}$ are infinitely dense along $\widetilde{\boldsymbol{k}\boldsymbol{k}_a}$, the $|u_m(\boldsymbol{k})\rangle$ obtained in this way is a normalized vector in the occupied space. In the practical computation, a discrete mesh of momentum points $\{\boldsymbol{k}_i\}$ is used and we need to normalize Eq.(2.12) for each $\boldsymbol{k}$. With this gauge choice along the path, the determinant part in $g(\widetilde{\boldsymbol{k}_a\boldsymbol{k}_b})$ becomes unity, leading to

$$g(\widetilde{\boldsymbol{k}_a\boldsymbol{k}_b}) = \frac{\mathrm{Pf}[M(\boldsymbol{k}_b)]}{\mathrm{Pf}[M(\boldsymbol{k}_a)]} \tag{2.13}$$

Hence $g(\widetilde{\boldsymbol{k}_a\boldsymbol{k}_b})$ represents the ratio between the Pfaffian $\mathrm{Pf}[M]$ at $\boldsymbol{k}_b$ and $\boldsymbol{k}_a$ in the parallel transport gauge. This interpretation is useful, because the topological index is related to the winding of the phase of Pfaffian. For example, in a 2D system whose BZ is shown in Fig.(2.1), the FKM Z_2 index in Eq.(1.70) can be written in an equivalent way [16, 17]:

$$\nu_{2D} = \frac{1}{2\pi i} \oint_{\partial\tau} d\boldsymbol{k} \cdot \nabla \log \mathrm{Pf}[M(\boldsymbol{k})] \tag{2.14}$$

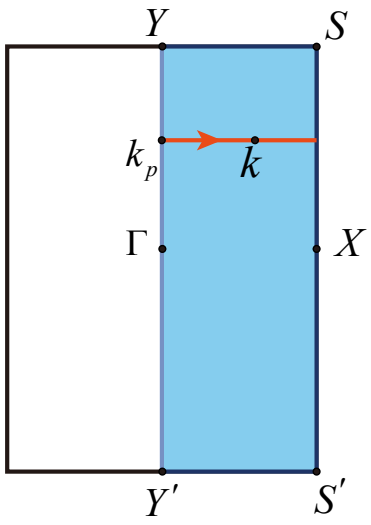

Figure 2.1: The Brillouin zone for 2D insulator with time reversal symmetry. τ is represented by the shaded area enclosed by $SYY'S'$.

Here τ is the area enclosed by $SYY'S'$ and $\partial\tau$ is its boundary. Similar to Eq.(1.70), this formula also requires a smooth and periodic gauge such that $M(\boldsymbol{k})$ is smooth in the BZ. Eq.(2.14) shows that this index is related to the change of the phase of $\mathrm{Pf}[M(\boldsymbol{k})]$ along the boundary $\partial\tau$. However, the Pfaffian itself is gauge-dependent as in Eq.(2.8), making it challenging to track its phase. The quantity $g(\widetilde{\boldsymbol{k}_a\boldsymbol{k}_b})$ is naturally gauge-invariant, therefore with the interpretation in Eq.(2.13) it provides a convenient way to bypass the gauge issue and track the phase of Pfaffian.

Now we will show that ν_{2D} can be rewritten in terms of the gauge-invariant quantity g. From now on it is sufficient to restrict the path $\widetilde{\boldsymbol{k}_a\boldsymbol{k}_b}$ to be the straight line $\overline{\boldsymbol{k}_a\boldsymbol{k}_b}$ connecting $\boldsymbol{k}_a$ and $\boldsymbol{k}_b$ and define:

$$\begin{aligned} g(\boldsymbol{k}_a,\boldsymbol{k}_b) &= g(\overline{\boldsymbol{k}_a\boldsymbol{k}_b}) \\ &= \frac{\mathrm{Pf}[M(\boldsymbol{k}_b)]}{\mathrm{Pf}[M(\boldsymbol{k}_a)]}\det\left[\langle u_m(\boldsymbol{k}_a)|\prod_{\boldsymbol{k}_i\in\overline{\boldsymbol{k}_a\boldsymbol{k}_b}}^{\boldsymbol{k}_a\leftarrow\boldsymbol{k}_b} P_{\boldsymbol{k}_i}|u_n(\boldsymbol{k}_b)\rangle\right] \end{aligned} \tag{2.15}$$

We construct a parallel transport gauge on τ as follows [47]. First, we find a smooth

and periodic gauge along straight line $\overline{YY'}$. To achieve this, first we select an arbitrary gauge at Y', then for each $\boldsymbol{k} \in YY'$, we define the gauge for wave functions at $\boldsymbol{k}$ using Eq.(2.12) with $\boldsymbol{k}_a = Y'$ and $\boldsymbol{k}_b = Y$. This establishes a smooth parallel transport gauge along the path YY', but it does not satisfy the periodic boundary condition, i.e., the wave functions at Y and Y' are different. To recover the periodicity, we can make a unitary transform at each $\boldsymbol{k}$ to a new set of wave functions $|\tilde{u}_m(\boldsymbol{k})\rangle$:

$$
\begin{aligned}
|\tilde{u}_m(\boldsymbol{k})\rangle &= \sum_{n\in occ} |u_n(\boldsymbol{k})\rangle D(\boldsymbol{k})_{nm} \\
D(\boldsymbol{k}) &= D_0^{\frac{|\boldsymbol{k}-Y'|}{|Y-Y'|}} \\
(D_0)_{nm} &= \langle u_n(Y)|u_m(Y')\rangle, \quad m,n \in occ
\end{aligned}
\tag{2.16}
$$

The matrices D and D_0 are unitary by definition. Then the new wave functions $|\tilde{u}_m(\boldsymbol{k})\rangle$ are smooth and periodic along path YY', which we will refer to as $|u_m(\boldsymbol{k})\rangle$ from now on. Next we proceed to construct a smooth and periodic gauge in τ. For each $\boldsymbol{k} \in \tau$, denote its projection to $\overline{YY'}$ as $\boldsymbol{k}_p$ such that $\overline{\boldsymbol{k}_p\boldsymbol{k}}$ is parallel to $\overline{YS}$, as shown in Fig.(2.1). The parallel transport gauge is defined by setting the wave function at $\boldsymbol{k}$ to be:

$$
|u_m(\boldsymbol{k})\rangle = \prod_{\boldsymbol{k}_i \in \overline{\boldsymbol{k}_p\boldsymbol{k}}}^{\boldsymbol{k}\leftarrow\boldsymbol{k}_p} P_{\boldsymbol{k}_i} |u_m(\boldsymbol{k}_p)\rangle \tag{2.17}
$$

The gauge constructed in this way is smooth on τ and satisfies the periodic boundary condition between $\overline{YS}$ and $\overline{Y'S'}$, because the wave function at $\overline{YS}$ and $\overline{Y'S'}$ are parallel transported from the same set of wave functions at Y and Y'. For each $\boldsymbol{k}_p \in \overline{YY'}$, we have $\boldsymbol{k}_p + \pi\hat{x} \in \overline{SS'}$ and Eq.(2.13) implies

$$
g(\boldsymbol{k}_p, \boldsymbol{k}_p + \pi\hat{x}) = \frac{\mathrm{Pf}[M(\boldsymbol{k}_p + \pi\hat{x})]}{\mathrm{Pf}[M(\boldsymbol{k}_p)]} \tag{2.18}
$$

This relation provides a way to reformulate the Z_2 index ν_{2D} in terms of g. Define

$\overline{g}(\boldsymbol{k}) = g(\boldsymbol{k}, \boldsymbol{k} + \pi\hat{x})$, then Eq.(2.14) becomes

$$\begin{aligned}
\nu_{2D} &= \frac{1}{2\pi i}\left(\int_{S'}^{S} - \int_{Y'}^{Y}\right) d\boldsymbol{k} \cdot \nabla \log \mathrm{Pf}[M(\boldsymbol{k})] \\
&= \frac{1}{2\pi i}\int_{Y'}^{Y} d\boldsymbol{k} \cdot \nabla \log \frac{\mathrm{Pf}[M(\boldsymbol{k} + \pi\hat{x})]}{\mathrm{Pf}[M(\boldsymbol{k})]} \\
&= \frac{1}{2\pi i}\int_{Y'}^{Y} d\boldsymbol{k} \cdot \nabla \log \overline{g}(\boldsymbol{k}) \qquad (2.19)
\end{aligned}$$

Here the final integral is along a time-reversal invariant path that connects Y, Γ and Y'. Eq.(2.19) shows that ν_{2D} can be expressed in terms of the line quantity g. Although Eq.(2.19) is derived in the specific parallel transport gauge, the gauge-invariance of g implies that this formula is valid in any gauge. This means that the above construction of the smooth parallel transport gauge is only a conceptual step which is never needed in a real calculation. Importantly, the evaluation of g itself does not require a smooth gauge to begin with. In practice, to evaluate ν_{2D} from Eq.(2.19), all we need is to make a discrete mesh of $\boldsymbol{k}$ points in τ with randomly selected phase for each wave function, and by definition in Eq.(2.15) the function $\overline{g}(\boldsymbol{k}) = g(\boldsymbol{k}, \boldsymbol{k} + \pi\hat{x})$ will be smooth in $\boldsymbol{k}$, which can lead to a well-defined result in Eq.(2.19). Up to now Eq.(2.19) requires only time-reversal symmetry, which is the least requirement in symmetry to protect the FKM Z_2 topological index.

2.2 Topological insulators with order-two crystalline symmetries in addition to time-reversal symmetry

We will show that if a 2D or 3D time-reversal invariant topological insulators (TIs) have an additional order-two crystalline symmetry, for example two-fold rotation C_2 or mirror σ, the line quantity g defined above in Eq.(2.9) or Eq.(2.15) can simplify

the FKM Z_2 index ν to involve only one-dimensional lines of the BZ. Note that the eigenvalues of the spacial symmetry C_2 or σ at high symmetry momenta are not sufficient to determine the Z_2 index, because for a spin one-half system C_2 or σ has eigenvalues $\pm i$ and the two bands in each Kramers pair have opposite eigenvalues of C_2 or σ. Therefore, at any C_2 invariant momentum there are always a half of valence bands with C_2 or mirror eigenvalue $+i$ and the other half with eigenvalue $-i$ no matter ν is trivial or not. Hence spacial symmetry eigenvalues themselves are insufficient to determine the topological index.

2.2.1 Systems with additional two-fold rotational symmetry

When the system has additional spacial symmetries, the line quantity $g(\boldsymbol{k}_a, \boldsymbol{k}_b)$ has a useful property as follows. Suppose the system has a symmetry C such that a point $\boldsymbol{k}$ in the BZ is transformed to $C\boldsymbol{k}$, and C can be the combination of time-reversal and spacial symmetries. If C commutes with time-reversal T and the matrix representing C is independent of $\boldsymbol{k}$, then depending on whether C is unitary or anti-unitary, $g(\boldsymbol{k}_a, \boldsymbol{k}_b)$ in Eq.(2.15) satisfies:

$$\begin{aligned} g(C\boldsymbol{k}_a, C\boldsymbol{k}_b) &= g(\boldsymbol{k}_a, \boldsymbol{k}_b), \text{ if C is unitary} \\ g(C\boldsymbol{k}_a, C\boldsymbol{k}_b) &= g(\boldsymbol{k}_a, \boldsymbol{k}_b)^*, \text{ if C is anti-unitary} \end{aligned} \tag{2.20}$$

This property comes from the transformation properties of the Pfaffian and the Wilson line operator. We give a detailed proof of this property in Appendix A.1. This property is important in evaluating $g(\boldsymbol{k}_a, \boldsymbol{k}_b)$ at symmetry-related lines in the BZ. Now we consider systems with a two-fold rotational symmetry C_2 in additional to time-reversal T. The combined operator C_2T is also a symmetry of the system which acts on the momentum space like a mirror, therefore there are C_2T invariant planes in the BZ. Suppose there are two such planes that include all eight time-reversal invariant

momenta (TRIM) as in Fig.(2.2)(a), where the C_2 axis is along z direction and C_2T invariant planes are colored in yellow. If $\boldsymbol{k}_a, \boldsymbol{k}_b$ are taken inside one of the C_2T invariant planes, then Eq.(2.20) shows $g(\boldsymbol{k}_a, \boldsymbol{k}_b) = g(C_2T\boldsymbol{k}_a, C_2T\boldsymbol{k}_b)^* = g(\boldsymbol{k}_a, \boldsymbol{k}_b)^*$ so that $g(\boldsymbol{k}_a, \boldsymbol{k}_b)$ is real because C_2T is anti-unitary. If $\boldsymbol{k}_a, \boldsymbol{k}_b$ are taken to be TRIM, then $g(\boldsymbol{k}_a, \boldsymbol{k}_b)$ should have magnitude of 1 because the M matrices in Eq.(2.15) are unitary at TRIM. These two conditions quantize $g(K_1, K_2)$ to ± 1, where K_1, K_2 are TRIM in the same C_2T invariant plane. Furthermore, as in Eq.(2.11), $g(K_1, K_2)$ is related to the partial polarization ν_{1D}:

$$\begin{aligned} \nu_{1D}(K_1, K_2) &= \frac{1}{\pi}\left[\int_{K_1}^{K_2} d\boldsymbol{k} \cdot \mathrm{Tr}\, \mathcal{A}(\boldsymbol{k}) + i \log \frac{\mathrm{Pf}[\omega(K_2)]}{\mathrm{Pf}[\omega(K_1)]}\right] \mod 2 \\ g(K_1, K_2) &= e^{i\pi\nu_{1D}(K_1,K_2)} = \pm 1 \end{aligned} \tag{2.21}$$

It has been shown in Ref.[43] that the FKM Z_2 index for a 2D system is equivalent to the difference between the $1D$ partial polarization ν_{1D} at two pairs of TRIM:

$$\begin{aligned} \nu_{2D}(k_z = 0) &= \nu_{1D}(\Gamma, X) - \nu_{1D}(Y, S) \mod 2 \\ \nu_{2D}(k_z = \pi) &= \nu_{1D}(Z, U) - \nu_{1D}(T, R) \mod 2 \end{aligned} \tag{2.22}$$

The FKM strong Z_2 index in 3D is given by $\nu_{3D} = \nu_{2D}(k_z = 0) - \nu_{2D}(k_z = \pi) \mod 2$. Combining with Eq.(2.21) we have

$$(-1)^{\nu_{3D}} = g(\Gamma, X) g(Y, S) g(Z, U) g(T, R) \tag{2.23}$$

Therefore the 3D strong Z_2 index is simplified by the line quantity $g(\boldsymbol{k}_a, \boldsymbol{k}_b)$ so that it involves only 1D subspace of the BZ.

Eq.(2.23) assumes that all the eight TRIM are included in some C_2T invariant planes, which is not always true for a general C_2 rotation. For example, if the C_2 axis

is along direction $\hat{x}+\hat{y}$ rather than $\hat{z}$ for the same Brillouin zone as in Fig.(2.2)(b), there is only one C_2T invariant plane S_1 passing through Γ, S', R', Z. Denote the other time-reversal invariant plane passing through X, Y, T, U as S_2, Then $\nu_{3D} = \nu_{2D}(S_1) - \nu_{2D}(S_2) \mod 2$. We show that $\nu_{2D}(S_2)$ must vanish due to the C_2 symmetry. Denote the midpoint of $\overline{XY}$ as M. Since C_2 is unitary, from Eq.(2.20) we have $g(X,M) = g(C_2X, C_2M) = g(Y,M) = g(M,Y)^{-1}$. Therefore $g(X,Y) = g(X,M)g(M,Y) = 1$, which means the partial polarization $\nu_{1D}(X,Y)$ is quantized to 0. The same argument can be applied to $\overline{TU}$. Hence $\nu_{1D}(X,Y) = \nu_{1D}(T,U) = 0$ due to the C_2 symmetry, therefore $\nu_{2D}(S_2)$ vanishes. We present a more detailed proof of the triviality of $\nu_{2D}(S_2)$ in Appendix A.2 using the interpretation of $g(\boldsymbol{k}_a, \boldsymbol{k}_b)$ as a measure of Pfaffian in the parallel transport gauge. With this result, the strong Z_2 index ν_{3D} is determined only by lines in C_2T invariant plane S_1:

$$(-1)^{\nu_{3D}} = (-1)^{\nu_{2D}(S_1)} = g(\Gamma, S')g(Z, R') \tag{2.24}$$

The above proof for Eq.(2.23) and (2.24) for different types of C_2 axis can be unified in a general framework, which is also applicable to Brillouin zones that are not cube-shaped. There are eight TRIM $K_i, i = 1...8$ in a 3D BZ. Since time-reversal operator commutes with C_2, C_2 must bring one TRIM to itself or to another TRIM. For those TRIM non-invariant under C_2, let $C_2K_i = K_j$ and $C_2K_j = K_i$, then the midpoint $M = (K_i + K_j)/2$ must be invariant under C_2, and $g(K_i, M) = g(C_2K_i, C_2M) = g(K_j, M) = g(M, K_j)^{-1}$. Therefore $g(K_i, K_j) = g(K_i, M)g(M, K_j) = 1$. This fixes the partial polarization $\nu_{1D}(K_i, K_j) = 0$, which does not contribute to the strong index ν_{3D}. Therefore we only need to consider those TRIM that are also invariant under C_2. Define the C_2T invariant subspace in the BZ by $S_{C_2T} = \{\boldsymbol{k} \in BZ | C_2T\boldsymbol{k} = \boldsymbol{k} + \boldsymbol{G}\}$ where $\boldsymbol{G}$ is any reciprocal lattice vector, and define a set L_{C_2T} to be the set of straight paths inside S_{C_2T} such that each path $\gamma \in L_{C_2T}$ connects two C_2-invariant TRIM,

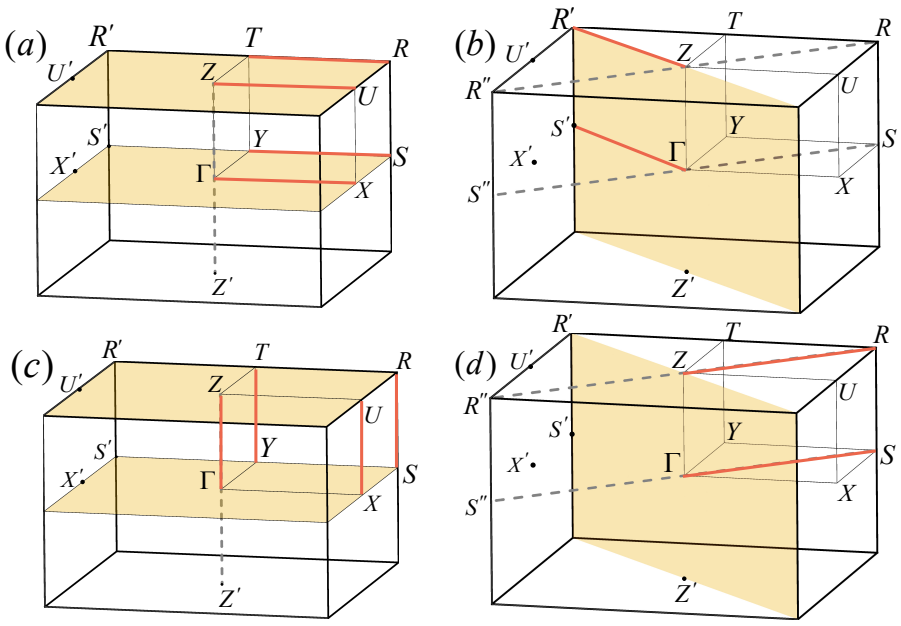

Figure 2.2: The plot of a 3D Brillouin zone. The red lines denote the one-dimensional subspace that is needed to evaluate the FKM strong Z_2 index in Eq.(2.25) and (2.28). (a) System with a C_2 symmetry along $\hat{z}$ direction. The colored planes are the C_2T invariant planes. (b) System with a C_2 symmetry along $\hat{x}+\hat{y}$ direction. There is only one C_2T invariant plane. (c) System with a mirror plane perpendicular to $\hat{z}$. (d) System with a mirror plane perpendicular to $\hat{x}+\hat{y}$.

different paths in L_{C_2T} do not cross with each other, and each C_2-invariant TRIM is connected by one path in L_{C_2T}. With this definition, in Fig.(2.2) (a) and (b) L_{C_2T} reduces to the red lines $\{\overline{\Gamma X}, \overline{YS}, \overline{ZU}, \overline{TR}\}$ and $\{\overline{\Gamma S'}, \overline{ZR'}\}$ respectively (or equivalently $\{\overline{\Gamma Y}, \overline{XS}, \overline{ZT}, \overline{UR}\}$ and $\{\overline{\Gamma Z}, \overline{S'R'}\}$, which does not change the final result). Therefore Eq.(2.23) and (2.24) can be unified as

$$(-1)^{\nu_{3D}} = \prod_{\gamma \in L_{C_2T}} \mathrm{Sign}[g(\gamma)] \tag{2.25}$$

Here the sign function Sign is added to take account of the fact that the absolute value of $g(\gamma)$ can be smaller than 1 in a practical numerical calculation in which the projection in Eq.(2.15) is taken at discrete points. In this case $g(\gamma)$ is still real, and the sign of it determines the index ν_{3D}. Eq.(2.25) shows that for any topological insulator with an additional two-fold rotational symmetry, the FKM strong Z_2 index can be computed through a well-defined one-dimensional subspace of the Brillouin zone. If there are multiple C_2 axes in the system, this simplification can be applied to any one of the C_2, independent of the presence of the other symmetries. This calculation is applicable to 2D insulators as well, which can be achieved by restricting L_{C_2T} to the 2D Brillouin zone. This method is convenient to implement in the sense that it does not require a smooth gauge, because the definition of $g(\gamma)$ in Eq.(2.15) is gauge-independent.

2.2.2 Systems with additional mirror symmetry

For systems with a mirror symmetry σ in additional to T, similar analysis can be applied by evaluating $g(\boldsymbol{k}_a, \boldsymbol{k}_b)$ in the σT invariant subspace defined by $S_{\sigma T} = \{\boldsymbol{k} \in BZ | \sigma T \boldsymbol{k} = \boldsymbol{k} + \boldsymbol{G}\}$. If the mirror is perpendicular to $\hat{z}$ as in Fig.(2.2)(c), then $S_{\sigma T}$ consists of four straight paths along $\hat{z}$ direction that pass through TRIM. Since σT is anti-unitary, Eq.(2.20) implies $g(\Gamma, Z) = g(\sigma T \Gamma, \sigma T Z)^* = g(\Gamma, Z)^*$, therefore

$g(\Gamma, Z)$ is real and quantizes to ± 1, so as $g(X, U), g(Y, T), g(S, R)$. Following the same argument as the C_2 case, we have

$$\nu_{3D} = g(\Gamma, Z)g(X, U)g(Y, T)g(S, R) \tag{2.26}$$

If the mirror plane is perpendicular to $\hat{x}+\hat{y}$ as in Fig.(2.2)(d), $S_{\sigma T}$ consists of two lines $\{\overline{SS''}, \overline{RR''}\}$. The TRIM Γ, S, Z, R are invariant under the mirror symmetry σ but X', Y, U', T are not. Following the same argument, $g(X', Y)$ and $g(U', T)$ are fixed to 1 because these two points interchange under σ, therefore they do not contribute to ν_{3D}. In this case we have

$$\nu_{3D} = g(\Gamma, S)g(Z, R) \tag{2.27}$$

In general, similar to the C_2 case above, we can define $L_{\sigma T}$ to be the set of straight paths inside $S_{\sigma T}$ such that each path $\gamma \in L_{\sigma T}$ connects two mirror-invariant TRIM, different paths in $L_{\sigma T}$ do not cross with each other, and each mirror-invariant TRIM is connected by one path in $L_{\sigma T}$. In Fig.(2.2) (c) and (d) $L_{\sigma T}$ reduces to $\{\overline{\Gamma Z}, \overline{XU}, \overline{YT}, \overline{SR}\}$ and $\{\overline{\Gamma S}, \overline{ZR}\}$ respectively. Note that in Fig.(2.2)(d) we cannot take $\{\overline{\Gamma Z}, \overline{SR}\}$ because these lines are not inside σT invariant subspace. With this definition, the index is written as

$$\nu_{3D} = \prod_{\gamma \in L_{\sigma T}} \text{Sign}[g(\gamma)] \tag{2.28}$$

Here the sign function takes account of the fact that $|g(\gamma)|$ can be smaller than 1 in a real calculation on discrete momentum points. With Eq.(2.25) and (2.28), we have developed a unified method to calculate FKM strong Z_2 topological index that requires examining only a 1D subspace of the BZ, for systems with two-fold rotation or mirror symmetry. If the system has multiple mirrors or C_2 axes, this method will work if we focus on any one of them.

It is also worthwhile to explore the situation when the system has space-inversion

symmetry I in addition to T. It turns out that our method is still applicable, although the Z_2 index can be determined directly by inversion eigenvalues. In this case Eq.(2.20) when applied to symmetry operator IT shows that that $g(\boldsymbol{k}_a, \boldsymbol{k}_b)$ is real everywhere, since every momentum point is invariant under IT. This implies $g(K_i, K_j)$ will be quantized to ± 1 for any pair of TRIM K_i and K_j. Therefore our method is applicable again and we have $(-1)^{\nu_{3D}} = \prod_\gamma g(\gamma)$, where the product ranges over the four lines that connect the eight TRIM.

We have shown that in systems where topological indices cannot be reduced to high-symmetry-point symmetry eigenvalues, certain symmetries can still help simplify the calculation of the index. With the definition of the gauge-invariant line quantity $g(\boldsymbol{k}_a, \boldsymbol{k}_b)$, we present a unified way to calculate topological index by examining only 1D subspace of the Brillouin zone for systems with either C_2 or mirror symmetry in addition to time-reversal symmetry. Our method is applicable to a wide range of systems because among all the 32 point groups, 30 of them contain such a symmetry, except for C_3 the the trivial group C_1. This approach also finds its application in higher-order topological insulators described in the next chapter.

CHAPTER III

Pfaffian Formalism for Higher-order Topological Insulators

The topological insulators (TIs) described in the previous chapters have gapped d-dimensional bulk states and gapless $(d-1)$-dimensional topologically protected boundary modes, such as the Chern insulator and the Z_2 topological insulators. The existence of boundary modes with codimension 1 is a manifestation of the bulk-boundary correspondence, and these insulators are also called first-order topological insulators. Similarly, there exists higher-order topological insulators (HOTIs) whose gapless boundary modes appear at lower dimensional boundaries [48, 49, 50, 51, 52, 53, 54, 55, 56, 57, 58, 59, 60, 61, 62, 63, 64, 65, 66, 67, 68, 69, 70, 71], i.e., the n-th order HOTI has gapless modes at $(d-n)$-dimensional boundaries. For example, the 3D second-order TIs have gapless modes localized at one-dimensional hinges, and the 2D second-order TIs have in-gap modes localized at corners which can lead to fractional corner charges.

The robustness of these boundary modes require symmetry protection, and there are various symmetries that can protect the higher-order topological phase, such as space-inversion, mirror reflection, rotoinversion, the product of rotation and time-reversal C_nT [48, 49, 50, 51, 52, 53, 54, 55, 56], etc. The existence of the higher-order topological boundary modes requires both the bulk and the set of its boundaries to

preserve the protecting symmetry.

There are many different mechanisms that can lead to higher-order topology, such as the Wannier-sector polarization from nested Wilson loops [58, 59], filling anomaly [8], the sign change of mass terms [57], etc. Here I illustrate the formation of higher-order topological features using an example of 3D chiral second-order topological insulators protected by C_4T symmetry [48], where C_4 is the fourfold rotation along z direction and T is the spin one-half time-reversal operator satisfying $T^2 = -1$. This system has the product C_4T as its symmetry, but C_4 and T are broken separately. The topological index is the magnetoelectric polarization P_3 [23, 27, 48, 72, 73, 74, 75, 76] defined as:

$$P_3 = \frac{1}{16\pi^2} \int d^3k \epsilon_{abc} \,\mathrm{Tr}\left[\mathcal{F}_{ab}(\boldsymbol{k})\mathcal{A}_c(\boldsymbol{k}) - \frac{i}{3}\left[\mathcal{A}_a(\boldsymbol{k}), \mathcal{A}_b(\boldsymbol{k})\right]\mathcal{A}_c(\boldsymbol{k})\right]. \tag{3.1}$$

Here a, b, c can be x, y, z, $\mathcal{A}$ and $\mathcal{F}$ are nonabelian Berry connection and Berry curvature matrices for the occupied bands:

$$\begin{aligned} \mathcal{A}_a(\boldsymbol{k})_{mn} &= -i\langle u_m(\boldsymbol{k})|\partial_a|u_n(\boldsymbol{k})\rangle,\ \partial_a \equiv \partial_{k_a},\ m, n \in occ \\ \mathcal{F}_{ab}(\boldsymbol{k}) &= \partial_a\mathcal{A}_b(\boldsymbol{k}) - \partial_b\mathcal{A}_a(\boldsymbol{k}) + \mathrm{i}\left[\mathcal{A}_a(\boldsymbol{k}), \mathcal{A}_b(\boldsymbol{k})\right] \end{aligned} \tag{3.2}$$

P_3 is quantized to 0 or $\frac{1}{2}$ when the system has an axion-odd symmetry, which includes time-reversal and C_4T. If the system has spinful time-reversal symmetry with $T^2 = -1$, then $2P_3$ is identical to the FKM Z_2 index in Eq.(1.70) [72], and when $P_3 = \frac{1}{2}$ the system is the first-order Z_2 topological insulator described in Section 1.4.3 with gapless Dirac cones in the surface Brillouin zone. If time-reversal symmetry is broken but the system preserves spinful C_4T symmetry, the phase with $P_3 = \frac{1}{2}$ is the nontrivial chiral second-order topological insulator with chiral modes localized at the hinges parallel to the C_4 axis, as shown in Fig.(3.1). The direction of these chiral hinge modes preserve C_4T symmetry and the side surfaces are gapped. These hinge modes are stable as

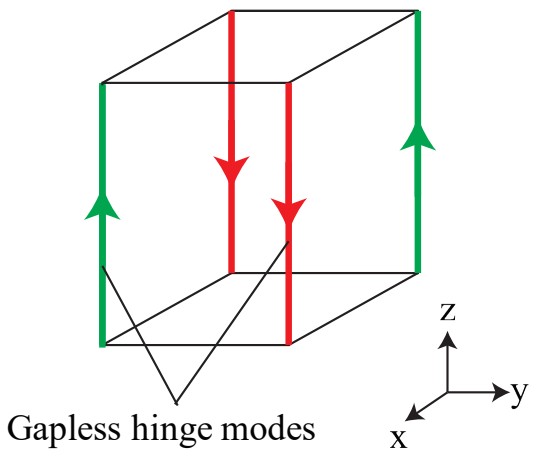

Figure 3.1: Illustration of a second-order topological insulator protected by C_4T. There are chiral hinge modes localized at the hinges of the real space boundary. The propagating directions of these hinge modes obey C_4T symmetry.

long as the bulk and the boundaries together preserve the C_4T symmetry.

The existence of these hinge modes can be understood from the sign change of mass term at neighbouring surfaces. The C_4T-symmetric second-order TI can be obtained from a first-order TI which preserves both C_4 and T by adding a perturbation ΔV in the bulk that breaks time-reversal but preserves the product C_4T. Without ΔV, there are gapless Dirac cones protected by time-reversal in the surface Hamiltonian $H_{surface} \sim k_1\sigma_1 + k_2\sigma_2$. The perturbation ΔV breaks time-reversal and induces a mass term $m\sigma_3$ in the surface Hamiltonian so that the Dirac cone is gapped out. Because ΔV also breaks C_4, the mass term induced by it will change sign at different surfaces that are related by C_4. Therefore, the mass term has to vanish at the hinge where the surfaces with different sign of mass term meet. This implies the hinge will remain gapless, leading to to the features of higher-order topological phases.

Although these higher-order TIs are characterized by the same index P_3 as the first-order TIs, which suggests a strong and deep connection between the two, one important link between these TIs and higher order TIs is still missing, i.e., the FKM

Pfaffian formula [16, 17] described previously in Eq.(1.70). This Pfaffian formula laid the foundation for many important conclusions about TIs. First, the Pfaffian formula enables the development of a gauge-independent method to compute the index. For example, in principle, to compute the Z_2 index for a TI, it requires a global gauge in the entire 3D Brillouin zone (BZ), which means the wave functions are globally smooth and periodic in the entire Brillouin zone. Although the existence of such a gauge is guaranteed, finding it is not always straightforward, as mentioned in Section 1.5. Based on the Pfaffian formula, numerical techniques [77, 78] can be developed so that the construction of a global gauge is no longer needed. Another important aspect of the Pfaffian formula is that the Fu-Kane parity criterion [17] can be derived from it, which allows us to determine the topological index directly from the parity of wave functions in the presence of additional space inversion symmetry. This opens the door to the diagnosis of topological phases via symmetry representations of the wave functions. For second-order TIs, however, due to the broken time-reversal symmetry, a Pfaffian formalism is still absent, and thus many knowledge that we accumulated from studying TIs cannot be directly generalized.

In our work [79], we develop a Pfaffian formalism for higher-order topological insulators protected by C_4T symmetry, utilizing a composite operator obtained from C_4T sewing matrix. We found that in strong analogy to TIs, the topological index of these higher-order TIs can also be determined via a Pfaffian formula. This conclusion not only provides a new pathway for computing topological indices, but also makes it possible to generalize existing Pfaffian-based knowledge about TIs to high-order TIs, such as methods to obtain topological indices without a global gauge. As examples, we will show below that our Pfaffian formula allows us to obtain the index through examining only a small part of the Brillouin zone without using a global gauge, along a similar line as what has been achieved for TIs [77, 78]. It also provides a straightforward generalization of the Fu-Kane's parity criterion [22] to second-order

TIs if a four-fold rotoinversion symmetry is present, which demonstrates a direct connection between P_3 and symmetry indicators [10, 32].

3.1 Generalization of the Pfaffian formula

We consider a chiral second-order topological insulator (CSOTI) invariant under C_4T but without T or C_4 symmetry, and we set the rotational axis to be aligned with the z direction. The half-integer spin leads to $(C_4T)^4 = -1$. Due to the anti-unitary nature of C_4T and the half-integer spin of fermions, in analogy to Kramers doublets, all bands in our system shall show two-fold degeneracy at C_4T-invariant momenta, denoted as $K^4 = \{\Gamma, M, Z, A\}$, where $\Gamma = (0,0,0), M = (\pi,\pi,0), Z = (0,0,\pi), A = (\pi,\pi,\pi)$. Without losing generality, we assume that there is no accidental degeneracy beyond what is required by these Kramers pairs, because accidental degeneracy can always be lifted by perturbations without changing topological indices. Thus, for a system with N_{tot} bands and $2N$ occupied valance bands, a $2N \times 2N$ unitary sewing matrix for the symmetry operator C_4T can be defined

$$B_{mn}(\boldsymbol{k}) = \langle u_m(C_4T\boldsymbol{k})|C_4T|u_n(\boldsymbol{k})\rangle, \tag{3.3}$$

where m, n are valence band indices, $C_4T\boldsymbol{k} \equiv (k_y, -k_x, -k_z)$. In the absence of accidental degeneracy as assumed above, this $B(\boldsymbol{k})$ matrix is 2×2 block diagonal due to the Kramers pairs, i.e., $B(\boldsymbol{k}) = diag(B_1, B_2, ..., B_N)$ with each $B_r(\boldsymbol{k})$ being 2×2 unitary matrices for $r = 1, 2, ..., N$.

We parameterize the 3D Brillouin zone torus T^3 as a cube $I^3 = [-\pi,\pi]\times[-\pi,\pi]\times[-\pi,\pi]$ with the $\pm\pi$ surfaces identified by periodic boundary condition. The top and bottom surfaces of this cube $k_z = \pm\pi$ are invariant under C_4T and should have vanishing Chern number. The system also has C_2 symmetry along z, and the side surfaces $k_x = \pm\pi$ and $k_y = \pm\pi$ are invariant under C_2 after identifying the surfaces

at $+\pi$ and $-\pi$. This in-plane C_2 symmetry makes the Chern number at these side surfaces vanish as well. This means all six surfaces of the cube I^3 have zero Chern number, and according to Ref.[72] there exists a global gauge such that the wave functions are smooth and periodic in the whole Brillouin zone torus. In this global gauge each block $B_r(\boldsymbol{k})$ $(r = 1, ..., N)$ of the C_4T sewing matrix is smooth and we can further make $\det[B_r(\boldsymbol{k})] = 1$ for all $\boldsymbol{k}$ in the BZ [72]. Therefore, as a function of momentum, each $B_r(\boldsymbol{k})$ defines a smooth map from the 3D BZ to the linear space formed by all SU(2) matrices. In the language of differential manifold, a 3D BZ is a three-torus T^3, while SU(2) is diffeomorphic to a three-sphere S^3, and thus B_r defines a map $T^3 \to S^3$. For such a map, there exists an integer topological index, i.e. the degree $\deg[B_r]$, which measures how many times the T^3 wraps around the S^3:

$$\deg[B_r] = -\int \frac{\mathrm{d}^3k}{24\pi^2}\epsilon^{abc}\,\mathrm{Tr}\left[\left(B_r\partial_a B_r^\dagger\right)\left(B_r\partial_b B_r^\dagger\right)\left(B_r\partial_c B_r^\dagger\right)\right] \tag{3.4}$$

where $\partial_a = \partial/\partial k_a$ and a, b, c can take values of x, y, z.

It is known that the index P_3 in Eq.(3.1) is quantized in the presence of C_4T, and it can be rewritten via the C_4T sewing matrix [27, 48, 73]

$$2P_3 = -\frac{1}{24\pi^2}\int \mathrm{d}^3\boldsymbol{k}\epsilon^{abc}\,\mathrm{Tr}\left[\left(B\partial_a B^\dagger\right)\left(B\partial_b B^\dagger\right)\left(B\partial_c B^\dagger\right)\right].$$

For a block diagonal B matrix, this integral reduces to

$$2P_3 = \sum_{r=1}^{N}\deg[B_r] \tag{3.5}$$

where $\deg[B_r]$ is the degree of the map $B_r : T^3 \to S^3$ discussed above. There are some general properties for the degree of a map. For a generic smooth map $G : T^3 \to \mathrm{SU}(2)$, its degree $\deg[G]$ defined according to Eq.(3.4) is always quantized to an integer and

satisfies

$$\deg[G^\dagger] = -\deg[G], \quad \deg[G^*] = \deg[G], \quad \deg[G^{\mathrm{T}}] = -\deg[G] \tag{3.6}$$

With another smooth map $G' : T^3 \to SU(2)$, the matrix product GG' also defines a smooth map that satisfies:

$$\deg[GG'] = \deg[G] + \deg[G'] \tag{3.7}$$

If we view $G(\boldsymbol{k})$ and $G(C_4T\boldsymbol{k})$ as two maps that send $\boldsymbol{k} \in T^3$ to $SU(2)$, then

$$\deg[G(C_4T\boldsymbol{k})] = -\deg[G(\boldsymbol{k})] \tag{3.8}$$

More details about these properties are discussed in Appendix B.2. It is worthwhile to emphasize that only the module 2 of $2P_3$ (or $\deg[B_r]$) is gauge invariant and thus has real physical meaning. This conclusion can be checked by noticing that a gauge transformation can change the degree by an even integer, i.e. under $|u_n(\boldsymbol{k})\rangle \to \sum_{m\in occ}|u_m(\boldsymbol{k})\rangle U_{mn}(\boldsymbol{k})$, $B(\boldsymbol{k}) \to U^\dagger(C_4T\boldsymbol{k})B(\boldsymbol{k})U^*(\boldsymbol{k})$ and $\deg[B] \to \deg[B]+2\deg[U]$. Therefore we will only keep track of the mod 2 of the degree, which will be denoted as $\deg_2[B_r]$.

The mod 2 of the degree can be easily calculated through a counting technique, if we realize that the degree counts how many times the original spaces wraps around the target space. Here, we first demonstrate this technique using a simple example: a map between 1-spheres $f : S^1 \to S^1$ shown in Fig.(3.2). To get $\deg_2[f]$, we take any non-singular point in the target space and count how many points in the original space are mapped to this target point under f. If this number is n, then $\deg_2[f] = n \ mod \ 2$.

For $B_r : T^3 \to S^3$, it turns out that a specific gauge can be chosen, which allows the counting technique to be easily adopted. Because $C_2 = -(C_4T)^2$, C_2 is also a

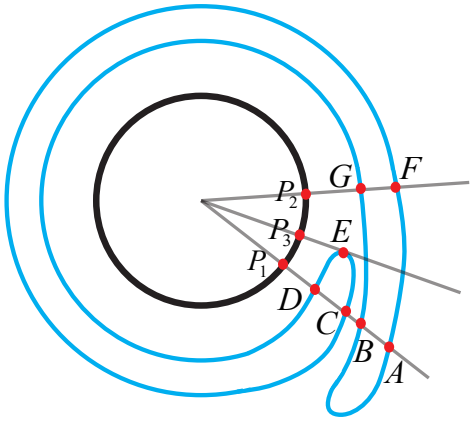

Figure 3.2: Illustration of a map $f : S^1 \to S^1$ with degree 0. The black circle is the target space and the blue line demonstrates the map from the original space to this circle. To calculate $\deg_2[f]$, we can pick a non-singular point like P_1 or P_2 in the target space and count the number of points that are mapped to it. There are four points mapped to P_1 and two points to P_2, therefore $\deg_2[f] = 4 \ mod \ 2 = 2 \ mod \ 2 = 0$. Note that we cannot choose the point P_3 to calculate the degree because the map at point E is singular.

symmetry of the system, therefore we can define a unitary $2N \times 2N$ sewing matrix for C_2:

$$D_{mn}(\boldsymbol{k}) = \langle u_m(C_2\boldsymbol{k})|C_2|u_n(\boldsymbol{k})\rangle, \tag{3.9}$$

where $C_2\boldsymbol{k} \equiv (-k_x, -k_y, k_z)$. In Appendix B.1 we show that the identities $C_2 = -(C_4T)^2$ and $(C_2)^2 = -1$ impose a relation between the sewing matrices of C_2 and C_4T:

$$D(\boldsymbol{k}) = -B(C_4T\boldsymbol{k})B^*(\boldsymbol{k}) \quad \text{and} \quad D(C_2\boldsymbol{k}) = -D^\dagger(\boldsymbol{k}) \tag{3.10}$$

With these properties of sewing matrices, we can find a smooth and periodic gauge in the Brillouin zone so that $D(\boldsymbol{k})$ is independent of $\boldsymbol{k}$:

$$D(\boldsymbol{k}) = diag(i\sigma_z, i\sigma_z, ..., i\sigma_z) \tag{3.11}$$

To prevent interrupting the logic flow, we postpone the construction of this special gauge to Section 3.1.1. With this gauge choice, Eq.(3.10) implies

$$B_r(C_4T\boldsymbol{k}) = -i\sigma_z B_r^{\mathrm{T}}(\boldsymbol{k}) \tag{3.12}$$

This condition has remarkable consequences. If $\boldsymbol{k}$ is a C_4T invariant point, Eq. (3.12) implies

$$B_r(\boldsymbol{K}) = \pm\frac{i}{\sqrt{2}}(\sigma_x + \sigma_y) \equiv A_\pm,\ \boldsymbol{K} \in K^4, \tag{3.13}$$

where $K^4 = \{\Gamma, M, Z, A\}$ represents C_4T invariant points as defined early on, i.e., at C_4T invariant points, B_r can only take one of these two distinct values $A_\pm$. On the other hand, if $\boldsymbol{k}$ is not a C_4T invariant point and if $B_r(\boldsymbol{k}) = A_\pm$, then Eq.(3.12) implies $B_r(C_4T\boldsymbol{k}) = B_r(\boldsymbol{k}) = A_\pm$. Hence if some $\boldsymbol{k} \notin K^4$ is mapped to A_+, there must be one (or three) additional momentum point (related to each other by C_4T) which is also mapped to A_+, and the same is true for A_-. Therefore if we choose A_+ (or A_-) as the special point to perform the counting described above, as far as $\deg_2[B_r]$ is concerned, only the four C_4T invariant points need to be considered, because any other point contributes even numbers to the counting. This requires the map at C_4T invariant points to be non-singular, e.g., we cannot use point E in Fig.(3.2) to perform the degree counting. We show in Section 3.1.2 that the map is indeed non-singular and this degree counting method is valid. In summary, for each B_r, we only need to examine the four C_4T invariant points (K^4). If n_r of these four points are mapped to A_+ (and thus $4 - n_r$ to A_-), then $\deg_2[B_r] = n_r \ mod\ 2$.

Now we relate this n_r to a Pfaffian. For any $\boldsymbol{k}$ point that is invariant under C_4, define

$$M_{mn}(\boldsymbol{k}) = \langle u_m(\boldsymbol{k})|\Theta|u_n(\boldsymbol{k})\rangle,\ \ \Theta = \frac{C_4T + C_4^{-1}T}{\sqrt{2}}, \tag{3.14}$$

where m, n are valence band indices. Θ here is a linear superposition of symmetry operators. For C_4-invariant $\boldsymbol{k}$ points, both C_4T and $C_4^{-1}T$ bring $\boldsymbol{k}$ to the same momentum, therefore $\Theta|u_n(\boldsymbol{k})\rangle$ has a well-defined momentum. Furthermore, at C_4-invariant momenta $(C_4)^4 = -1$ implies $(C_4)^2 = -(C_4)^{-2}$, together with $T^2 = -1$ lead to

$$\Theta^2 = \left(\frac{C_4T + C_4^{-1}T}{\sqrt{2}}\right)^2 = -\frac{(C_4)^2 + (C_4)^{-2} + 2}{2} = -1 \tag{3.15}$$

This implies Θ is an operator that can impose the Kramers degeneracy similar to time-reversal, because Θ is an anti-unitary operator that square to -1. Eq.(3.15) also implies if $|u_n(\boldsymbol{k})\rangle$ is normalized, then the state $\Theta|u_n(\boldsymbol{k})\rangle$ is also normalized. Note that Eq.(3.14) is similar to Eq.(2.5) but they are distinct quantities defined for different systems, where the time-reversal operator T is replaced by Θ. As shown in Appendix B.1, for every C_4-invariant $\boldsymbol{k}$ point the M matrix in Eq.(3.14) is anti-symmetric:

$$M(\boldsymbol{k}) = -M(\boldsymbol{k})^{\mathrm{T}} \tag{3.16}$$

And the proof is similar to Eq.(2.6). When the C_4 matrix is independent of $\boldsymbol{k}$, $M(\boldsymbol{k})$ is anti-symmetric for every momentum in the Brillouin zone. We also show in Appendix B.1 that at C_4T invariant points $\boldsymbol{K} \in K^4$, $M(\boldsymbol{K})$ is unitary and satisfies:

$$M(\boldsymbol{K}) = \left(B(\boldsymbol{K}) - B^{\mathrm{T}}(\boldsymbol{K})\right)/\sqrt{2} \tag{3.17}$$

Now we choose the special gauge in which Eq.(3.11) is satisfied. At each $\boldsymbol{K} \in K^4$, $M(\boldsymbol{K})$ is block diagonal $M(\boldsymbol{K}) = diag(M_1, M_2, ..., M_N)$. From Eq. (3.13) we know that $B_r(\boldsymbol{K}) = A_+$ or A_- and Eq.(3.17) implies $\mathrm{Pf}[M_r(\boldsymbol{K})] = +1$ or -1 respectively. Therefore, counting n_r is identical to counting the number of C_4T invariant momentum points with $\mathrm{Pf}[M_r(\boldsymbol{K})] = +1$, i.e., $(-1)^{\deg_2[B_r]} = (-1)^{n_r} = \prod_{\boldsymbol{K}\in K^4} \mathrm{Pf}[M_r(\boldsymbol{K})]$,

and when contributions from all valence bands are combined together, we have

$$(-1)^{2P_3} = \prod_{\boldsymbol{K}\in K^4} \frac{\mathrm{Pf}[M(\boldsymbol{K})]}{\sqrt{\det[B(\boldsymbol{K})]}} \tag{3.18}$$

This equation generalizes the FKM Pfaffian formula [16, 17] to systems without time-reversal symmetry, via replacing the T operator with a new combination $\Theta = (C_4 T + C_4^{-1} T)/\sqrt{2}$.

On the r.h.s. of Eq. (3.18), we added by hand a denominator $\sqrt{\det B}$. In the gauge we choose above, this quantity is unity and thus doesn't contribute anything. However, this denominator is important, because it makes the r.h.s. gauge invariant. Thus, although our conclusion is based on a specific gauge, it remains valid regardless of gauge choices, as long as $B(\boldsymbol{k})$ remains smooth and a unique sign is chosen for the square root for a continuous branch of $\sqrt{\det[B(\boldsymbol{k})]}$, which can always be achieved because $B(\boldsymbol{k})$ is unitary for every $\boldsymbol{k}$. To demonstrate this gauge invariance, here we perform a generic gauge transformation $|u_n(\boldsymbol{k})\rangle \to |u_j(\boldsymbol{k})\rangle U_{jn}(\boldsymbol{k})$. Because $\mathrm{Pf}[BAB^{\boldsymbol{T}}] = \mathrm{Pf}[A]\det[B]$ and $\det[BAB^{\boldsymbol{T}}] = \det[A]\det[B]^2$, the gauge transformation implies that $\mathrm{Pf}[M(\boldsymbol{K})] \to \mathrm{Pf}[M(\boldsymbol{K})]\det[U(\boldsymbol{K})]^*$ and $\sqrt{\det[B(\boldsymbol{K})]} \to \sqrt{\det[B(\boldsymbol{K})]}\det[U(\boldsymbol{K})]^*$. Hence the effect of the gauge transformation cancels in Eq. (3.18).

3.1.1 Explicit transformation to make C_2 sewing matrix constant

In this section we construct the gauge transform to make Eq.(3.11) valid. In the gauge in which the C_4T sewing matrix $B(\boldsymbol{k})$ is smooth and $\det[B(\boldsymbol{k})] = 1$, the C_2 sewing matrix $D(\boldsymbol{k})$ is also smooth and $\det[D(\boldsymbol{k})] = 1$ due to Eq.(3.10). We want to find a smooth gauge transformation $|u_n(\boldsymbol{k})\rangle \to \sum_{j\in occ}|u_j(\boldsymbol{k})\rangle \tilde{U}_{jn}(\boldsymbol{k})$ where $\tilde{U} \in \mathrm{SU}(2N)$ to make C_2 sewing matrix $D(\boldsymbol{k}) = diag(i\sigma_z, i\sigma_z, ..., i\sigma_z)$ for all momenta in the BZ. Since we assume no accidental degeneracy other than Kramers degeneracy, D is block diagonal with each block being SU(2). Therefore the problem reduce

from SU($2N$) to SU(2). Denote $D_r(\boldsymbol{k})$ as one of the SU(2) block, under the gauge transformation $D_r(\boldsymbol{k}) \to U^\dagger(C_2\boldsymbol{k})D_r(\boldsymbol{k})U(\boldsymbol{k})$. Since $D_r \in$ SU(2), we can parameterize it as

$$D_r(\boldsymbol{k}) = \exp[i(\pi/2 + \delta(\boldsymbol{k}))\hat{n}(\boldsymbol{k}) \cdot \sigma], \tag{3.19}$$

where $\delta(\boldsymbol{k}) \in [-\frac{\pi}{2}, \frac{\pi}{2}]$ and $\hat{n} = (n_x, n_y, n_z)$ is a unit vector that can be interpreted as the axis of the SU(2) rotation, and $2(\pi/2 + \delta) \in [0, 2\pi]$ is the angle of rotation. The fact that $D_r(C_2\boldsymbol{k}) = -D_r^\dagger(\boldsymbol{k})$ implies

$$\delta(\boldsymbol{k}) = -\delta(C_2\boldsymbol{k}), \quad \hat{n}(\boldsymbol{k}) = \hat{n}(C_2\boldsymbol{k}) \tag{3.20}$$

Because $D_r(\boldsymbol{k}) = -B_r(C_4T\boldsymbol{k})B_r^*(\boldsymbol{k})$ and $B_r(C_4T\boldsymbol{k})$ has the opposite degree to $B_r^*(\boldsymbol{k})$, the degree of $D_r(\boldsymbol{k})$ is zero and the winding is trivial. We will first find a transformation to make $\delta(\boldsymbol{k}) = 0$. This can be achieved by choosing $R(\boldsymbol{k}) = \exp[-i\frac{1}{2}\delta(\boldsymbol{k})\hat{n}(\boldsymbol{k})\cdot\sigma]$. Then $R(C_2\boldsymbol{k}) = \exp[i\frac{1}{2}\delta(\boldsymbol{k})\hat{n}(\boldsymbol{k}) \cdot \sigma]$ and

$$\begin{aligned} R^\dagger(C_2\boldsymbol{k})D_r(\boldsymbol{k})R(\boldsymbol{k}) &= \exp[-i\frac{1}{2}\delta(\boldsymbol{k})\hat{n}(\boldsymbol{k}) \cdot \sigma] \exp[i(\pi/2 + \delta(\boldsymbol{k}))\hat{n}(\boldsymbol{k}) \cdot \sigma] \\ &\quad \exp[-i\frac{1}{2}\delta(\boldsymbol{k})\hat{n}(\boldsymbol{k}) \cdot \sigma] \\ &= \exp[i(\pi/2)\hat{n}(\boldsymbol{k}) \cdot \sigma] = i\hat{n}(\boldsymbol{k}) \cdot \sigma \end{aligned} \tag{3.21}$$

Now the target space is determined by unit vector $\hat{n}$ and is isomorphic to a subspace of S^2. Since the winding is trivial, there exists a similarity transformation $w(\boldsymbol{k}) \in$ SU(2) to bring each axis $\hat{n}(\boldsymbol{k})$ to $+\hat{z}$ direction:

$$w^\dagger(\boldsymbol{k})(i\hat{n}(\boldsymbol{k}) \cdot \sigma)w(\boldsymbol{k}) = i\sigma_z \tag{3.22}$$

See Fig.(3.2) for an analogy of a map $f : S^1 \to S^1$. The map f has degree 0, therefore the target of each $\boldsymbol{k}$ can be continuous deformed to the north pole by either

a clockwise deformation (for points C, D, E) or a counter clockwise deformation (for points A, B, F, G). Now we show that $w(\boldsymbol{k}) = w(C_2\boldsymbol{k})$. Suppose momentum $\boldsymbol{k_0}$ corresponds to point A in Fig.(3.2). The fact that $\hat{n}(\boldsymbol{k}) = \hat{n}(C_2\boldsymbol{k})$ means $C_2\boldsymbol{k_0}$ must be one of B, C, D points so that they have the same $\hat{n}$. If $C_2\boldsymbol{k_0}$ corresponds to C or D, then if we let $\boldsymbol{k}$ vary on a continuous path of momentum points from A to F, the point $C_2\boldsymbol{k}$ must have a discontinuous jump at E, which is impossible. Therefore $C_2\boldsymbol{k_0}$ has to be point B, which is in the same branch as A. Therefore if transformation $w(\boldsymbol{k_0})$ can bring A to the north pole, so can it bring B. Hence we have $w(\boldsymbol{k}) = w(C_2\boldsymbol{k})$.

Now the transformation to bring $D_r(\boldsymbol{k})$ to $i\sigma_z$ is just $U(\boldsymbol{k}) = R(\boldsymbol{k})w(\boldsymbol{k})$, so that

$$\begin{aligned} D_r(\boldsymbol{k}) &\rightarrow U^\dagger(C_2\boldsymbol{k})D_r(\boldsymbol{k})U(\boldsymbol{k}) \\ &= w^\dagger(C_2\boldsymbol{k})R^\dagger(C_2\boldsymbol{k})D_r(\boldsymbol{k})R(\boldsymbol{k})w(\boldsymbol{k}) \\ &= w^\dagger(\boldsymbol{k})(i\hat{n}(\boldsymbol{k})\cdot\sigma)w(\boldsymbol{k}) = i\sigma_z \end{aligned} \tag{3.23}$$

Therefore, we have constructed the gauge with $D(\boldsymbol{k})$ being a constant matrix: $D(\boldsymbol{k}) = diag(i\sigma_z, ..., i\sigma_z)$. The nice thing is that this construction of gauge transform is only needed as a theoretical proof, and it is not needed in the practical computation of the topological index.

3.1.2 Issues about singular points in degree counting

When we use the degree counting technique on C_4T invariant points $\boldsymbol{K} \in K^4$ to calculate the degree of $B_r(\boldsymbol{k})$, there is a requirement that the map at $\boldsymbol{K}$ is not singular. If we parameterize the map $B_r(\boldsymbol{k}) = \exp[i\theta\hat{n}\cdot\sigma]$ with constrain $n_x^2 + n_y^2 + n_z^2 = 1$, then the non-singular condition is that the determinant of Jacobian matrix at $\boldsymbol{K}$ is nonzero: $\det\left[\frac{\partial(\theta, n_\alpha, n_\beta)}{\partial(k_x, k_y, k_z)}\right] \neq 0$ for some $\alpha, \beta \in \{x, y, z\}$.

In general we can always do a small perturbation to the map to avoid the singular points. However, if the symmetry requires the map to be singular, then the singularity

is not avoidable. One such example is the sewing matrix $D_r(\boldsymbol{k}) \in SU(2)$ for C_2. Symmetry requires $D_r(C_2\boldsymbol{k}) = -D_r^\dagger(\boldsymbol{k})$ hence $\hat{n}(C_2\boldsymbol{k}) = \hat{n}(\boldsymbol{k})$. Thus near C_2 invariant points $\hat{n}(k_x, k_y, k_z) = \hat{n}(-k_x, -k_y, k_z)$ for small k_x, k_y. Therefore $\frac{\partial \hat{n}}{\partial k_x} = \frac{\partial \hat{n}}{\partial k_y} = 0$, leading to a zero determinant of Jacobian. This means the map $D_r(\boldsymbol{k})$ at every C_2 invariant point must be singular and the degree counting technique does not work for it.

Fortunately there is no such symmetry restriction for C_4T sewing matrix $B_r(\boldsymbol{k})$. Consider momentum points near $\Gamma = (0, 0, 0)$. In the gauge where $D(\boldsymbol{k}) = diag(i\sigma_z, ..., i\sigma_z)$, symmetry requires

$$\begin{aligned} B_r(C_4T\boldsymbol{k}) &= B_r(k_y, -k_x, -k_z) = -i\sigma_z B^{\mathrm{T}}(\boldsymbol{k}) \\ B_r(\Gamma) &= \pm\frac{i}{\sqrt{2}}(\sigma_x + \sigma_y) \end{aligned} \tag{3.24}$$

We can give an example of B_r that is non-singular near Γ and respect the symmetry requirement. Keep only first-order terms in k, this example is given by

$$B_r(\boldsymbol{k}) = k_x + i(\frac{1}{\sqrt{2}} + k_z)\sigma_x + i(\frac{1}{\sqrt{2}} - k_z)\sigma_y + ik_y\sigma_z + O(k^2) \tag{3.25}$$

It can be checked that this example is consistent with Eq.(3.24), and the determinant of Jacobian $\det\left[\frac{\partial(\theta, n_x, n_z)}{\partial(k_x, k_y, k_z)}\right] \neq 0$. Therefore there is no symmetry restriction for B_r to be singular at C_4T invariant points and we are legitimate to apply the degree counting technique.

3.2 Application of the Pfaffian formula

The generalized Pfaffian formula Eq.(3.18) is the main result in this chapter. In this section we will show that it can generalize many important conclusions in first-order Z_2 topological insulators to higher order topological insulators. In particular, it

provides a gauge-independent way to compute the topological index, and the parity criterion can be generalized to S_4 criterion.

3.2.1 Gauge-independent formula for P_3

We will show that Eq.(3.18) can be expressed as a 2D integral without the need of a smooth global gauge, which greatly reduces computational cost for evaluating P_3, similar to what has been achieved in TIs [77, 78]. For C_4-invariant $\boldsymbol{k}$ points, we define another matrix for the valence bands

$$\omega_{mn}(\boldsymbol{k}) = \langle u_m(-\boldsymbol{k})|\Theta|u_n(\boldsymbol{k})\rangle \tag{3.26}$$

with Θ defined in Eq. (3.14). As shown in Appendix B.1, at C_4-invariant momenta (straight lines $Z\Gamma\overline{Z}$ and $AM\overline{A}$ in Fig.(3.3)) $\omega(\boldsymbol{k})$ is unitary and $\det[\omega(\boldsymbol{k})] = \det[B(\boldsymbol{k})]$. Because $\omega(\boldsymbol{K}) = M(\boldsymbol{K})$ for $\boldsymbol{K} \in K^4$, Eq.(3.18) can thus be rewritten as

$$(-1)^{2P_3} = \prod_{\boldsymbol{K}\in K^4} \frac{\mathrm{Pf}[\omega(\boldsymbol{K})]}{\sqrt{\det[\omega(\boldsymbol{K})]}} \tag{3.27}$$

As Fu and Kane [17] have shown for TIs, Eq.(3.27) can also be expressed as an integral

$$2P_3 = \frac{1}{2\pi}\left[\oint_{\partial\tau_{1/2}} \mathcal{A}d\ell - \int_{\tau_{1/2}} d\tau\mathcal{F}\right] \ mod\ 2 \tag{3.28}$$

Here $\tau_{1/2}$ refers to the rectangle $Z\overline{ZA}A$ in Fig.(3.3) and $\partial\tau_{1/2}$ is its boundary. $\mathcal{A}$ and $\mathcal{F}$ are the abelian Berry connection and Berry curvature inside $\tau_{1/2}$. If we label each wavefunction $|u_n(\boldsymbol{k})\rangle$ as $|u_r^s(\boldsymbol{k})\rangle$, where $r = 1, ..., N$ labels different Kramers pairs and $s = \mathrm{I}, \mathrm{II}$ distinguishes the two states in a Kramers pair, there is a gauge fixing

condition at the boundary $Z\overline{Z}$ and $A\overline{A}$ for Eq.(3.28) to be valid:

$$\left|u_r^{\mathrm{I}}(-\boldsymbol{k})\right\rangle = \Theta\left|u_r^{\mathrm{II}}(\boldsymbol{k})\right\rangle \tag{3.29}$$

$$\left|u_r^{\mathrm{II}}(-\boldsymbol{k})\right\rangle = -\Theta\left|u_r^{\mathrm{I}}(\boldsymbol{k})\right\rangle \tag{3.30}$$

The formula here is slightly different from the one used in Ref. [17], because T is now replaced by $\Theta = (C_4T + C_4^{-1}T)/\sqrt{2}$. But for Eqs. (3.29) and (3.30), because it is evaluated only along $Z\overline{Z}$ and $A\overline{A}$, where $\Theta\boldsymbol{k} = T\boldsymbol{k} = -\boldsymbol{k}$, the action of T and Θ on momentum becomes the same and thus derivations in Ref [17] can be generalized to systems studied here by simply replacing T by Θ.

Eq.(3.28) enables us to develop efficient numerical techniques to calculate P_3 without the need for a global gauge, following similar line of thinking as has been achieved for TIs [77, 78]. The method proceeds as the following. First, let us select a discrete mesh in $\tau_{1/2}$ and define $Q_{\mu,mn}(\boldsymbol{k}) = \langle u_m(\boldsymbol{k})|u_n(\boldsymbol{k}+\boldsymbol{s_\mu})\rangle$, where $\mu = 1, 2$ and s_μ is the mesh step size in the two directions in $\tau_{1/2}$. Apply gauge fixing condition Eqs. (3.29) and (3.30) to the boundary $\partial\tau_{1/2}$. Let $L_\mu(\boldsymbol{k}) = \det[Q_\mu]/|\det[Q_\mu]|$ and $\tilde{A}_\mu(\boldsymbol{k}) = \ln L_\mu(\boldsymbol{k})$, $\tilde{F}(\boldsymbol{k}) = \ln\left(L_1(\boldsymbol{k})L_2(\boldsymbol{k}+s_1)L_1^{-1}(\boldsymbol{k}+s_2)L_2^{-1}(\boldsymbol{k})\right)$ where the imaginary part of all the logarithm are restricted to $(-\pi, \pi]$. Then $2P_3$ can be calculated through

$$2P_3 = \frac{1}{2i\pi}\left[\sum_{\boldsymbol{k}\in\partial\tau_{1/2}} \tilde{A}_\mu(\boldsymbol{k}) - \sum_{\boldsymbol{k}\in\tau_{1/2}} \tilde{F}(\boldsymbol{k})\right] \; mod\ 2, \tag{3.31}$$

where the direction μ should be along the positive direction of $\partial\tau_{1/2}$. This numerical technique does not require a smooth gauge and is thus convenient to implement. This method has been well-known for 2D and 3D TI, and is now generalized to 3D HOTI without time-reversal symmetry. Remarkably, Eq.(3.31) shows that in order to calculate the magnetoelectric polarization P_3 for a 3D system, we only need to investigate a 2D subspace in the Brillouin zone without the requirement of a smooth gauge.

Eq.(3.18) also allows us to determine P_3 though the zero of $\mathrm{Pf}[M(\boldsymbol{k})] \equiv p_f(\boldsymbol{k})$. Under a smooth gauge with $\det[B] = 1$, $p_f(\boldsymbol{K}) = \pm 1$ at $\boldsymbol{K} \in K^4$. Hence Eq.(3.18) can be interpreted as the sum of phase change of $p_f(\boldsymbol{k})$ from Z to Γ and from M to A as shown in Fig.(3.3), i.e., $2P_3 = (\pi i)^{-1} \int_L d\boldsymbol{k} \cdot \boldsymbol{\nabla} \log p_f(\boldsymbol{k})$ where L is the combination of two straight pathes $(Z \to \Gamma) + (M \to A)$. As proved in Appendix B.1, $p_f(\boldsymbol{k}) = p_f(C_4 T \boldsymbol{k})^* \det[B(\boldsymbol{k})]$, and thus when $\det[B] = 1$ and $\boldsymbol{k} \in L$, $p_f(\boldsymbol{k}) = p_f(-\boldsymbol{k})^*$. Therefore the phase change of $p_f(\boldsymbol{k})$ from Z to Γ is the same as that from Γ to $\overline{Z}$. With this fact we can extend the integration path L to be $\partial\tau_{1/2}$ and divide by 2 to get $2P_3$, which gives

$$2P_3 = \frac{1}{2\pi i} \oint_{\partial\tau_{1/2}} d\boldsymbol{k} \cdot \boldsymbol{\nabla} \log \mathrm{Pf}[M(\boldsymbol{k})] \tag{3.32}$$

This is a generalization of the result by Kane and Mele [16], via replacing T by Θ. The r.h.s. of the equation measures the phase winding of $\mathrm{Pf}[M(\boldsymbol{k})]$ around the boundary of the 2D area $\tau_{1/2}$. This implies that the gauge-invariant line quantity g [45] described in the previous chapter can be applied to calculate P_3. Specifically, we can use the definition of g in Eq.(2.15) with the M matrix given by Eq.(3.14):

$$g_\Theta(\boldsymbol{k}_a, \boldsymbol{k}_b) = \frac{\mathrm{Pf}[M(\boldsymbol{k}_b)]}{\mathrm{Pf}[M(\boldsymbol{k}_a)]} \det \left[\langle u_m(\boldsymbol{k}_a) | \prod_{\boldsymbol{k}_i \in \overline{\boldsymbol{k}_a \boldsymbol{k}_b}}^{\boldsymbol{k}_a \leftarrow \boldsymbol{k}_b} P_{\boldsymbol{k}_i} | u_n(\boldsymbol{k}_b) \rangle \right] \tag{3.33}$$

Here the sub-index Θ means the M matrix contains Θ as in Eq.(3.14). Then following the derivation that leads to Eq.(2.19), we get from Eq.(3.32):

$$2P_3 = \frac{1}{2\pi i} \int_{Z'}^{Z} d\boldsymbol{k} \cdot \nabla \log \overline{g}_\Theta(\boldsymbol{k}) \mod 2 \tag{3.34}$$

Here $\overline{g}_\Theta(\boldsymbol{k}) = g_\Theta(\boldsymbol{k}, \boldsymbol{k} + \pi\hat{x} + \pi\hat{y})$ and the integral is along the straight path from Z' to Z. Therefore the magnetoelectric polarization P_3 can be expressed in terms of an

integral of the line quantity $g_\Theta(\boldsymbol{k}_a, \boldsymbol{k}_b)$. This method involves only gauge-independent objects, therefore a smooth gauge is not needed. Comparing with Eq.(3.31), Eq.(3.34) does not need the gauge fixing in Eq.(3.29) and (3.30). Eq.(3.31) and (3.34) are two different approaches to compute the topological index P_3 for higher-order topological insulators in 3D which does not require a smooth gauge, and only a 2D subspace of the Brillouin zone is needed in the computation.

We can also find an alternative interpretation for the physical meaning of Eq.(3.32). When the C_4 matrix is independent of $\boldsymbol{k}$, the M matrix is anti-symmetric in the whole Brillouin zone and $\mathrm{Pf}[M(\boldsymbol{k})]$ is a well-defined quantity for every $\boldsymbol{k}$. When $P_3 \neq 0$, Eq.(3.32) means there is a nontrivial phase winding of $\mathrm{Pf}[M(\boldsymbol{k})]$ around the 1D boundary $\partial\tau_{1/2}$, which implies the existence of points in $\tau_{1/2}$ with $\mathrm{Pf}[M(\boldsymbol{k})] = 0$. Therefore, $2P_3$ can be obtained by counting the number of nodal points with $\mathrm{Pf}[M(\boldsymbol{k})] = 0$ in $\tau_{1/2}$. More details will be demonstrated below using a tight-binding model. Interestingly, here we have shown that for a 3D HOTI, its topological index P_3 can be calculated by looking at the zeros of $\mathrm{Pf}[M(\boldsymbol{k})]$ in a single 2D plane ($\tau_{1/2}$). This is in direct contrast to first-order 3D TIs, where one needs to investigate two time-reversal-invariant 2D planes to determine the Z_2 index [80]. Eq.(3.32) also implies that if $\mathrm{Pf}[M(\boldsymbol{k})]$ is nonzero over $\tau_{1/2}$, then P_3 will automatically be trivial.

3.2.2 Topological diagnosis with additional S_4 symmetry

We will show that if the system has fourfold rotoinversion symmetry S_4 in addition to C_4T, then P_3 can be directly obtained by evaluating S_4 eigenvalues at high symmetry points. This conclusion is a generalization of the Fu-Kane's parity criterion [22] to HOTIs, with a key observation that $\tilde{S} = (S_4 + S_4^{-1})/\sqrt{2}$ and $\Theta = (C_4T + C_4^{-1}T)/\sqrt{2}$ can play the role of space inversion I and time reversal T respectively. This correspondence can be seen from the fact that $(\tilde{S})^2 = 1$ and $\tilde{S}\Theta = IT = S_4C_4T$, which is

a consequence of $(S_4)^4 = -1$ and $S_4 = IC_4^{-1}$. Define sewing matrix:

$$v_{mn}(\mathbf{k}) = \langle u_m(\mathbf{k})|S_4 C_4 T|u_n(\mathbf{k})\rangle \tag{3.35}$$

As shown in Appendix B.1, $v(\mathbf{k})$ is unitary and antisymmetric for every $\mathbf{k}$, and $\mathrm{Pf}[v(\mathbf{k})] = \mathrm{Pf}[v(C_4 T\mathbf{k})]^* \det[B(\mathbf{k})]$. We can make a gauge transformation to make $\mathrm{Pf}[v(\mathbf{k})] = 1$ (and thus $\det[B(\mathbf{k})] = 1$) for all $\mathbf{k}$, and $M(\mathbf{K})$ and $v(\mathbf{K})$ are linked together at $\mathbf{K} \in K^4$ through

$$\begin{aligned} M_{mn}(\mathbf{K}) &= \langle u_m(\mathbf{K})|\Theta|u_n(\mathbf{K})\rangle = \langle u_m(\mathbf{K})|\tilde{S}^2\Theta|u_n(\mathbf{K})\rangle \\ &= \eta_m(\mathbf{K})\langle u_m(\mathbf{K})|\tilde{S}\Theta|u_n(\mathbf{K})\rangle \\ &= \eta_m(\mathbf{K}) v_{mn}(\mathbf{K}) \end{aligned} \tag{3.36}$$

Hence $\det[M(\mathbf{K})] = \prod_{i=1}^{2N} \eta_i(\mathbf{K}) \det[v(\mathbf{K})]$. Because $\tilde{S}$ commutes with C_4T, bands in the same Kramers pair share identical $\tilde{S}$ eigenvalues, thus $\prod_{i=1}^{2N} \eta_i(\mathbf{K}) = \prod_{r=1}^{N} (\eta_r^{\mathrm{I}}(\mathbf{K}))^2$ where η_r^{I} is $\tilde{S}$ eigenvalue for each Kramers pair. Therefore

$$\det[M(\mathbf{K})] = \mathrm{Pf}[M(\mathbf{K})]^2 = \left(\prod_{r=1}^{N} \eta_r^{\mathrm{I}}(\mathbf{K}) \, \mathrm{Pf}[v(\mathbf{K})] \right)^2 \tag{3.37}$$

Eq.(3.36) shows that $\mathrm{Pf}[M(\mathbf{K})]$ is a polynomial of v_{mn} and η_r^{I}, and the square of this polynomial must equal to Eq.(3.37). When all $\eta_r^{\mathrm{I}} = 1$ we should have $M = v$ and $\mathrm{Pf}[M] = 1$. These conditions uniquely fix the polynomial to be $\mathrm{Pf}[M(\mathbf{K})] = \prod_{r=1}^{N} \eta_r^{\mathrm{I}}(\mathbf{K}) \, \mathrm{Pf}[v(\mathbf{K})] = \prod_{r=1}^{N} \eta_r^{\mathrm{I}}(\mathbf{K})$. Since $\det[B] = 1$ in this gauge, from Eq.(3.18) we get

$$(-1)^{2P_3} = \prod_{\boldsymbol{K} \in K^4} \prod_{r=1}^{N} \eta_r^{\mathrm{I}}(\boldsymbol{K}) \tag{3.38}$$

Here r runs over all occupied Kramers pairs, and K_4 is the set of S_4 invariant points and $\eta_r^{\mathrm{I}} = \pm 1$ is eigenvalue of $\tilde{S} = (S_4 + S_4^{-1})/\sqrt{2}$. Eq.(3.38) is a generalization of the

Fu-Kane parity criterion [22] to systems with S_4 but no inversion symmetry. It shows the magnetoelectric polarization P_3 can be determined by the eigenvalues of S_4. It is also consistent with results obtained using symmetry indicators [10, 32].

3.2.3 Numerical check of the Pfaffian formula

Here we use tight-binding models to demonstrate and to verify the Pfaffian formula we developed. Consider a four-band model with a Hamiltonian

$$\begin{aligned} H(\boldsymbol{k}) &= (\cos k_x + \cos k_y + \cos k_z - 2)\tau_z\sigma_0 + q_1 \sum_{i=x,y,z} \sin k_i \tau_x \sigma_i \\ &\quad + q_2 \sum_{j=x,y} \sin k_j \sin k_z \tau_y \sigma_j + q_3 \tau_x \sigma_0 \\ &\quad + p(\cos k_x - \cos k_y)\tau_y \sigma_0 \end{aligned} \tag{3.39}$$

Here $C_4 = \tau_0 e^{-i\frac{\pi}{4}\sigma_z}$, $T = -i\tau_0\sigma_y K$, $S_4 = \tau_z e^{i\frac{\pi}{4}\sigma_z}$. The Hamiltonian satisfies $H(C_4 T\boldsymbol{k})$ $= C_4 T H(\boldsymbol{k})(C_4 T)^{-1}$. The p term breaks C_4 and T symmetry but preserves S_4 and $C_4 T$. If p vanishes then the system becomes a 3D TI. The q_2 and q_3 terms break S_4 symmetry. When $q_2 = q_3 = 0$, S_4 symmetry is recovered and the model reduces to the one shown in Ref. [48]. In this case the Kramers pair in the valence bands at Γ has $\tilde{S}$ eigenvalue -1 and all other S_4 invariant points have $\tilde{S}$ eigenvalue $+1$. Thus by Eq. (3.38), we have $P_3 = 1/2$ and the system is a CSOTI. When small q_2 and q_3 are turned on, the band gap does not close and the system should still remain a CSOTI. Because the matrix of C_4 does not depend on $\boldsymbol{k}$, Pf$[M(\boldsymbol{k})]$ is well-defined for every momentum in the Brillouin zone. We calculate the zero of Pf$[M(\boldsymbol{k})]$ as shown in Fig.(3.3). The zeros form a loop penetrating $\tau_{1/2}$, giving rise to a phase winding of 2π in Pf$[M(\boldsymbol{k})]$. Therefore from Eq. (3.32), $P_3 = 1/2$. We also apply Eq. (3.31) and (3.34) separately to calculate the index, and we get $P_3 = 1/2$ as well. To verify our prediction we diagonalize the system with open boundary condition along k_x and k_y, and the spectra as a function of k_z is shown in Fig.(3.3). Gapless hinge states are

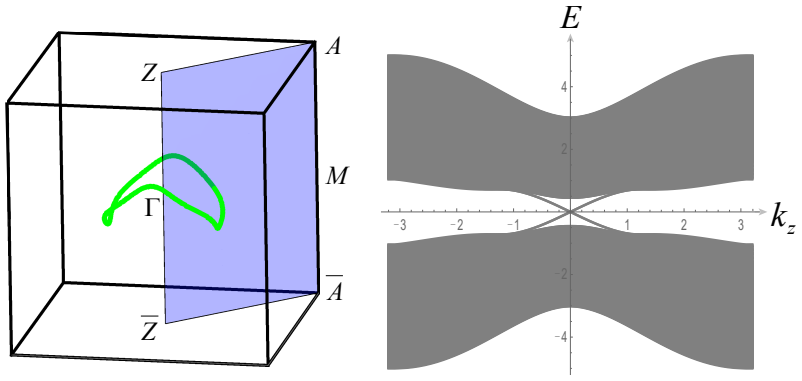

Figure 3.3: Left: schematic plot of the Brillouin zone. $\tau_{1/2}$ is the colored rectangle and $\partial\tau_{1/2}$ is its boundary. The green line represents the momenta with $\mathrm{Pf}[M(\boldsymbol{k})] = 0$ for the Hamiltonian shown in Eq. (3.39). The line of zero Pfaffian penetrates $\tau_{1/2}$, resulting in a phase winding of 2π in Eq. (3.32), which implies that $P_3 = 1/2$. Parameters used here are $p = 0.5, q_1 = 1, q_2 = 0.2, q_3 = 0.3$. Right: spectra of H as a function of k_z with open boundary condition along k_x and k_y with the same parameters. The existence of gapless hinge states suggests nontrivial topology.

found, which confirms that the system is a CSOTI with $P_3 = 1/2$.

We have generalized the Pfaffian formalism to higher-order topological insulators protected by C_4T symmetry as shown in Eq. (3.18) and its variations in Eqs. (3.31), (3.32) and (3.34). If the system also preserves a S_4 symmetry, P_3 can be obtained directly from S_4 eigenvalues at high symmetry momenta as in Eq.(3.38). Without S_4, we find that the topological index P_3 can be calculated by examining a single 2D surface $\tau_{1/2}$ as shown in Fig.(3.3) without the need of a smooth gauge, which greatly simplifies the calculation.

CHAPTER IV

Gapless Topological Phases: Topological Semimetals

Topological phases can also be defined for gapless systems. Contrary to gapped systems, in gapless systems there is no clear distinction between occupied and unoccupied bands because of the band crossing, and the concept of topology is different from the one introduced in Section 1.3, i.e., the notion of topology in gapless systems is not to classify different phases whose occupied bands cannot be adiabatic deformed to each other, and instead it classifies different types of robust band crossing that are topologically protected.

The crossing of two bands can usually be lifted by the hybridization between them, then the band crossing is avoided. As shown in Fig.(4.1), if two bands $E_1(k)$ and $E_2(k)$ cross each other, when there is a finite mixing term b, the energy of the hybridized bands become $E_{\pm}(k) = \frac{E_1(k)+E_2(k)}{2} \pm \sqrt{\left(\frac{E_1(k)-E_2(k)}{2}\right)^2 + |b|^2}$, then $E_+(k) \neq E_-(k)$ as long as $b \neq 0$, i.e., the band crossing is lifted. Therefore, the existence of robust band crossing needs a reason that protects it. The region of band crossing in momentum space can be isolated points such as Weyl or Dirac points [81, 82, 83, 84, 85, 86], or they can form one-dimensional closed loops which are called nodal lines [73, 87, 88, 89]. The notion of topology for gapless systems distinguishes different types of robust band crossing.

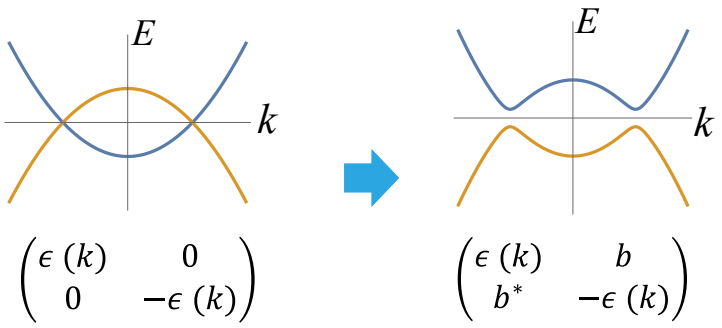

Figure 4.1: Illustration of avoid crossing of energy bands. A small hybridization b can gap out the band crossing.

For example, Weyl semimetals in 3D have band crossing at isolated Weyl points in the bulk Brillouin zone. Near the Weyl point, the Hamiltonian for the two crossing bands can be approximated by $H(\boldsymbol{k}) \sim k_x\sigma_x + k_y\sigma_y + k_z\sigma_z$ with energy $E(\boldsymbol{k}) = \pm\sqrt{k_x^2 + k_y^2 + k_z^2}$. Then it can be seen that this band crossing cannot be gapped by small perturbation, because a perturbation such as $b\sigma_x$ only shifts the position of Weyl point from origin to $(-b, 0, 0)$ but it cannot gap out the crossing. The robustness of Weyl points can be understood from topology. If we draw a sphere S in the momentum space enclosing the Weyl point, then on the sphere the bands are gapped and the Chern number can be defined on this sphere for the bands below the gap. For Weyl points this Chern number is nonzero, which is called the chirality of the Weyl point. Because Chern number is quantized to integers and can only be changed when gap closes, a nonzero Chern number on this sphere implies there is a gap closing point enclosed by the sphere, otherwise we can always continuously deform the sphere to make its Chern number vanish. Therefore, the existence of Weyl points is protected by topology, and the topological index is the chirality. A Weyl point can be gapped out only when it meets another Weyl point with opposite chirality.

Band crossing can also be protected by symmetry. If the crossing points are at symmetry-invariant momentum and the symmetry enforces the hybridization term

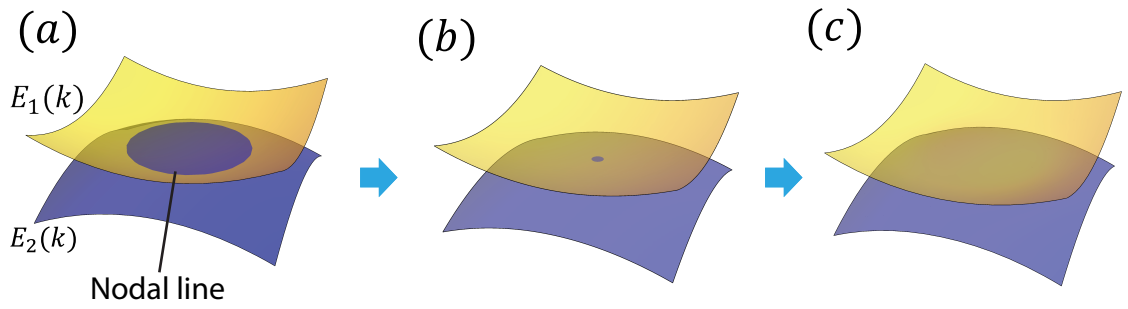

Figure 4.2: (a): A nodal line protected by the mirror symmetry in the mirror-invariant plane. (b,c): The nodal line can disappear after shrinking to a point.

to vanish, then the band crossing becomes robust. This scenario occurs for mirror-protected nodal lines [90, 91]. As shown in Fig.(4.2)(a), inside a mirror-invariant plane in the Brillouin zone the bands can be labeled by their eigenvalues of mirror symmetry. If two bands $E_1(\boldsymbol{k})$ and $E_2(\boldsymbol{k})$ with different mirror eigenvalues cross each other, then due to mirror symmetry the mixing term has to vanish and the band crossing remains, resulting in a mirror-protected nodal line. This nodal line is robust to small perturbations that preserve the mirror symmetry, but it can be gapped out after it shrinks to a point when the symmetry is still preserved, as shown in Fig.(4.2)(b,c).

There exists more robust nodal lines that cannot be gapped out even after it shrinks to a point. These nodal lines have nontrivial monopole charge [87], and they exist in systems with space-inversion I and time-reversal symmetry T and has negligible spin-orbit coupling ($T^2 = +1$). This can be demonstrated in a four-band Hamiltonian obtained near the nodal line:

$$\begin{aligned} H(\boldsymbol{k}) &= k_x\Gamma_1 + k_y\Gamma_2 + k_z\Gamma_3 + bV \\ &= k_x\tau_y\sigma_y + k_y\tau_y\sigma_x + k_z\tau_z\sigma_0 + b\tau_x\sigma_z \end{aligned} \tag{4.1}$$

Here σ, τ represent Pauli matrices. Note the anti-commutation relation $\{\Gamma_i, \Gamma_j\} =$

$2\delta_{ij},\ i,j \in \{1,2,3\}$ and the V matrix does not anti-commute with some other terms. This system has the product of time-reversal and space-inversion as a symmetry $IT = \tau_z\sigma_x K$ such that $ITH(\boldsymbol{k})(IT)^{-1} = H(\boldsymbol{k})$. The dispersion relation is given by:

$$E(\boldsymbol{k}) = \pm\sqrt{k_z^2 + \left(\sqrt{k_x^2 + k_y^2} \pm b\right)^2} \tag{4.2}$$

For each momentum, we label the bands by $E_1 \sim E_4$ with increasing energy. If we investigate the momenta at which the two middle bands cross ($E_2 = E_3$), it requires $E(\boldsymbol{k}) = 0$ in Eq.(4.2), leading to

$$k_z = 0 \text{ and } k_x^2 + k_y^2 = b^2 \tag{4.3}$$

This is the equation for the nodal line formed by band 2 and 3, which is a circle of radius b inside the xy plane in the momentum space. When we continuously deform the Hamiltonian so that b becomes small, the nodal line will gradually shrink to a nodal point. However, after b becomes zero and then changes sign, the nodal line does not disappear because b and $-b$ lead to the same nodal line configuration. This is am example where the nodal line cannot be destroyed by shrinking to a point. Note that the IT symmetry plays an crucial role here, because an additional term like $b'\tau_y\sigma_z$ can appear in the Hamiltonian without IT symmetry. This term anti-commutes with $\Gamma_{1\sim3}$ and it can gap out the nodal line. This type of nodal line is protected by a topological index called monopole charge, which is a Z_2 index defined only in the presence of IT symmetry. When the monopole charge is nontrivial, the nodal line cannot be destroyed by shrinking to a point, and it can disappear only after it annihilates with another nodal line with nontrivial monopole charge.

There is also a nodal line formed by band 1 and 2, which is a vertical nodal line given by $k_x = k_y = 0$, and similarly for band 3 and 4. Note that this vertical nodal line is linked with the circular nodal line formed by middle bands 2 and 3. This is

the linking structure pointed out in Ref [73]. A nodal line with nontrivial monopole charge is linked with nodal lines that come from the other band gaps. This linking structure requires the minimal model for this type of nodal line to have four bands.

4.1 Generic diagnosis scheme for nodal lines with nontrivial monopole charge

In our work [92], we systematically studied the conditions in which these nodal lines with nontrivial monopole charge will appear. In particular, for a system with space-inversion, time-reversal and rotational symmetry, our method can determine the number and configuration of these nodal lines in the Brillouin zone via the symmetry representations of the energy bands at high symmetry momenta. This approach does not require the high symmetry lines in the Brillouin zone to be gapped, which goes beyond Ref [93]. We also find novel cage-like nodal structures around high-symmetry line as well as the emergence of nodal lines with new types of monopole charge beyond the Z_2 classification in Ref [87].

The creation and annihilation of nodal lines with nontrivial monopole charge involve at least four bands due to the linking structure of nodal lines [73]. Therefore, we use a four-band tight binding model to study all the new types of nodal structures and their transitions. In a four-band model, having two conduction and two valence bands, respectively, we first show that the Hamiltonian can be simplified into one of the two special limits H_1 or H_2 in a smooth process without introducing new band crossings between conduction and valence bands. The relatively simple form, and the doubly degenerate spectrum of $H_{1,2}$ make easy the calculation of the band crossing positions and wave functions. The band inversion is then studied in the simplified Hamiltonian, where all topological nodes are necessarily point nodes. Defining the so called "parity Chern number" for the Fermi surface, we are able to classify the

types, configurations and parity Chern numbers of the nodal points for each type of band inversion. In fact, generalizing a discussion in Ref. [27], we can obtain the quantitative relations between the rotation and inversion eigenvalues of the inverted bands and the parity Chern number of the nodal point.

After the non-simplifying terms are added, H becomes non-degenerate, and the nodal points expand naturally into nodal lines. It can be expected that some quantum numbers of the nodal line, such as the parity Chern number, will be inherited from the former. To be more specific, a nodal point with parity Chern number 2 after non-simplifying terms evolves into either two nodal loops with unity monopole charge each, or into an interesting nodal cage with monopole charge 2, depending on the specific type of band inversion. A higher-than-unity monopole charge will be defined in due course, under the assumption that near the Fermi energy the orbitals have the same twofold rotation eigenvalue. This made charge-2 nodal lines one of the fragile topological band crossings [94, 95], in analogy to the recently studied fragile topological gapped states.

Therefore, we complete the theory on band inversion induced topological nodal lines in the presence of inversion, time-reversal and spin rotation symmetries. We work with the assumption that the nodal lines are formed by small band inversion, i.e., the inverted gap is small compared with other energy scales. Under the assumption, the nodal structures form near the point of band inversion, and we propose that the parity and rotation eigenvalues of the inverted bands determine many aspects of the resultant nodal loops: their types, positions and monopole charges [92].

4.2 Adiabatic Hamiltonian reduction for four-band systems

In this section, we show that the Hamiltonian of an arbitrary four-band system can be adiabatically deformed into one of the two special cases without introducing new band crossings between the two valance and two conduction bands. The existence of

this adiabatic path allow us to reduce any Hamiltonian into (one of) these two special cases, where topological analysis is greatly simplified and topological indices mostly are fully dictated by band inversions at high symmetry points.

4.2.1 Γ matrices and the basis for 4-band Hamiltonians

In general, a 4×4 Hermitian matrices spans a 16-dimensional linear space, and the following 16 matrices can be used as the basis of this linear space: (1) the identity matrix I, (2) four Γ-matrices Γ_i with $i = 1$, 2, 3, and 4, (3) six Σ-matrices $\Sigma_{i,j} = i[\Gamma_i, \Gamma_j]/2$ and (4) four matrices $i\Gamma_j\Gamma_k\Gamma_l$ where $i = \sqrt{-1}$ and $j \neq k \neq l$ and (5) $\Gamma_5 = \Gamma_1\Gamma_2\Gamma_3\Gamma_4$. An example of these matrices can be found in Appendix C.1. These 16 matrices all come from the four Γ matrices and their products. The Γ matrices satisfy the Clifford algebra of a four-dimensional Euclidean space $\{\Gamma_a, \Gamma_b\} = 2\delta_{ab}$ and the Σ matrices satisfy the so(4) Lee algebra and form a representation for the generators of the SO(4) rotational group.

For systems with time-reversal and space-inversion symmetry ($T^2 = +1$), the Hamiltonian can be made real when proper basis are utilized. For a 4×4 real-symmetric matrix, one can use the following 10 matrices as its basis (1) the identity matrix I, (2) Γ_1, Γ_2, Γ_3, (3) Σ_{14}, Σ_{24} and Σ_{34}, (4) $i\Gamma_1\Gamma_2\Gamma_4$, $i\Gamma_2\Gamma_3\Gamma_4$, $i\Gamma_1\Gamma_3\Gamma_4$. With this basis, any Hamiltonian of a four-band system with time-reversal and space-inversion symmetry can be written as the linear combination of these 10 matrices

$$H = a\Gamma_1 + b_1\Gamma_2 + b_2\Gamma_3 + c_1\Sigma_{14} + c_2 i\Gamma_2\Gamma_3\Gamma_4 + \ldots \tag{4.4}$$

In this basis, the product of the time-reversal and space-inversion symmetry is simply $TI = K$, where K implies complex conjugate. For reasons that will be discussed below, here we choose to showed the explicit form for 5 of the 10 terms. The coefficients here (a, b_1, b_2, c_1, c_2 and 5 additional terms that we didn't explicitly show here) are

real functions of momentum $\boldsymbol{k}$. In general, this is a complicated Hamiltonian, which requires 10 independent functions of $\boldsymbol{k}$ to characterize. Although the eigenvalues and eigenfunctions of this Hamiltonian could be computed in principle, they involve solutions of a quartic eigen-equation, whose analytic formula is extremely complicated in general.

As shown in the Appendix C.2, for an arbitrary four-band Hamiltonian with time-reversal and space-inversion symmetry, we can adiabatically deform the Hamiltonian into one of the following two structures

$$H_1 = a\Gamma_1 + b_1\Gamma_2 + b_2\Gamma_3, \tag{4.5}$$

and

$$H_2 = a\Gamma_1 + c_1\Sigma_{14} + c_2 i\Gamma_2\Gamma_3\Gamma_4. \tag{4.6}$$

This adiabatic procedure will not induce any new level crossing between the two conduction and two valence bands. As a result, the topological structure and topological indices (e.g. the monopole charge of nodal lines [87]) remain invariant. The existence of such an adiabatic deformation provides us an easy pathway to classify possible topological states here. Instead of trying to classify all arbitrary Hamiltonians as shown in Eq. (4.4), we reduce the problem into classifying the topological structures for the two reduced Hamiltonians H_1 and H_2 [Eqs. (4.5) and (4.6)].

In addition, it is worthwhile to point out that the reduced Hamiltonian H_1 and H_2 greatly simplifies the topological index calculation because of two reasons. First, in constrast to a generic Hamiltonian, these two reduced Hamiltonians can be easily diagonalized and the eigen-wavefunctions take a simple analytic form, making topological information easy to access. Secondly, these two Hamiltonians have an extra Z_2 symmetry, and as will be shown below, this Z_2 symmetry provides a direct connection

between topological indices and high-symmetry-point band inversions, which greatly simplifies the topological index calculation.

As one can easily check, H_1 and H_2 share a lot of identical properties. For both of them, the two conduction (valence) bands are degenerate, and the eigen-energy share the same functional form.

$$\epsilon_1 = \pm\sqrt{a^2 + b_1^2 + b_2^2} \tag{4.7}$$

for H_1 and

$$\epsilon_2 = \pm\sqrt{a^2 + c_1^2 + c_2^2} \tag{4.8}$$

for H_2. These similarities between H_1 and H_2 are not accidental. Instead, it is the direct consequence of a duality relation, which will be discussed in the following section.

4.2.2 Duality relation

There is a duality relation between H_1 and H_2, which implies that these two Hamiltonians must share identical algebraic properties.

As mentioned above, the Γ matrices form a representation of the Clifford algebra. On the other hand, the exact form of Γ matrices is not unique. For example, we can choose to use another set of Γ matrices:

$$\tilde{\Gamma}_1 = \Gamma_1 \tag{4.9}$$

$$\tilde{\Gamma}_2 = \Sigma_{14} \tag{4.10}$$

$$\tilde{\Gamma}_3 = i\Gamma_2\Gamma_3\Gamma_4 \tag{4.11}$$

$$\tilde{\Gamma}_4 = -\Sigma_{12} \tag{4.12}$$

This new set of $\tilde{\Gamma}$ matrices also follow the same Clifford algebra, and thus are fully equivalent to the original ones that we used above from the algebraic point of the view.

In other words, the Γ matrices and the $\tilde{\Gamma}$ matrices provide two representations of the Clifford algebra, mathematically equivalent to each other. More interestingly, these two representations are the dual of each other $\tilde{\tilde{\Gamma}}_i = \Gamma_i$, i.e. the same transformation from Γ to $\tilde{\Gamma}$ [Eqs. (4.9)-(4.12)] also maps $\tilde{\Gamma}$ back to Γ. To observe this duality relation, we first use these new $\tilde{\Gamma}$ matrices and their products to define another set of 16 matrices as the basis for 4×4 Hermitian matrices, and it is easy to verify that this new set of matrices satisfies the dual relation of Eqs. (4.9)-(4.12).

$$\Gamma_1 = \tilde{\Gamma}_1 \tag{4.13}$$

$$\Gamma_2 = \tilde{\Sigma}_{14} \tag{4.14}$$

$$\Gamma_3 = i\tilde{\Gamma}_2\tilde{\Gamma}_3\tilde{\Gamma}_4 \tag{4.15}$$

$$\Gamma_4 = -\tilde{\Sigma}_{12} \tag{4.16}$$

and thus $\tilde{\tilde{\Gamma}}_i = \Gamma_i$. Furthermore, this duality relation also applies to H_1 and H_2, i.e. H_1 and H_2 swaps as we swap Γ_i with $\tilde{\Gamma}_i$.

$$H_1 = a\Gamma_1 + b_1\Gamma_2 + b_2\Gamma_3 = a\tilde{\Gamma}_1 + b_1\tilde{\Sigma}_{14} + b_2 i\tilde{\Gamma}_2\tilde{\Gamma}_3\tilde{\Gamma}_4, \tag{4.17}$$

and

$$H_2 = a\tilde{\Gamma}_1 + c_1\tilde{\Gamma}_2 + c_2\tilde{\Gamma}_3 = a\Gamma_1 + c_1\Sigma_{14} + c_2 i\Gamma_2\Gamma_3\Gamma_4, \tag{4.18}$$

In summary, the duality relation can be represented as

$$\Gamma_1 \Leftrightarrow \Gamma_1 \tag{4.19}$$

$$\Gamma_2 \Leftrightarrow \Sigma_{14} \tag{4.20}$$

$$\Gamma_3 \Leftrightarrow i\Gamma_2\Gamma_3\Gamma_4 \tag{4.21}$$

$$\Gamma_4 \Leftrightarrow -\Sigma_{12} \tag{4.22}$$

$$H_1 \Leftrightarrow H_2 \tag{4.23}$$

$$P_1 \Leftrightarrow P_2 \tag{4.24}$$

where P_1 (P_2) is a Z_2 operator that will be defined in the next section. Because Γ and $\tilde{\Gamma}$ matrices satisfy the same algebra, this duality relation implies that H_1 and H_2 must have the same algebraic properties.

4.2.3 Z_2 symmetry and the parity Chern number

H_1 and H_2 also share another important common feature. Both these two Hamiltonians preserve a Z_2 symmetry. We can define two Z_2 parity operators

$$P_1 = i\Gamma_1\Gamma_2\Gamma_3 \tag{4.25}$$

and

$$P_2 = i\tilde{\Gamma}_1\tilde{\Gamma}_2\tilde{\Gamma}_3 \tag{4.26}$$

It is easy to verify that

$$P_1^2 = P_2^2 = 1 \tag{4.27}$$

and

$$[H_1, P_1] = [H_2, P_2] = 0 \tag{4.28}$$

Thus, H_1 (H_2) preserves the Z_2 symmetry defined by P_1 (P_2). Notice that P_1 and P_2 are also dual to each other.

In addition, it must be emphasized that these parity operates anti-commute with TI.

$$\{P_1, TI\} = \{P_2, TI\} = 0 \tag{4.29}$$

This anti-commutation relation implies two things. First of all, it requires that for H_1 or H_2, the two valence (conduction) bands must be degenerate. This is because no $1D$ representation can give such an anti-commutation relation, and thus 2-fold degeneracy has to be required, in analogy to Kramers doublets from the $T^2 = -1$ time-reversal symmetry. Secondly, due to the same anti-commutation relation, the two degenerate quantum states here (in either the valence or the conduction bands) must have opposite parity. Here, the parity refers to the +1/-1 eigenvalue of P_1 or P_2.

This degeneracy/parity property is very important because it allows us to define a topological index, which will be called the parity Chern number. Among the two degenerate valence bands, the parity of this Z_2 symmetry allows us to select one band with +1 (or -1) parity eigenvalue. For any 2D closed manifold in the 3D k-space (e.g. the $k_z = 0$ plane), we can then compute the Chern number of this band that we selected: C^+ for the band with parity +1 and C^- for the other band with parity -1. This parity Chern number is an integer topological index, in analogy to the spin Chern number or mirror Chern number in quantum spin Hall systems or systems with mirror symmetry. The time-reversal and space-inversion symmetries here imply that

the total Chern number must vanish, and thus $C^+ = -C^-$.

For H_1 and H_2, this parity Chern number has a clear and specific physical meaning. If this topological index is nonzero for any closed and contractible k-space 2D manifold, then it implies that this manifold has a nontrivial topological structure and thus cannot be adiabatically shrink into a point. In other words, some gapless nodal points shall arise in the 3D space enclosed by this manifold, which prevent this manifold from adiabatically shrinking into a point. Generically, these nodal points are Dirac points with four-fold degeneracy (i.e. the two conduction and two valence band all becomes degenerate at this Dirac point), and each Dirac point carries a parity Chern number ± 1. Thus, the parity Chern number of a 2D manifold here measures directly the number of Dirac points enclosed by this manifold. As will be shown below, when certain rotational symmetry is enforced, more complicated band crossing points, e.g. quadratic or cubic band crossing points in analogy to their 2D counterparts [96], can also emerge. In general, one quadratic (cubic) band crossing point carries a parity Chern number ± 2 (± 3).

As we deviate away from H_1 and H_2 (but preserve the time-reversal and space-inversion symmetry), the Z_2 symmetry defined by P_1 or P_2 is explicitly broken, but these Dirac points cannot be gapped out. Instead, they develop into topological nodal lines. In particular, these topological nodal lines are not conventional ones. Instead, each of them carries a nontrivial monopole charge. This is because C^+ mod 2 coincides with another topological index, the Z_2 monopole charge introduced in Ref.[87]. As we deviate the Hamiltonian from H_1 and H_2, the Z_2 symmetry will in general be explicitly broken and thus the parity Chern number is no long well defined, but the parity of the parity Chern number (i.e. the monopole charge) remains as a good topological index. For any adiabatic deformation of the Hamiltonian, this index remains invariant and thus a Dirac point for H_1 and H_2 with $C^+ = \pm 1$ shall evolve into a topological nodal line with monopole charge 1.

In general, as shown in Ref.[87], a monopole charge is a Z_2 index with value being either 0 or 1. However, as will be shown below, if additional symmetry is enforced, monopole charge may take higher values beyond 1. The physical meaning of a higher monopole charge is two fold. (1) In certain cases, it is associated with the number of topological nodal lines. As we mentioned early on, for H_1 and H_2, the value of parity Chern number provides the number of Dirac points. In the presence of certain rotational symmetry, we may have multiple Dirac points (associated with each other via some symmetry transformation), and thus a large-than-one parity Chern number. As we deviate from H_1 or H_2, each of the Dirac points will develops into a topological nodal line, and thus the parity Chern number provides us direct information about the number of topological nodal lines that we should expect in the Brillouin zone. (2) In certain other cases, as will be shown below, a higher index doesn't produce multiple nodal lines. Instead, we found one single topological nodal line carrying high topological index (monopole charge 2) in systems with four-fold or six-fold rotational symmetries. These nodal lines must be around a high symmetry axis and preserve the corresponding rotational symmetry, and their high index can be justified by defining a Z_2 monopole charge in a fraction of a closed 2D manifold embedded in the 3D Brillouin zone.

Another key property of these parity Chern number lies in the fact that it can be directly associated with band inversions at high symmetry points, through a technique derived in Ref.[27]. Thus, our topological index offers a bridge way to connect band inversions at high symmetry points with the topological nature of nodal lines. With this bridge, in most cases, information about high symmetry points can fully dictate topological nodal lines, especially those with nontrivial monopole charge. This result is one key observation of this manuscript, and it allows us to classify and locate topological nodal lines (with nontrivial monopole charge) purely based on local information of the band structure.

4.2.4 Theoretical approach

Below, we will utilize the techniques discussed above to analyze and classify topological nodal lines in 3D systems with time-reversal and space-inversion symmetries. We will consider systems with different rotational symmetries and various types of band inversions. As mentioned above, here, we first focus on four-band models with two conduction/valence bands, but the topological indices discussed here is well defined in generic systems with arbitrary number of bands and thus all the topological properties remain invariant, when extra bands are introduced. In addition, for simplicity, we will focus on the case where band inversions only occur at the Γ point ($\boldsymbol{k} = 0$), but the same discussion and principle can be generalized to deal with band inversions at other high symmetry points.

We will classify the band inversion based on symmetry and the point group representation of each band. For each allowed band inversion type, we will compute the parity Chern number (defined above) for H_1 and H_2 over the $k_z = 0$ plane and the $k_z = \pi$ planes. Because we have shown above that any four-band Hamiltonian can be adiabatically deformed into either H_1 and H_2, although we only examine H_1 and H_2 in this effort, our conclusions generically apply to any generic Hamiltonians. With this parity Chern numbers, we can then define a topological index

$$Q = C^{+}_{k_z=\pi} - C^{+}_{k_z=0} \tag{4.30}$$

This index measures the difference between the parity Chern number in the $k_z = 0$ and $k_z = \pi$ planes. For H_1 and H_2, this index will be labeled as Q_1 and Q_2 respectively.

As mentioned in the previous section, for the Hamiltonian H_1 or H_2, this index Q measures the number of Dirac points located between the $k_z = 0$ and $k_z = \pi$ planes, i.e. the upper half of the 3D Brillouin zone ($0 < k_z < \pi$). It is easy to verify that the lower half of the Brillouin zone ($-\pi < k_z < 0$) has the same number of Dirac points

due to the space-inversion symmetry. For a generic Hamiltonian (away from H_1 or H_2), each Dirac points will evolve into a topological nodal line (with a nontrivial monopole charge), and thus this index Q measures the number of topological nodal loops (with nontrivial monopole charge) in the upper half of the Brillouin zone. This is how we determine the topological structure and classify topological states in these systems. In particular, for the simplest case (without any other symmetries), Q mod 2 is just the monopole charge of the upper half Brillouin zone.

To compute this topological index Q, we apply the method developed in Ref.[27] for the $k_z = 0$ and $k_z = \pi$ planes respectively. This technique allows us to determine Q purely using information about high-symmetry-point band inversions, up to modular $2n$ for a system with $2n$-fold rotational symmetry or $4n+2$ for system with $(2n+1)$-fold rotational symmetry. These values are fully dictated by what happened at high symmetry points, while microscopic details away from high symmetry points become irrelevant.

As will be shown below, in certain cases, the $k_z = 0$ or $k_z = \pi$ planes are not fully gapped, e.g. mirror symmetry-protected nodal lines may arise if $k_z = 0$ or π is a mirror plane. For these cases, we will choose a 2D plane in the Brillouin zone slightly deformed from $k_z = 0$ or π, as demonstrated in Fig.(4.3). This deformed plane respects the same rotation symmetry (for rotations along the z axis), and it contains all the four high symmetry points of the $k_z = 0$ or π plane, i.e. k_x and k_y being 0 or π. This deformed k-space 2D plane will avoid the gapless points or nodal lines, such that we can define and compute the parity Chern number mentioned above. Because we preserved the high symmetry points and the rotational symmetry, the parity Chern number can still be dictated by high-symmetry-point band inversions same as before.

We should also emphasize that here we only focus on generic topological properties that are robust against fine tuning or perturbations, as long as the symmetry and the gap remain. Thus, in general, it is possible that additional nodal lines or nodal points

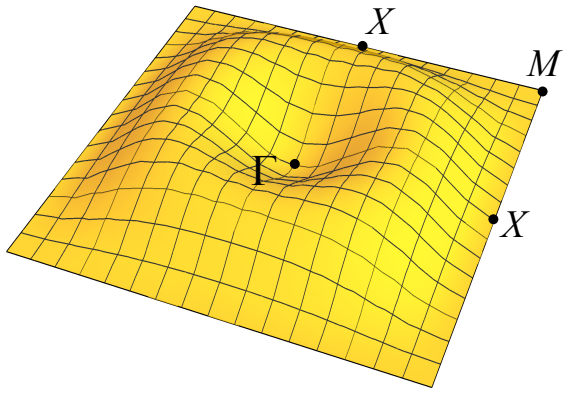

Figure 4.3: A deformed $k_z = 0$ plane for the calculation of topological indices. If the $k_z = 0$ plane is not fully gapped, we can choose a slightly deformed plane to calculate the topological index. Here we demonstrate one example by considering a system with four-fold rotational symmetry around the z axis. With inversion symmetry and four-fold rotational along z, the $k_z = 0$ plane is a mirror plane ($k_z \to -k_z$), and thus it may contain mirror-symmetry-protected topological nodal lines. To find a fully gapped 2D manifold in the k-space to define the topological index (e.g. C^+ or the monopole charge), we can deform a bit from the $k_z = 0$ plane as shown in the figure. The deformed 2D manifold still contains all the four high symmetry points of the original $k_z = 0$ plane (Γ, X and M), and it still preserves the four-fold rotational symmetry along z. This 2D manifold allows us to avoid nodal lines or nodal points in the $k_z = 0$ plane and thus topological indices can be defined and computed using high symmetry points.

may arise, e.g. accidental degeneracy, but those features in general can be gapped out via adiabatic perturbations and would not be considered in our study.

4.2.5 Comparison with lattice models

In addition to theoretically analyzing topological indices using reduced Hamiltonian H_1 and H_2, in Appendix C.4 we also constructed lattice models with generic Hamiltonians beyond H_1 and H_2. These lattice models are constructed based on symmetry without further constraints. For each specific lattice, we introduce orbits with different symmetry to each Bravais lattice site, and systematically included all symmetry-allowed short-range hopping terms in our model Hamiltonian Details about the symmetry-based construction can be found in Ref.[97]. In these lattice models, we randomly assign values to the control parameters (e.g., the hopping strength) and compute the band structure by numerical diagonalizing the Hamiltonian in the k-space. Then we compared nodal lines and other topological features that are observed in these models with our generic theoretical classifications (using H_1 and H_2). The generic classification and model calculations agree with each other in all the cases that we have examined.

4.3 Band inversions in the presence of time-reversal symmetry

In this section, we demonstrate the generic techniques discussed above by focusing on systems with one pair of bands inverted at the Γ point, and no band inversion takes place at any other high symmetry points. We will first provide a summary of result, while details are being provided afterwards.

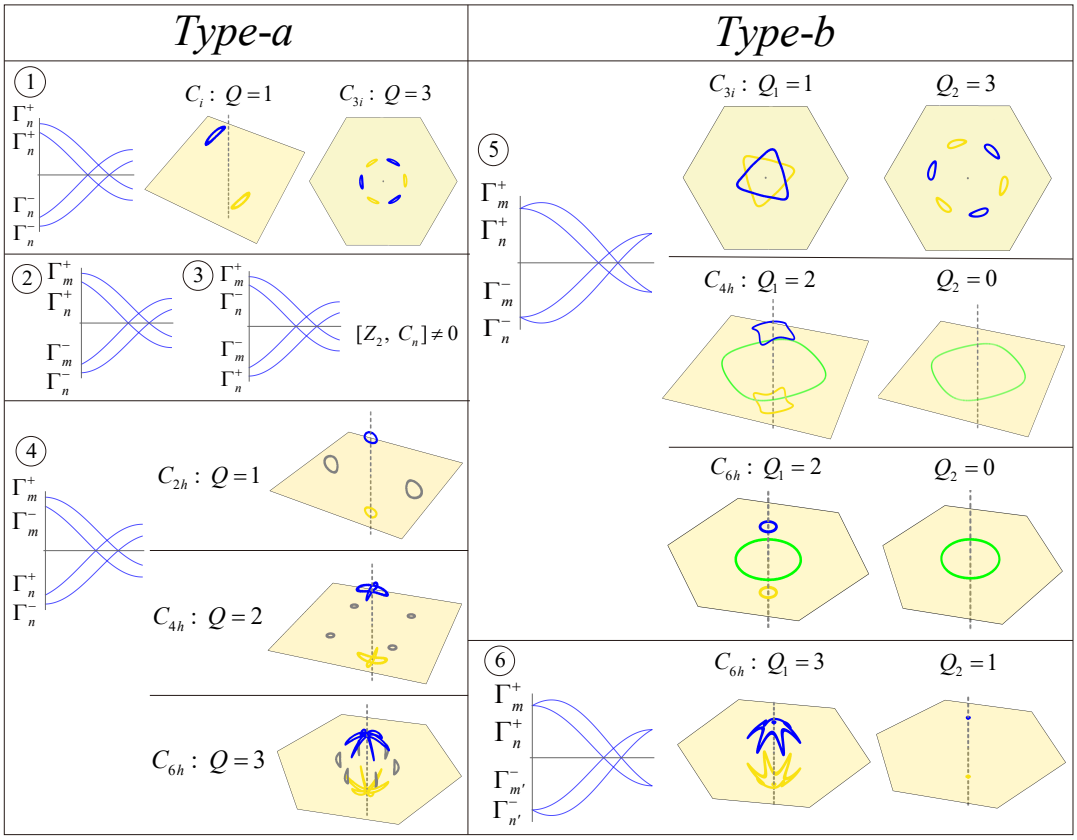

Figure 4.4: Band inversions and topological nodal lines in systems with various symmetries. Blue (yellow) nodal lines represent nodal lines in the upper (lower) half of the Brillouin zone with $0 < k_z < \pi$ ($-\pi < k_z < 0$). All these nodal lines carry nontrivial monopole charge and thus they cannot be gapped out by shrinking into a point. Green nodal lines are protected by the mirror symmetry and is located in the $k_z = 0$ plane. Gray nodal lines cannot be detached from the $k_z = 0$ mirror plane, but they are not mirror-symmetry-protected nodal lines. Instead, these gray nodal lines also carry nontrivial monopole charge and thus cannot be gapped out by shrinking into a point.

4.3.1 Summary of results

As mentioned early on, we consider systems with time-reversal and space-inversion symmetry, and ignore spin-orbital effects ($T^2 = +1$). In addition, we assume that the system preserves the n-fold rotational symmetry along the z axis with $n = 1, 2, 3, 4, 6$. We focus on systems with a double band inversion at the Γ point, which can be classified and labeled according to the symmetry representations of the bands as summarized in the table shown in Fig.(4.4). Here we distinguish two different scenarios depending on whether the inverted bands at Γ belongs to type-a or type-b representations, and 6 different families of band inversions are examined here as shown in the table. Here, we follow the same notation utilized in the study of point or space groups [98], where type-a and type-b represent two different types of response under time-reversal (See below for their definitions and other details).

For band inversions between type-a bands, it turns out that high-symmetry-point band inversions fully dictate the topological index and the configuration of the topological nodal lines, while for type-b bands, for each specific band inversion, two quantum phases with distinct topological structure and nodal line configurations are always allowed. These two phases are separated by a topological transition, signatured by a gap closing in (or near) the $k_z = 0$ plane.

In particular, we would like to highlight band inversion family 4, 5 and 6 shown in Fig.(4.4). For family 4, we found a special type of nodal lines (blue and yellow lines) which are oriented along a high symmetry axis. Each of these nodal lines carries a monopole charge of 1. Remarkably, for systems with a four-fold or six-fold rotational symmetry, these nodal lines have to tangle together to form a cage like structure, due to a combined constraint from topology and symmetry. Because these nodal lines are connected, the monopole charge of each line becomes ill defined. Instead, the correct topological index here is the monopole charge of a cage structure, which carries a monopole charge 2 and 3, if the rotational symmetry is four- and six-fold

respectively. In addition, this family may also show nodal lines near the $k_z = 0$ plane (gray lines). These nodal lines may orient parallel or perpendicular to the $k_z = 0$ plane and they cannot be detached from the $k_z = 0$ plane due to the mirror symmetry ($k_z \to -k_z$). Although pinned by the mirror symmetry, these nodal lines are not the conventional mirror-symmetry protected nodal lines. Instead, each of them carries a nontrivial monopole charge 1.

In family 5 and 6, for systems with a four- or six-fold rotational symmetry, we observe another new type of nodal lines (blue and yellow). Each of these nodal lines carries a monopole charge 2, in direct contrast to nodal lines without rotational symmetry, whose the monopole charge is a Z_2 index and thus can only be 0 or 1. These monopole-charge-2 nodal lines must be oriented around a high symmetry axis (the k_z-axis). As will be shown below, the rotational symmetry enables us to define the monopole charge on half of a 2D closed manifold in these cases, and the rotational symmetry requires both of the half manifolds share the same monopole charge. As a result, for each half manifold, the monopole charge is still a Z_2 topological index (0 or 1), but for the whole manifold, the monopole charge shall take the value 0 or 2 after adding up the contribution from both half pieces. For a monopole charge 1 nodal line, we know that it can be adiabatically shrunk in to a Dirac point with linear dispersion. For these monopole charge 2 nodal lines, they will shrink into quadratic (or even cubic) band crossing points with quadratic dispersion in directions perpendicular to the rotational axis and linear along k_z.

4.3.2 Three types of time-reversal symmetry in lattice systems

For a homogenous system with SO(3) rotational symmetry, time-reversal symmetry can be classified into two categories, depending on whether we have integer or half-integer spins. In a lattice systems, however, this classification becomes more complicated due to the interplay between space and time symmetry. Instead of two

categories, three categories becomes needed, dubbed type-a, b and c [98].

A type-a representation of a point group is also known as a real representation. Under time-reversal, a type-a representation is mapped back to itself. Type-b representations are also known as complex representations. Under time-reversal, a type-b representation will turn into another representation, different from the original one. For example, in a system with three-fold rotational symmetry (point group C_3), this group has three presentations doubled Γ_1, Γ_2 and Γ_3. Under a C_3 rotation, states belongs to the Γ_1 representation remains unchanged, while states in Γ_2 or Γ_3 representation pick up a complex phase $e^{2\pi/3i}$ or $e^{-2\pi/3i}$ respectively. Here, Γ_1 is a type-a representation, who is its own time-reversal partner, while Γ_2 and Γ_3 are type-b representations and they are the time-reversal partner of each other. This can be easily checked by realizing that due to its anti-Hermitian nature, time-reversal flips the complex phase factors $e^{2\pi/3i}$ and $e^{-2\pi/3i}$, which is why Γ_2 and Γ_3 are connected by a time-reversal transformation. Type-c representations are similar to type-a in the sense that the representation is its own time-reversal partner. However, in contrast to type-a, type-c representations cannot be made real due to the half-integer spin quantum number. In this paper, we will only consider type-a and type-b representations, because type-c representations are prohibited in systems without spin-orbit couplings ($T^2 = +1$) [98].

In comparison to a homogeneous system with SO(3) rotational symmetry, type-a and type-c corresponds to integer and half-integer spins respectively. In contrast, type-b is the most special one among the three, and it has no correspondence in the SO(3) rotational group. Remarkably, we found that band inversions between between type-a bands and band inversions between type-b bands result in totally different topological structures and topological classifications, which is one of the key results of this manuscript as summarized in the Table in Fig.(4.4).

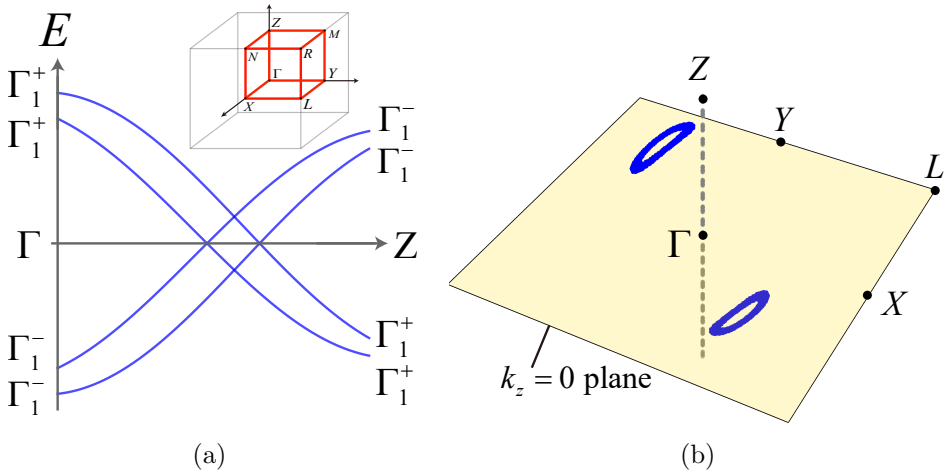

Figure 4.5: (a) Schematic band structure demonstrating a pair of band inversion at Γ. The inset shows the Brillouin zone of a system with C_i symmetry. Here, the eight high symmetry points are labeled as Γ, X, Y, L, Z, M, N, R following the convention of a triclinic Bravais lattice. At Γ, the two valence (conduction) bands have the $-$ $(+)$ parity under space-inversion, which is opposite to all other high symmetry points where the valence (conduction) bands have the $+$ $(-)$ parity. (b) Topological nodal lines induced by this band inversion.

4.3.3 Point group C_i

If the system has no other symmetry beyond space-inversion and time-reversal, the crystal point group is C_i. In this case the system does not have any rotational symmetries. Without spin-orbit coupling, the group C_i has two representations, Γ_1^+ and Γ_1^- (even or odd under space-inversion respectively), and both these two representations are type-a. For this case, all the eight high symmetry points share the same point-group symmetry. With the assumptions presented above, only one type of band inversion is possible here as shown in Fig.(4.5). At the Γ point, the two valence bands belong to the Γ_1^- representation and the two conduction bands have the symmetry of Γ_1^+, while all other high symmetry points are opposite with the valence (conduction) bands belonging to the Γ_1^+ (Γ_1^-) representation.

Here, we can look at the $k_z = 0$ plane. For H_1, we use the Z_2 symmetry P_1 to define a parity Chern number. Because for the 2D $k_z = 0$ plane, space-inversion

is effectively equivalent to a π rotation along the z-axis, this $k_z = 0$ plane can be considered as a 2D system with 2-fold rotational symmetry along z. As shown in Ref.[27], with 2-fold rotational symmetry, we can compute a Chern number up to mod 2 using high symmetry points rotational eigenvalues (i.e. $+1/-1$ parity of the valance bands for our system here). Here, because the rotational operator commute with the Z_2 symmetry, we can apply the same technique for the parity Chern number and find that $C^+_{k_z=0} \mod 2 = 1$. The same analysis for the $k_z = \pi$ plane produces $C^+_{k_z=\pi} \mod 2 = 0$. Thus, $Q_1 \mod 2 = 1$, where Q is the topological index defined above in Eq. (4.30) and the subindex 1 here implies that it is for H_1. For H_2, we can perform the same analysis and we find that $Q_1 = Q_2 = 1$ up to mod 2.

Because any Hamiltonian is adiabatically connected with either H_1 or H_2, the fact $Q_1 = Q_2 = 1$ implies that this band inversion always produces the same topological structure, with Z_2 monopole charge 1. For H_1 and H_2, as mentioned above, the topological index implies that one Dirac point is located in the upper half of the Brillouin zone ($0 < k_z < \pi$), and one in the lower half ($-\pi < k_z < 0$). For a generic Hamiltonian deviated from H_1 or H_2, each Dirac point evolves into a topological nodal line with a nontrivial Z_2 monopole charge, and thus we expected one nodal line located in the upper half of the Brillouin zone and one in the lower half. Both these two nodal lines carry nontrivial monopole charge, and thus they cannot be gapped out by shrinking a nodal loop into a point [87].

As shown in Fig.(4.5), we setup a four-band lattice model on a triclinic lattice with four orbits (two with + and two with − parity under space-inversion) at each Bravais lattice site. With this band inversion, the band structure indeed shows nodal lines and monopole charge as predicted above. Details about the model can be found in the Appendix C.4.

It is worthwhile to mention that the index Q here is determined up to mod 2, and thus for H_1 and H_2 the number of Dirac points is determined only up to mod 2.

In principle, extra pairs of Dirac points may arises in the upper half of the Brillouin zone (and the same number of pairs of Dirac points will arise in the lower half as well due to the inversion symmetry). These extra pairs are allowed but not generic or universal, because in general, a pair of Dirac points can annihilate with each other and be gapped out via adiabatic deformations. Thus, because we have confined our focus on generic and universal properties as stated in earlier sections, these extra pairs of nodal lines will not be consider, neither will we try to obtain the value of Q beyond mod 2 in this symmetry class.

4.3.4 Systems with n-fold rotational symmetries

If the system preserves a n-fold rotational symmetry along z ($n > 1$), in addition to space-inversion and time-reversal symmetries, more complicated band inversions become allowed. Here, again we focus on cases with one pair of bands inverted at the Γ point. And as highlighted in the Introduction, we consider small inversion at Γ, where the inverted gap is small compared with other energy scales in the system. The results is shown in Fig.(4.4), where we showed a table summarizing 6 families of possible band inversions. It is worthwhile to emphasize that here we didn't try to exhaust all possible types of band inversions, but the same technique can be easily generalized.

One remarkable observation here lies in the fact that if the inverted bands have type-a time-reversal symmetry, the band inversion fully dictates the value of the topological index. However, if the inverted bands all have type-b time-reversal symmetry, then the topological indices may take two different values, i.e. the band inversion doesn't fully dictate the topological index. In these systems, as we tune the values of control parameters, a topological phase transition will be triggered, at which some of the nodal lines annihilate and reconfigure with each other.

Same as before, the band inversion is characterized by the symmetry properties

of the inverted bands, and labeled by the symmetry representations of each band at high symmetry points. Here, we follow the group theory notation used in Ref.[98]. In general, for systems with the space-inversion symmetry, a representation of a point group is labeled as Γ with two indices $\Gamma_n^{\pm}$. The subindex n is the an integer. Representations with different subindex n show different response to space rotations and mirror reflections, etc. The superscript $+$ or $-$ labels the parity under space-inversion (± 1).

4.3.5 Band inversion between type-a bands

In this section, we examine band inversion between bands with type-a time reversal symmetry.

Here, we start from family 1, where we have four orbits per unit cell, and their symmetry representations all share the same subindex Γ_n but two of them have $+$ parity under space-inversion, while the other two are $-$. Because these four bands have two distinct parity eigenvalues, we can distinguish them and thus define a pair of band inversion at Γ. As shown in the schematic band structure in Fig.(4.4), for family 1, we assume that at the Γ point, the two bands with $-$ parity has lower energy, while at all other high symmetry points, it is the two $+$ parity bands who have lower energy. It is worthwhile to mention that in general, Γ point preserves the same point group symmetry as the crystal itself, and thus, the bands can be labeled using the representation of the point group of the crystal. However, for other high symmetry points, their point group (known as the little group at that momentum point) is usually a subgroup of the point group of the crystal. As a results, we should use the representation of the corresponding subgroup to label the bands at those momentum points. For a small band inversion considered here, the representation for bands away from the Γ point can be deduced easily from the point-group compatibility table [98]. We will not dive into the mathematical details here, but nevertheless, for

any band inversion, the point group allows us to immediately determine the symmetry representations at any high symmetry points. And thus, we can use the formula developed in Ref.[27] to compute the topological index. For band inversions in family 1, it turns out that the index is always trivial, if the system has even-fold rotational symmetry along z (C_{2n}). For odd-fold (C_{2n+1}), the index is $Q = 2n + 1$ regardless of microscopic details. This result implies that with even-fold rotational symmetry, this band inversion will not leads to any nodal lines with nontrivial monopole charge. Instead, it is quite straightforward to note that because even-fold rotation and space-inversion imply that the $k_z = 0$ plane is a mirror plane, this band inversion will result in a mirror-symmetry-protected nodal line in the $k_z = 0$ plane. For systems with odd-fold rotational symmetry (C_{2n+1}), $k_z = 0$ is not a mirror plane and thus no mirror-symmetry-protected nodal line will emerge, but the nontrivial index Q implies that we shall see $2n + 1$ nodal lines in the upper half of the Brillouin zone ($0 < k_z < +\pi$), each of which carries a nontrivial monopole charge 1, and they are related to each other by the C_{2n+1} rotation along z. The inversion symmetry implies that another set of $2n+1$ nodal lines shall arise in the lower half of the Brillouin zone $-\pi < k_z < 0$.

In family 2 and 3, the bands involved in the band inversion has different rotational symmetry (i.e. their representations have different subindex label $n \neq m$). In this case, high symmetry point doesn't provide direct information about the topological index. This is because for this case, the Z_2 symmetry (P_1 or P_2) dosen't commute with the rotational symmetry (C_n). As a result, we cannot apply the method in Ref.[27] to determine the parity Chern number using high-symmetry-point rotational eigenvalues.

In family 4, we consider a different type of band inversion with $n \neq m$. It turns out that this case only arises for systems with even-fold rotational symmetry (2, 4 or 6), where systems with C_{3i} symmetry (three-fold) don't have two different a-type

representations and thus we cannot get $n \neq m$. The topological index Q for this case is n, if the system preserves $2n$-fold rotation symmetry along z. As mentioned above, generically, $Q = n$ implies that for H_1 or H_2, we will have n Dirac points in the upper (or lower) half of the Brillouin zone. For a generic Hamiltonian (deviated from H_1 or H_2), each Dirac point evolves into a topological nodal line, and thus n nodal lines should be expected for the upper (or lower) half of the Brillouin zone.

As will be shown below, this naive picture is indeed correct, but the $2n$-fold rotational symmetry here gives us an interesting twist. In fact, the topological index $Q = n$ and the $2n$-fold rotational symmetry together tells us that each topological nodal line here must preserve the C_2 symmetry (two-fold rotational along z), and thus these nodal lines must organize themself into a cage-like structure as shown in Fig.(4.4).

For H_1 and H_2, if a system has a $2n$-fold rotational symmetry and we have a Dirac point at momentum $\boldsymbol{k}$, Dirac points shall also be found at momentum $C_{2n}\boldsymbol{k}$, $C_{2n}^2\boldsymbol{k}$ ... $C_{2n}^{2n-1}\boldsymbol{k}$ due to the rotational symmetry. Unless $\boldsymbol{k}$ is on certain high symmetry lines (e.g. the k_z axis with $k_x = k_y = 0$), these $2n$ momentum points are in general different from each other and thus $2n$ Dirac points shall be expected in the upper half of the Brillouin zone. However, the topological index dictates that only n Dirac points can exists here, which is half of $2n$. This implies immediately that our Dirac points must be located on certain high symmetry lines, such that the following $2n$ momentum points are not all distinct: $\boldsymbol{k}$, $C_{2n}\boldsymbol{k}$, $C_{2n}^2\boldsymbol{k}$ ... $C_{2n}^{2n-1}\boldsymbol{k}$. Similarly, for the nodal loops, due to the same reason, we should generically expect $2n$ of them in the upper half of the Brillouin zone. However, the fact that $Q = n$ implies that we can have only n nodal lines, and thus each of our nodal line must be invariant under two-fold rotational along z (i.e. under such a rotation, a nodal is mapped back to itself). These combined constraints from topology and symmetry require that the nodal lines must form the cage like structure as shown in Fig.(4.4).

This theory prediction is indeed what we observed in lattice models. In this case, without utilizing any topological knowledge, the band inversion and the n-fold rotational symmetry along the z-axis automatically implies that two gapless nodal points must arise along the $k_x = k_y = 0$ axis. This is because the band inversion cannot satisfy the symmetry compatibility relation of the point/space group along the z axis [98]. In other words, along the k_z axis ($k_x = k_y = 0$), bands from representations Γ_m and Γ_n have different symmetry under z-axis rotation, and thus hybridization between them is prohibited. As a result, this band inversion at Γ must lead to symmetry protected band crossings along this high symmetry axis. However, it turns out that this symmetry-based conclusion is not the full story. Instead of two individual nodal points, what really arise here are actually cage-like topological nodal loops as shown in Fig.(4.4). The number of the loops is determined by the rotational symmetry (n loops in the upper half Brillouin zone if we have 2n-fold rotational symmetry). These nodal loops cross with the $k_x = k_y = 0$ axis at two points, which are the two gapless points predicted by the symmetry arguments above. And it is easy to verify that each of the topological nodal line here is invariant under a C_2 rotation along z. As we deform the Hamiltonian towards H_1 or H_2, these cage-like nodal lines all shrink into a point (on the k_z axis). For system with 2-fold rotation, this nodal point is a Dirac point, but if we have 4-fold or 6-fold rotational symmetry, we will find a quadratic or cubic band crossing point instead. Here, for a quadratic or cubic band crossing point, the dispersion is linear along k_z, but in the k_x or k_y direction, the dispersion is quadratic or cubic. These higher-order band crossing point is a 3D version of the 2D quadratic or cubic band crossing point. Similar to their 2D counterparts, a 3D quadratic or cubic band crossing point require rotational symmetries (4 or 6 fold) [96]. Otherwise they will split into 2 or 3 Dirac points. For the topological index, a quadratic (cubic) band crossing point carries parity Chern number 2 (3), which is twice (triple) the value of a Dirac point, which is also the

reason why it develops into 2 or 3 topological nodal lines as we deviate from H_1 or H_2.

In addition, in family 4, some additional topological nodal lines can arise near the $k_z = 0$ plane (gray lines shown in the figure). These nodal lines preserve the mirror symmetry ($k_z \to -k_z$), but they are not the conventional mirror-symmetry-protected nodal lines. As we can see from the figure, these nodal lines can extend out of the ($k_z = 0$) mirror plane, as long as it remains invariant under mirror reflection. Each of these nodal lines carries a nontrivial monopole charge 1.

4.3.6 Band inversion between type-b bands

In family 5 and 6, we consider band inversions from type-b bands, which can occur in systems with 3-, 4- or 6-fold rotational symmetry (i.e. point group C_{3i}, C_{4h}, C_{6h}). At high symmetry points, a band with type-b symmetry must be two-fold degenerate (the band and its time-reversal partner). As a result, a band inversion of type-b bands must invert two bands simultaneously.

For band inversions of type-b bands, it turns out that the nodal line structure in this case is *not* fully dictated by band inversions at high symmetry points. For each specific band inversion, there are always two possible quantum phases with different topological structures. More precisely, we can show that the topological index Q defined above always takes different values for Hamiltonians H_1 and H_2 ($Q_1 \neq Q_2$). Because we have proved above that any Hamiltonian is adiabatically connected to one of these two Hamiltonians (H_1 and H_2), the fact that they have different topological indices implies that for systems with band inversions involving type-b bands, there are always two different quantum phases. Any quantum systems with Hamiltonian adiabatically connected with H_1 belongs to one quantum phase, and all other systems with Hamiltonian smoothly connected with H_2 belongs to the other quantum phase. These two quantum phases are separated by a quantum phase transition, at which

the number of topological nodal lines will change.

In family 5, the valance bands at Γ involves one pair of time-reversal partners with symmetry representation Γ_m^- and Γ_n^- ($T\Gamma_m \to \Gamma_n$ and $T\Gamma_n \to \Gamma_m$). For the conduction bands, the corresponding symmetry representation have the same subindices but the parity (under space-inversion) is opposite Γ_m^+ and Γ_n^+. At all other high symmetry points, these two pairs of states are inverted as shown in the schematic figure. For systems with three-fold rotational symmetry (C_{3i}), in the first phase (adiabatically connected with H_1), the parity Chern number is $Q_1 = 1$ and thus we expect one topological nodal line in the upper half of the Brillouin zone (and one in the lower half) for a generic Hamiltonian in this phase. As we deform the Hamiltonian to H_1, the nodal line shrink into a Dirac point located on the k_z axis. In the second phase, we have $Q_2 = 3$ and thus are three topological nodal lines in the upper (lower) half of the zone. As we deform this Hamiltonian into H_2, these nodal lines merge into three Dirac points, which are not located around the k_z axis, in contrast to H_1. As we try to cross the phase boundary (say from the first phase to the second one), the two nodal lines in the first phase (one above and one below the $k_z = 0$ plane) moves towards each other and eventually they meet at the $k_z = 0$ plane. After the two nodal lines meet, they regroup and split into six new nodal lines (three above and three below $k_z = 0$). The phase transition involves a gap closing in the $k_z = 0$ plane (which was fully gapped in both phases away from the phase boundary), which enables the topological index to change its value, i.e. a topological phase transition.

In systems with four- or six-fold rotational symmetry (point group C_{4h} or C_{6h}), the two quantum phases have $Q_1 = 2$ and $Q_2 = 0$, and thus topological nodal lines with nontrivial monopole charge (blue/yellow shown in the figure) arise in the first quantum phase but not in the second. In both phases, there is a mirror-symmetry protected nodal line (green) in the $k_z = 0$ plane. At the topological phase transition, the two nodal lines with nontrivial monopole charge meet and annihilate at the $k_z = 0$

plane.

It is worthwhile to emphasize that each of the topological nodal lines here carries monopole charge 2, instead of 1. And thus, as this pair of nodal lines annihilate at the topological phase transition, the topological index changes by 2 instead of 1. This is in direct contrast with generic cases where the monopole charge can only be 0 or 1. Due to the four-fold (six-fold) rotational symmetry here, the topological index (monopole charge) is doubled. Instead of 0 and 1, it takes the value 0 or 2. In contrast to a generic nodal line with monopole charge 1, a monopole charge 2 nodal line can only arise in systems with four- or six-fold rotational symmetry. Furthermore, such a charge-2 topological nodal line must be located around a high symmetry axis (with four- or six- fold rotational symmetry), and the nodal line itself is invariant under four- or six- fold rotation, in direct contrast to a conventional charge-1 nodal line. Furthermore, as we deform the Hamiltonian towards H_1, this nodal line shrink into a nodal point. This nodal point is a quadratic band crossing point similar to the one mentioned above in family 4. This quadratic band crossing also indicates that the topological index is 2 here, instead of 1.

In family 6, we consider two pairs of type-b bands with different rotational symmetry (symmetry representation Γ_m^+, Γ_n^+ and $\Gamma_{m'}^-$, $\Gamma_{n'}^-$ with m, n, m', n' being all distinct). This case can only arise in systems with six-fold symmetry (C_{6h}), because other rotational groups don't have two different pairs of type-b representations. In this case there is always a nodal point along the z-axis for $0 < k_z < \pi$ (and another one for $-\pi < k_z < 0$), because all bands have different rotational symmetries along the k_z axis. This nodal point is a Dirac point and it carries monopole charge 1.

Again, we have two topologically-distinct quantum phases with $Q_1 = 3$ and $Q_2 = 1$ respectively. At the topological phase transition, one pair of nodal lines (one above $k_z = 0$ and one below) meet and annihilate at the $k_z = 0$ plane. This nodal line preserves the six-fold rotational symmetry, and it carries monopole charge 2, similar

to the ones we observed in family 5 above. As we deform the Hamiltonian towards H_1, naively, we shall expect this nodal line to shrink into a quadratic band crossing point same as the monopole-charge-2 nodal line in family 5. However, because we have another Dirac point on the k_z axis, this nodal line (with index 2) and the Dirac point (with index 1) will all merge together into one nodal point, which is a cubic band crossing point, consistent with the total topological index $Q_1 = 3$.

4.4 Discussion

4.4.1 Higher symmetries

Above, we considered the space-inversion symmetries and n-fold rotational along z, with $n = 1, 2, 3, 4, 6$, which corresponds to point group symmetries C_i, C_{2h}, C_{3i}, C_{4h}, C_{6h} respectively. For crystals with any of these point group symmetries, we have systematic demonstrated the method to determine topological indices based on high-symmetry-point band inversions and discussed the implication of these topological indices in terms of topological nodal lines and nodal points.

For systems with more complicated point group symmetry, most of our techniques and conclusions can be generalized. This is because as shown above, the index that we used doesn't require any additional symmetry to be defined or calculated, and thus the topological nodal lines presented above do not require additional symmetries to remain stable. Therefore, if we are dealing with a crystal with higher point group symmetries, we can introduce a small perturbation to break the symmetry down to one of the groups that we considered here, and all our conclusions and nodal lines should remains stable as we turn off this small perturbation to recover the full symmetry of the crystal.

On the other hand, it must be emphasized that in systems with a higher symmetry, new phenomena and new topological nodal lines may arise. For example, if the point

group gives us additional mirror planes, extra mirror-symmetry-protected nodal lines may emerge, which is beyond the scope of our study.

4.4.2 Higher monopole charge due to rotational symmetry

As we know, generically, the monopole charge of a topological nodal line can only be 0 or 1, i.e. a Z_2 index. However, as mentioned above, for systems with four-fold or six-fold rotational symmetry, we observed nodal lines carrying higher monopole charge beyond 1. This higher index is due to the rotational symmetry. Here, we use the C_{4h} group in family 4 and 5 to demonstrate this high index, and to prove that our conclusion remains stable when extra bands are introduced (i.e. beyond four-band models). Instead of a four-band system, we consider a system with arbitrary number of bands. First, we will consider a simpler case where all the bands are type-a (like in family 4) or all of them are type-b (like in family 5). Later, we will discuss generic systems with both type-a and type-b bands.

Here, we consider a N-band system composed of type-a orbits only, while the same conclusions hold for systems with only type-b orbits. For a nodal line cage (family 4) or a monopole-charge-2 nodal line (family 5) shown in Fig.(4.4), we can enclose them with a closed-2D manifold. In particular, we can choose the manifold such that it is invariant under two-fold rotation (C_2) along the k_z axis, which can always be achieved because the nodal lines or cages here must preserve this C_2 symmetry. For this closed manifold, we can define the monopole charge, and it has been shown that the monopole charge should be a Z_2 index, if no rotational symmetry is assumed. However, in this case that we consider here, as will be shown below, we can define a Z_2 monopole charge for half of the manifold (say the half with $0 < k_x < \pi$). And due to the two-fold rotational symmetry (C_2), the other half of the manifold must carry the same Z_2 monopole charge. As a result, the total monopole charge of the manifold can be either 0 or 2, depending on whether the half-manifold monopole

charge is 0 or 1. This is the fundamental reason why we can obtain high monopole charge in this case, which results in a new type of topological nodal lines. To define the half manifold index, we utilize the two-fold rotational symmetry along z. It can be easily checked that if we have only type-a (or type-b) bands in our system, the C_{4h} symmetry ensures that the two-fold rotation must be an identity operator ($+I$ if we only have type-a bands and $-I$ if we only have type-b bands). As a result,

$$H_{C_2\boldsymbol{k}} = C_2 H_{\boldsymbol{k}} C_2^{-1} = H_{\boldsymbol{k}}. \tag{4.31}$$

Here, we utilized the fact that H and C_2 commute with each other, since C_2 is an identity operator (up to a -1 sign for type-b bands). As a result, for the manifold we choose, an extra symmetry is obtained $H_{C_2\boldsymbol{k}} = H_{\boldsymbol{k}}$. This symmetry implies that as far as our Hamiltonian is concerned, we can merge momentum points $C_2\boldsymbol{k}$ and $\boldsymbol{k}$. For a half manifold ($0 < k_x < \pi$), this procedure sews together momentum points on the edge, and transforms the half manifold into a compact manifold. Thus, we can define a Z_2 monopole charge for it. And it is easy to verify that the other half manifold must have the same monopole charge.

In the proof above, we assumed that the system only contains type-a (or type-b) bands. In a real systems, in principle, both types of bands shall exist. In this part, we argue that our conclusion will remain as along as other bands does not come close to the Fermi energy. The argument is based on the stability of the topological nodal lines that we found in family 4 and 5 (with C_{4h} symmetry) which carry monopole charge 2. As our proof above has showed, these monopole-charge-2 nodal lines remain stable if we go beyond four-band model, as long as the extra bands that we added to the system have the same time-reversal type. Let us introduce extra bands with different time reversal type as a perturbation and see if these nodal lines remain stable. Without loss of generality, here again we start from the case with only type-a

bands and a monopole-charge-2 nodal-line cage, and then introduce some extra type-b bands at energy away from the Fermi energy. For a topological nodal line, it is known that as long as the time-reversal and space-inversion symmetry is preserved (and spin-orbit couplings remain negligible), a nodal line cannot be gapped out unless it is first shrunk into a nodal point. As we discussed above, for a monopole-charge-2 nodal line, it has to preserve the rotational symmetry and thus when it shrinks into a nodal point, it must be a point along the high symmetry axis ($k_x = k_y = 0$ in this case). Along such a high symmetry line, type-a and type-b bands cannot hybridize, because they have different rotational eigenvalues under a C_4 rotation. As a result, even if extra type-b bands are introduced, they are incapable of gapping out this nodal line/point. This argument shows that at least in the perturbative range, these high-monopole-charge nodal lines are stable, regardless of how many bands we include in the system and what type of bands we include.

What we will not consider here are extra type-b bands added near the Fermi energy (inside the gap). This would be a much more complicated case, and whether the interplay between type-a and type-b bands at the Fermi energy can generate interesting novel phenomena remains an open question and will be explored in a separate project.

The same analysis can be generalized to certain cases with six-fold rotations, which proves the stability of the nodal line with monopole charge 2 in systems with C_{6h} symmetry.

CHAPTER V

Strongly Correlated Topological Phases in Moiré Superlattices

The previous chapters focus on topological phases in electronic systems that can be adiabatically connected to the limit without electronic interactions, where topology represents the obstruction for adiabatic deformation without gap closing or symmetry breaking. For strongly correlated electronic systems, there is a different notion of topology in terms of the intrinsic topological order [99]. A gapped phase with topological order has multiple degenerate manybody ground states if the phase is realized on a torus in the real space. These ground states cannot be distinguished by any local measurement. The excitations above these ground states are quasiparticles with fractional statistics. An example of topological order can be illustrated by the fractional quantum Hall states.

The fractional quantum Hall effect was discovered in 1982 [100] where the Hall conductance of a 2D electronic gas in strong magnetic field shows quantized plateaus $\sigma_{xy} = \nu\frac{e^2}{h}$ when the filing fraction ν is some specific rational numbers, e.g., the Laughlin state at $\nu = \frac{1}{2p+1}$ [101], the Jain's states at $\nu = \frac{p}{2np\pm1}$ [102], the Moore-Read state at $\nu = \frac{1}{2}$ [103, 104], and many others. The ground states of these systems have topological order. There is a finite energy gap separating the ground state and the other excited states, and the excitations in these systems are quasiparticles

called anyons with fractional charge and fractional statistics. The interaction between electrons is crucial for this effect, otherwise the system contains partially filled Landau level and the ground state will not be gapped.

Fractional quantum Hall states can also be stabilized in a lattice system without the external magnetic field, and the corresponding state is the fractional Chern insulator (FCI) [105, 106, 107, 108, 109, 110, 111, 112]. In FCI the role of the uniform external magnetic field is played by the nonzero Berry curvature, which implies it requires the insulator to have nontrivial Chern number, because otherwise the average of Berry curvature is zero. Although the concept of FCI has been proposed for a long time, the FCI without external magnetic field has not been experimentally realized yet. One of the challenges is that the fractional quantum Hall states typically requires the electron interaction strength to dominate over the width of energy bands. The Landau levels for 2D electron gas under strong magnetic field naturally satisfies this condition. For electronic insulators, this condition is not easily satisfied. Therefore, a system with a nearly flat band with nontrivial Chern number may be a good candidate to realize the FCI states.

The Moiré superlattice which is recently under intense study provides a plausible platform to realize the FCI states. The Moiré superlattice is formed when two layers of lattices with similar structure are slightly misaligned with each other, as shown in Fig.(5.1) (a) where two identical honeycomb lattices are aligned with a small twist angle θ. The Moiré superlattice has much larger lattice constant $a_M = a_0/\theta$, where a_0 is the lattice constant of the original lattice. Therefore, the Brillouin zone of the Moiré superlattice is reduced, as in Fig.(5.1) (b). The formation of Moiré superlattice has a significant effect on the electronic band structure. Due to the hybridization of bands and reduced size of Brillouin zone, the bandwidth is significantly reduced, resulting in nearly-flat Moiré bands. The filling fraction can be tuned by controlling the electric gating. The Moiré superlattices open up a new pathway to stabilize various strongly-

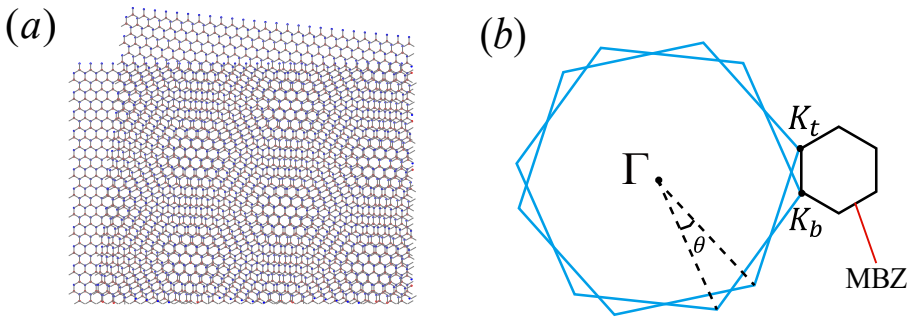

Figure 5.1: (a): Moiré superlattice formed by two layers of identical honeycomb lattices. (b): The Moiré Brillouin zone (MBZ) of the Moiré superlattice is determined by the twist angle θ. The MBZ is much smaller than the original Brillouin zone.

correlated phases such as superconductors and correlated insulators [113, 114, 115, 116, 117, 118, 119, 120, 121, 122, 123, 124, 125, 126, 127, 128, 129, 130, 131, 132]. Furthermore, the Moiré bands can also be topologically nontrivial with a nonzero Chern number [133, 134, 135, 136, 137]. Therefore, the Moiré superlattices offer a promising route to realize the long-sought fractionalized topological order [138, 139, 140, 141, 142].

In our work [143], we study the Moiré superlattice formed by twisted bilayer transition metal dichalcogenides (TMD) and seek the possibility to realize the fractional Chern insulator states. Comparing with the Moiré systems based on graphene, the TMD materials has an advantage that the spin-orbit coupling in TMD is strong, which leads to spin-valley locking that breaks the spin rotation SU(2) symmetry to U(1). This will eliminate the Goldstone mode of spin waves and can help stablize the FCI states. On the experimental side, recently, gapped electronic states at various fractional fillings (e.g., 1/3) were reported in TMD Moiré superlattices, e.g., WSe_2/WS_2, in addition to the more conventional Mott gap at half filling [128, 144, 145, 146, 147]. In these TMD Moiré superlattices, the observed gapped states were interpreted as Wigner crystals/charge order of electrons stabilized by strong Coulomb repulsion rather than FCI, partially because the underlying single-particle bands are topologi-

cally trivial [148].

To find FCI states, we need Moiré bands that are topologically nontrivial. It has been shown in [149] that some TMD homobilayers may host topologically nontrivial bands with non-zero spin/valley-Chern numbers. Therefore, our work focus on this type of Moiré superlattices. In contrast to a partially filled Chern band, because these systems preserve the time-reversal symmetry, two types of fractional states are in principle allowed (a) time-reversal invariant fractional topological insulators [150] and (b) FCIs via spontaneously breaking the time-reversal symmetry. The key focus of this study is whether Coulomb repulsion could stabilize some of these fractional states in TMD Moiré superlattices.

In our work [143], utilizing exact numerical methods, we show that at certain twisting angle and filling, by simply increasing the Coulomb interaction strength in such TMD Moiré superlattices, the system undergoes a quantum phase transition that spontaneously breaks the time-reversal symmetry by polarizing electrons into one of the two valleys. Further increase of Coulomb interaction will trigger a second quantum phase transition, and stabilize a FCI. This conclusion is confirmed by multiple numerical observables, including topological degeneracy, fractional Chern number, and entanglement spectrum. For excitations, our numerical studies observe both (intravalley) fractional excitations from the fractional topological order and (intervalley) valley-wave excitations from the spontaneous symmetry breaking. Such features could offer unique experimental signatures for these novel states. We also explore the possibility of stabilizing the non-Abelian Moore-Read state using the three-body interactions, which can be realized in TMD Moiré superlattice sandwiched between nonlinear dielectric media [151].

5.1 Model of twisted bilayer TMD

We consider twisted homobilayer TMD materials. For each single layer, the low energy electronic states reside at the valence band maxima at $\pm\boldsymbol{K}$ valleys. Contrary to bilayer graphene systems where the valley and spin degrees of freedom are both present, in TMD each valley in the top valence band has fixed spin orientation due to strong spin-orbit coupling and the broken inversion symmetry [152]. With a small twist angle θ between two layers, the $+\boldsymbol{K}$ valley for the top and bottom layers are shifted to $\boldsymbol{K}_t$ and $\boldsymbol{K}_b$ in the Moiré Brillouin zone (MBZ) respectively, as shown in Fig.(5.2) (b). For convenience we choose the rhombus-shaped MBZ and set the point $\boldsymbol{M} = (\boldsymbol{K}_t + \boldsymbol{K}_b)/2$ as the origin. We employ the continuum model [153] in which the Moiré Hamiltonian for the $+\boldsymbol{K}$ valley is:

$$H_+(\boldsymbol{k},\boldsymbol{r}) = \begin{pmatrix} -\frac{\hbar^2(\boldsymbol{k}-\boldsymbol{K}_b)^2}{2m^*} + \Delta_{\mathfrak{b}}(\boldsymbol{r}) & \Delta_T(\boldsymbol{r}) \\ \Delta_T^\dagger(\boldsymbol{r}) & -\frac{\hbar^2(\boldsymbol{k}-\boldsymbol{K}_t)^2}{2m^*} + \Delta_{\mathfrak{t}}(\boldsymbol{r}) \end{pmatrix} \tag{5.1}$$

Here m^* is the effective mass. The form of Moiré potential, $\Delta_{b,t,T}$, is dictated by the D_3 crystalline symmetry and a combination of C_{2z} rotation followed by switching the two layers, and can be parameterized by [149]:

$$\begin{aligned} \Delta_T(\boldsymbol{r}) &= w\left(1 + e^{-i\boldsymbol{G}_2\cdot\boldsymbol{r}} + e^{-i\boldsymbol{G}_3\cdot\boldsymbol{r}}\right) \\ \Delta_l(\boldsymbol{r}) &= 2w_z \sum_{j=1,3,5} \cos\left(\boldsymbol{G}_j\cdot\boldsymbol{r} + l\psi\right), \end{aligned} \tag{5.2}$$

where $l \in \{b,t\} = \{+1,-1\}$ and $\boldsymbol{G}_j$ is the Moiré reciprocal lattice vectors with length $|\boldsymbol{G}_j| = \frac{4\pi}{\sqrt{3}a_M}$ and polar angle $\frac{\pi(j-1)}{3}$. Here $a_M = a_0/\theta$ is the Moiré lattice constant for a small twisted angle θ and a_0 is the lattice parameter of TMD. Equation (5.1) is the Hamiltonian for the valley $+\boldsymbol{K}$, while the Hamiltonian for the valley $-\boldsymbol{K}$ can be obtained by the time-reversal symmetry $H_-(\boldsymbol{k},\boldsymbol{r}) = H_+(-\boldsymbol{k},\boldsymbol{r})^*$. To be specific,

our following discussions focus on twisted $MoTe_2$ homobilayer, whose parameters have been obtained from the first-principle calculations $(\hbar^2/2m^*a_0^2,\ w_z,\ w,\ \psi) = (495\text{ meV},\ 8\text{ meV},\ -8.5\text{ meV},\ -89.6^\circ)$ [149]. To obtain the dispersion relation, we need to perform a Fourier transformation and solve for the eignvalues in the extended momentum space. In the momentum space the basis is chosen to be like $(e^{i\boldsymbol{k}\cdot\boldsymbol{r}}\chi_b, e^{i\boldsymbol{k}\cdot\boldsymbol{r}}\chi_t, e^{i(\boldsymbol{k}+\boldsymbol{G}_1)\cdot\boldsymbol{r}}\chi_b, e^{i(\boldsymbol{k}+\boldsymbol{G}_1)\cdot\boldsymbol{r}}\chi_t, ..., e^{i(\boldsymbol{k}+\boldsymbol{G}_j)\cdot\boldsymbol{r}}\chi_b, e^{i(\boldsymbol{k}+\boldsymbol{G}_j)\cdot\boldsymbol{r}}\chi_t, ...)^T$ where $\chi_{b/t}$ are localized functions at bottom/top layer, and G_j are taken to be in a large set $\{G\}$. A truncation is needed for the set $\{G\}$, which is chosen to be a symmetric hexagon of radius $6|G_1|$, as in Fig.(5.3) (b). Denote the number of reciprocal lattice vectors in the truncation set $\{G\}$ as N_G, then the single particle Hamiltonian is a $2N_G \times 2N_G$ matrix where the factor 2 comes from the two layers, and its wave function $|u_{\tau,\boldsymbol{k}}\rangle$ is a $2N_G$-component column vector. Here $\tau = \pm$ refers to the two valleys.

The top valence band of a TMD single layer splits into multiple Moiré bands due to the Moiré potential. Due to its strong spin-orbit coupling and the spin-valley locking, the spin- and valley- degrees of freedom are locked together in these materials, and thus below we will use these two terminologies interchangeably. As shown in Fig.(5.2) (c) and (d), when the twist angle is close to $\theta_0 = 1.38^\circ$, the top Moiré band becomes nearly flat. The flatness of a band can be characterized by a ratio of the gap between the nearest bands to its band width. For the top Moiré band, the ratio can be as large as 13. When $\theta < 3.1^\circ$, The top Moiré band is topological characterized by a valley/spin Chern number $C = \pm 1$ due to the skyrmion lattice pseudo spin textures of the Moiré potential [149]. The Chern number for the opposite valley/spin is opposite as required by time-reversal symmetry. Thus, at the single-particle level, such TMD homobilayer can realize a quantum valley/spin Hall insulator. As interactions are turned on, as will be shown below, we find that this nearly flat top Moiré band can host fractional topological phases at fractional filling.

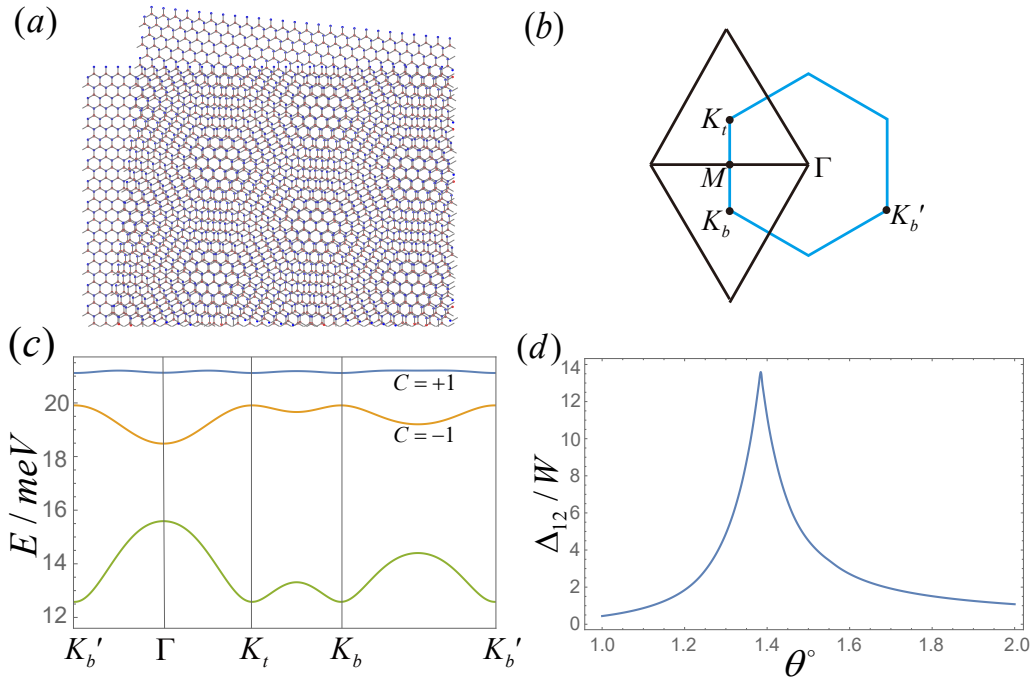

Figure 5.2: (a): Schematic view of the Moiré superlattice. (b): We choose the Moiré Brillouin zone (MBZ) to be the rhombus and the origin in momentum space is chosen at M. (c): Moiré band structure at $\theta = 1.38°$. The top Moiré band is nearly flat with Chern number ± 1. (d): The gap ratio $\frac{\Delta_{12}}{W} = \frac{\min(E_1(\boldsymbol{k}))-\max(E_2(\boldsymbol{k}))}{\max(E_1(\boldsymbol{k}))-\min(E_1(\boldsymbol{k}))}$ as a function of twisted angle θ, where $E_1(\boldsymbol{k})$ ($E_2(\boldsymbol{k})$) is the energy of the first (second) topmost Moiré band.

5.2 Projection of Coulomb interaction to a single band

We introduce screened Coulomb interaction and project it to the nearly flat top Moiré band [154]:

$$\begin{aligned} H_{\text{int}} &= \frac{1}{2A}\sum_{\boldsymbol{q}} :\rho(\boldsymbol{q})V(\boldsymbol{q})\rho(-\boldsymbol{q}): \\ &= \sum_{\boldsymbol{k},\boldsymbol{k}',\boldsymbol{q},\tau,\tau'} \frac{U}{2N_{\text{cell}}} v(\boldsymbol{q})\lambda_{\tau,\boldsymbol{q}}(\boldsymbol{k})\lambda_{\tau',\boldsymbol{q}}(\boldsymbol{k}')^* \\ &\quad C^\dagger_\tau(\boldsymbol{k})C^\dagger_{\tau'}(\boldsymbol{k}'+\boldsymbol{q})C_{\tau'}(\boldsymbol{k}')C_\tau(\boldsymbol{k}+\boldsymbol{q}), \end{aligned} \tag{5.3}$$

where $\tau = \pm$ is the valley index, and $\lambda_{\tau,\boldsymbol{q}}(\boldsymbol{k}) = \langle u_{\tau,\boldsymbol{k}}|u_{\tau,\boldsymbol{k}+\boldsymbol{q}}\rangle$ is the form factor originated from the projection. Here $v(\boldsymbol{q}) = 4\pi\tanh(qd)/\sqrt{3}qa_M$ is the dimensionless screened Coulomb potential with d the separation between the electrode and Moiré superlattice, which is set to $d = 2a_M$ in the calculations. A is system area and N_{cell} is the number of the unit cells in the calculations. The coefficient of $v(\boldsymbol{q})$ is chosen to make U equal to the bare Coulomb potential between two particles separated by a_M. $C_\tau(\boldsymbol{k})$ is the annihilation operator for single particle state $|u_{\tau,\boldsymbol{k}}\rangle$. Note that the sum over $\boldsymbol{k},\boldsymbol{k}'$ is inside the first Brillouin zone while the sum over $\boldsymbol{q}$ is over $(-\infty,\infty)\times(-\infty,\infty)$. We have chosen the convention that $C_\tau(\boldsymbol{k}) = C_\tau(\boldsymbol{k}+\boldsymbol{G})$, $u_{\tau,\boldsymbol{k}+\boldsymbol{G}'}(\boldsymbol{G}) = u_{\tau,\boldsymbol{k}}(\boldsymbol{G}+\boldsymbol{G}')$. Due to the fact that $|u_{\tau,\boldsymbol{k}}\rangle \neq |u_{\tau,\boldsymbol{k}+\boldsymbol{G}}\rangle$, care must be taken in selecting the correct $|u_{\tau,\boldsymbol{k}}\rangle$ when taking the inner product in the above interaction.

To apply exact diagonalization, define the system size to be $N_1 \times N_2$ and use an integer $n \in [0, 2N_1N_2 - 1]$ to represent both momentum n_k and valley n_τ, such that

n_k is inside the first BZ. Eq.(5.3) is rewritten as

$$\hat{V} = \sum_{n,n',m',m} V(n,n',m',m) C_n^\dagger C_{n'}^\dagger C_{m'} C_m \tag{5.4}$$

$$V(n,n',m',m) = \sum_{G\in\{G\}'} \frac{U}{2N_{cell}} v(m_k - n_k + G) \langle u_{n_\tau,n_k} | u_{m_\tau,m_k+G}\rangle \delta(n'_\tau, m'_\tau) \times \langle u_{n'_\tau,n'_k+G_0+G} | u_{m'_\tau,m'_k}\rangle \delta(n_\tau, m_\tau) \delta(\overline{m_k + m'_k - n_k - n'_k}, 0) \tag{5.5}$$

$$G_0 = m_k + m'_k - n_k - n'_k \in \{G\} \tag{5.6}$$

Here $\overline{k+q}$ means the part of momentum $k+q$ inside the first Brillouin zone, such that $\overline{k+q} = k+q-G$ for some Moiré reciprocal lattice vector G. The summation of G is over all the reciprocal lattice vectors. It comes from the infinite summation of q. In practice this summation is truncated to a set $\{G\}'$ of finite range. The delta functions represent valley and momentum conservation. The overline in the last delta function shows the momentum conservation is defined only module a reciprocal lattice vector, which allows a situation with $m_k + m'_k - n_k - n'_k = G_0 \neq 0$. In this case the nonzero G_0 will also appear in the above inner product $\langle u_{n'_\tau,n'_k+G_0+G} | u_{m'_\tau,m'_k}\rangle$. This G_0 ensures the correct state is used for taking the inner product. As illustrated in Fig.(5.3) (c), if the first BZ is taken to be the rhombus and m, n, m', n' are given by the black dots, these momentum points satisfy $m_k - n_k = n'_k + G_2 - m'_k = q$, therefore the G_0 constant is $G_0 = m_k + m'_k - n_k - n'_k = G_2 \neq 0$. The $G = 0$ term in the summation of Eq.(5.5) has an inner product between n'' and m':

$$\langle u_{n'_\tau,n'_k+G_0} | u_{m'_\tau,m'_k}\rangle = \langle u_{n'_\tau,n''_k} | u_{m'_\tau,m'_k}\rangle \tag{5.7}$$

Where $n'_k + G_0 = n''_k$ has been used. With the G_0 constant, the Coulomb interaction correctly involves the wave function at m, n, m', n'' linked by the blue lines of momentum q in Fig.(5.3) (c). If there is no such G_0 term, the interaction will involve $\langle u_{n'_\tau,n'_k} | u_{m'_\tau,m'_k}\rangle$ represented by the red line in Fig.(5.3) (c) instead, which will lead to

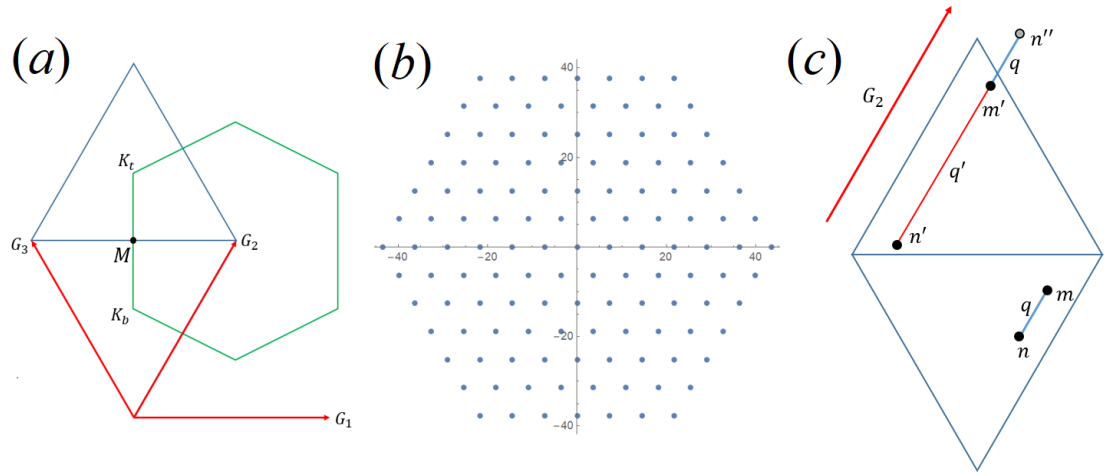

Figure 5.3: (a) The plot of Moiré Brillouin zone. (b) The truncation of the set $\{G\}$. The nearest neighbour distance in this figure is $|G_1|$. (c) The momentum points related by Coulomb interaction.

incorrect result.

The summation in Eq.(5.5) is truncated to a set $\{G\}'$, which is taken to be a hexagon of radius $4|G_1|$. $\{G\}'$ is chosen to be smaller than $\{G\}$, which is the truncation of single particle Hamiltonian, because the single particle wave function will be less accurate when $k+G$ is close to the boundary of $\{G\}$. Therefore, $\{G\}$ is taken larger than $\{G\}'$ to ensure the accuracy of wave function inside $\{G\}'$.

The single particle Hamiltonian only gives the wave function in the positive valley, and those in the negative valley are obtained by time-reversal:

$$u_{-,k}(G) = u_{+,-k}(-G)^* \tag{5.8}$$

The origin of the BZ is chosen to be the M point in Fig.(5.3) (a), and M is the middle point of the line joining $\pm k$. Note that the range of k above is $(-\infty,\infty)\times(-\infty,\infty)$, rather than the first BZ. When calculating the inner product in Eq.(5.5), the wave function at k and $k+G$ need to maintain phase coherence. For $\pm$ valleys, these

conditions are:

$$u_{+,k+G'}(G) = u_{+,k}(G+G') \tag{5.9}$$

$$u_{-,k+G'}(G) = u_{-,k}(G+G') \tag{5.10}$$

The matrix element between arbitrary manybody states can be obtained from Eq.(5.5). Let $|\psi\rangle$ and $|\psi'\rangle$ be simple direct product states whose creation operators are ordered, $|\psi\rangle = C^\dagger_{i_{N-1}}...C^\dagger_{i_0}|0\rangle$, with $i_{N-1} > ... > i_1 > i_0$. Suppose distinct manybody states $|\psi\rangle$ and $|\psi'\rangle$ have nonzero matrix element, which means there exist $i > j, i' > j'$ such that $\langle\psi'|C^\dagger_{j'}C^\dagger_{i'}C_iC_j|\psi\rangle \neq 0$. Then the matrix element is given by:

$$\langle\psi'|\hat{V}|\psi\rangle = (-1)^{\mu(i,j)}(-1)^{\mu'(i',j')}(V(j',i',i,j)-V(j',i',j,i)-V(i',j',i,j)+V(i',j',j,i)) \tag{5.11}$$

Where $V(j',i',i,j)$ is in Eq.(5.5), $\mu(i,j)$ is the number of "1" between the ith and jth bits in the bit-representation of $|\psi\rangle$. If $|\psi\rangle = |\psi'\rangle$, then $i = i'$ and $j = j'$, and the matrix element involves a sum over all combinations of i, j that do not annihilate the state:

$$\langle\psi|\hat{V}|\psi\rangle = \sum_{i>j,\psi_i=\psi_j="1"} (V(j,i,i,j) - V(j,i,j,i) - V(i,j,i,j) + V(i,j,j,i)) \tag{5.12}$$

Where ψ_i is the ith bit in the bit-representation of $|\psi\rangle$ that can take either "1" or "0". Eq.(5.12) gives the matrix elements for the manybody Hamiltonian matrix in the exact diagnonalization.

The Hamiltonian in Eq.(5.3) preserves a valley $U(1)_v$ symmetry, which could be broken by intervalley impurity scatterings. However, because of the large momentum transfer in the intervalley scattering process, the scattering due to the Moiré superlattice disorders is suppressed. Therefore the $U(1)_v$ symmetry becomes a good symmetry of the system, and we treat it as an exact symmetry of the Hamiltonian. In

this model, there are two competing symmetry breaking states: an intervalley coherent state that breaks the valley $U(1)_v$ symmetry and an valley/spin polarized state that breaks the time reversal symmetry. At half filling of the topmost band (account for valley degree of freedom), our Hartree-Fock analysis and exact-diagonalization results both suggest that a valley-polarized state is energetically favored, which spontaneously breaks the time-reversal symmetry and leads to a interaction-induced Chern insulator. Similar valley polarized state has also been discussed in graphene Moiré superlattices [134, 155]. At fractional filling, in principle, two types of fractional topological states might emerge, a fractional Chern insulator or a fractional topological insulator [150, 156], depending on whether the time-reversal symmetry is spontaneously broken or preserved, and our exact diagonalization below show that the FCI is favored and stabilized in our system.

5.3 Valley polarized FCI

We define the filling factor $\nu = 2\rho_e/\rho_s$, where ρ_e is the electron density occupying the top Moiré band and ρ_s is the electron density for the full filling of the two-fold degenerate top Moiré band. The factor 2 accounts for the valley degree of freedom. Using exact diagonalization, at $\nu = 1/3$ we observe numerical evidence of spontaneous valley polarization and FCI in the strong interaction limit, as shown in Fig.(5.4) (a). With 8 electrons and 4×6 unit cells ($4 \times 6 \times 2$ single-particle states including both valleys), the ground states are fully valley polarized with three nearly-degenerate ground states for each valley polarization, separated from the excited states by an energy gap of the order of 2 K. We calculated the many-body Chern number of each ground state utilizing twisted boundary conditions [109], and the topological index is found to be 1/3, characterizing a 1/3 FCI phase. This conclusion is further supported by the total momentum for each ground state, which obeys the generalized Pauli exclusion rule of FCIs [157].

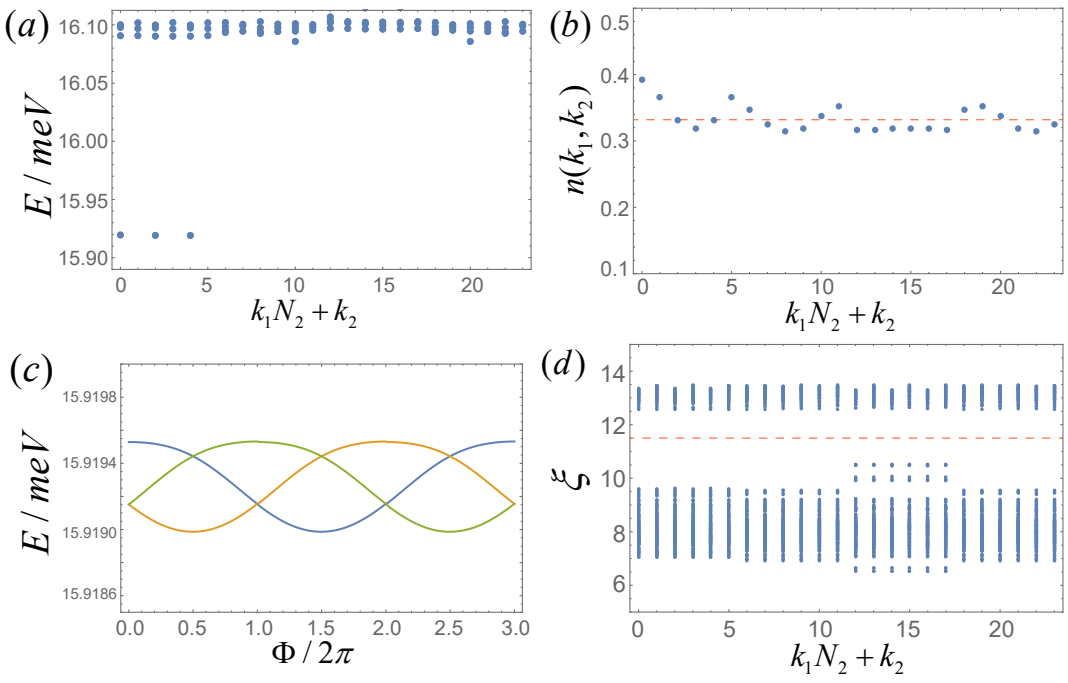

Figure 5.4: Numerical exact diagonalization results for 8 particles in 4×6 Moiré lattice. We choose $\theta = 1.38°$ and $U = 1.38$ meV. The bandwidth at this twist angle is $W = 0.083$ meV. Here $N = N_1 \times N_2/3$ is the number of particles. (a): Energy of many-body states labeled by momentum $k_1N_2 + k_2$. There are three nearly degenerate ground states in each valley with total momentum $(k_1, k_2) = (0, 0), (0, 2), (0, 4)$ respectively. (b): The occupation number of single particle states $n(k_1, k_2)$ for each of the three many-body ground states. The nearly uniform distribution of $n(k_1, k_2)$ suggests the ground state is an incompressible liquid. (c): Under flux insertion along k_2 direction, the ground states evolve into each other. (d): Particle entanglement spectrum (PES) for the separation of $N_A = 4$ particles.

The occupation number $n(k_1, k_2)$ of single particle states for each of the three many-body ground states are plotted in Fig.(5.4) (b). $n(k_1, k_2)$ is uniformly distributed for different single particle states, consistent with the fact that the ground state is an incompressible liquid. When flux is inserted along k_2 direction, the three nearly degenerate ground states evolve into each other under a 2π flux, and they evolve back to the original states under a 6π flux, as shown in Fig.(5.4) (c). The excitation gap maintains throughout the whole flux insertion process.

The topological nature of the ground states are further confirmed by our calculation of the particle entanglement spectrum (PES) [157]. To compute PES, we divide the N particles into two collections of N_A and $N_B = N - N_A$ particles and trace out N_B particles to get the reduced density matrix ρ_A. The PES levels ξ are obtained from the logarithm of eigenvalues of ρ_A, and are labeled by the total momentum of the remaining N_A particles, as shown in Fig.(5.4) (d) where we choose $N_A = 4$ for $N = 8$ particles. There is a clear entanglement gap with 2730 levels below the gap, consistent with the counting of quasihole excitation in the $\nu = 1/3$ FCI [157].

To exam the finite-size effect, we study the scaling of the many-body gap Δ with various system sizes at a fixed interaction strength. For a genuine FCI, Δ remain finite in the thermodynamic limit when both N_1 and N_2 approach infinity. However Δ should vanish if only one of N_1 or N_2 approaches infinity, because this limit is a one-dimensional system which should not support FCI [108]. This is confirmed in Fig.(5.5) (a), which shows Δ decreases when N_1 is fixed at 3 and N_2 increases from 4 to 8, but Δ increases when the system size changes from 3×8 to 4×6.

We then map out the phase diagram at $\nu = 1/3$ filling as a function of the interaction strength U which can be controlled by distance between the electrodes and the Moiré superlattice in experiments. We find a valley non-polarized Fermi liquid at a small U, a valley-polarized Fermi liquid at intermediate interaction and the FCI phase with valley polarization at strong interaction. The phase transition between the valley-polarized Fermi liquid and FCI can be described by Ginzburg-Landau theory with a Chern-Simons term. The phase boundaries between them are denoted as U_1 and U_2, and U_1/W and U_2/W for various twist angles and system sizes are displayed in Fig.(5.5) (c). Note that at $\theta = 1.38^\circ$ the single particle Moiré band has the largest gap to bandwidth ratio, see Fig.(5.2) (d). Therefore, Fig.(5.5) (c) implies that the parameter region for valley polarized Fermi liquid (the separation between U_1/W and U_2/W) becomes smaller when the bandwidth decreases, which may suggest in

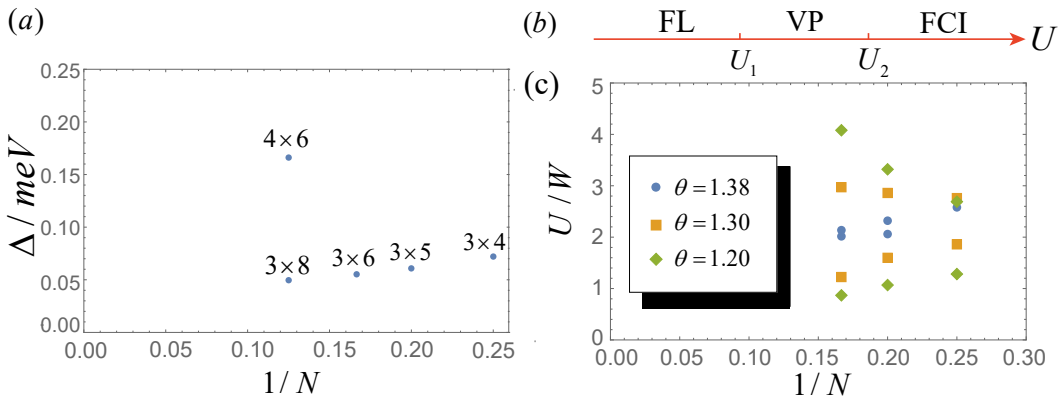

Figure 5.5: (a): The many-body gap Δ for various system sizes at $v = 1/3$ filling. The interaction strength is fixed to be $U = 1.38$ meV. The increase of Δ in 4×6 system suggests the gap persists in the two-dimensional thermodynamic limit. (b): The phase diagram for Fermi liquid (FL), valley polarized (VP) FL and fractional Chern insulator (FCI) at different interaction strength U. (c): The phase boundaries U_1/W and U_2/W for various system size and twist angle. We choose system size to be $3\times4, 3\times5$ and 3×6; and twist angles $\theta = 1.20°, 1.30°$ and $1.38°$. Every two points with the same color in the same column represent U_1/W and U_2/W respectively.

the ideal flat band limit there is a direct phase transition from Fermi liquid phase to FCI phase with valley polarization. This is consistent with the quantum Hall systems with flat Landau levels, where the interaction stabilizes simultaneously the fractional quantum Hall state with spin polarization.

5.4 Excitation above the FCI ground states

Here we study the charge neutral excitations above the FCI ground states. As a consequence of the spontaneous valley polarization, we consider the valley waves excitation $|\Psi_v(\boldsymbol{q})\rangle = \sum_{\boldsymbol{k}} z_{\boldsymbol{k}} C_+^\dagger(\boldsymbol{k}+\boldsymbol{q}) C_-(\boldsymbol{k})|\Psi_-\rangle$, where $|\Psi_-\rangle$ is the FCI ground state with $\tau = -$ valley fully occupied and $z_{\boldsymbol{k}}$ is variational parameter. The presence of the from factor in Eq. (5.3) breaks the valley pseudospin SU(2) rotation system down to the valley $\mathrm{U}(1)_v$ symmetry. As a result, the valley wave excitation are gapped. Indeed, the calculated valley wave spectrum for 8 particles in 4×6 lattice shown

in Fig. (5.6) are gapped, and can be fitted by $E_w(\boldsymbol{q}) = Jq^2 + A$. The valley wave disperses weakly in momentum and thus is well localized in space.

In quantum Hall ferromagnets, a pair of skyrmions has lower energy than the particle-hole bound state [158]. The system size limitation in the exact diagonalization does not allow us to study the valley skyrmion excitation in our numerical calculations. Here we use effective Hamiltonian for valley pseudospin $\mathbf{n}$: $H_n = \int dr^2 \left[\frac{J}{2}(\nabla \mathbf{n})^2 - \frac{A}{2}n_z^2\right]$, where J and A are given by the valley wave spectrum. A single skyrmion is no longer a stable excitation in the presence of the easy axis anisotropy term. This can be seen from the rescaling of the length $r \to \lambda r$, $\mathbf{n}_s(r) \to \mathbf{n}_s(\lambda r)$ for an arbitrary spin texture $\mathbf{n}_s(r)$. The first term in H_n is scaling invariant, but the second term scale as $-1/\lambda^2$. The system gains energy by shrinking the size of $\mathbf{n}_s$, and therefore skyrmions are not stable for H_n. The absence of skyrmions in our system can also be attributed to the opposite Chern number for the opposite valley. One cannot rotate $\mathbf{n}$ from one valley to opposite valley adiabatically without closing the energy gap, which implies the existence of anisotropy for $\mathbf{n}$. In this regard, the TMD Moiré superlattice is distinct from the graphene Moiré superlattice. At a finite skyrmion density, which can be achieved by electron doping in the FCI state, there exist Coulomb repulsion between skyrmions because skyrmions are charged. The Coulomb repulsion prevents an individual skyrmion from collapsing and stabilizes a skyrmion lattice [159].

In comparison, the lowest intravalley many-body excitation has lower energy than valley wave excitation for the parameters we used, i.e., the energy difference between the lowest fully-polarized excited state and the FCI state is $E_{mb} = 0.167$ meV $< E_w$, as shown in the inset of Fig.(5.6). Nevertheless, the valley wave excitation remains a stable excitation because the decay of the valley wave to the intravalley many-body excitations are forbidden as a result of valley $\mathrm{U}(1)_v$ symmetry. Intravalley many-body excitations has valley quantum number 0, while the valley wave has valley quantum

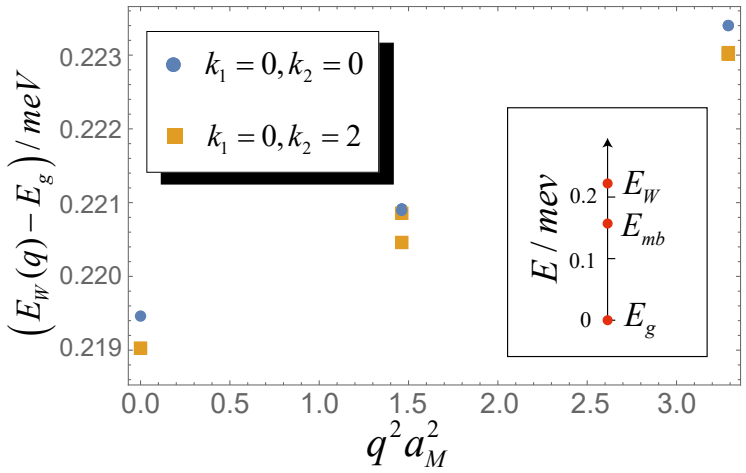

Figure 5.6: Dispersion of valley wave excitation $E_w(\boldsymbol{q})$. Excitation above the ground state with total momentum $k_1 = 0, k_2 = 0$ ($k_1 = 0, k_2 = 2$) are labeled by the squares and circles respectively. The slight energy difference for these two ground states is caused by finite size effect. The inset compares the energy of the lowest valley wave excitation E_w, the lowest intravalley many-body excitation E_{mb} and the ground state energy E_g.

number 2.

5.5 Moore-Read states

The FCI at $\nu = 1/3$ filling supports Abelian anyons. In fractional quantum Hall, the proposed Moore-Read state for the plateau at $v = 5/2$ supports non-Abelian anyons, which can be exploited for topological quantum computation [160]. Here we study the stabilization of the Moore-Read state in TMD Moiré superlattice. It turns out that the Coulomb interaction in Eq. (5.3) does not stabilize a gapped state at $v = 1/2$. Here we introduce three-body interaction, which can be induced by sandwiching the Moiré superlattice with nonlinear dielectric media [151], to favor the Moore-Read state. For example, the nonlinear contribution to electric energy, $\mathcal{E}_\mu \mathcal{E}_\nu \mathcal{E}_\eta$ (here $\mathcal{E}$ is electric field), produces three-body Coulomb interaction when electrons are

placed to the dielectric media. We consider a three-body interaction:

$$\hat{V}_3 = \frac{1}{6}\int d\boldsymbol{r_1} d\boldsymbol{r_2} d\boldsymbol{r_3} V_3(\boldsymbol{r_1}, \boldsymbol{r_2}, \boldsymbol{r_3}) : \rho(\boldsymbol{r_1})\rho(\boldsymbol{r_2})\rho(\boldsymbol{r_3}) :$$
$$V_3(\boldsymbol{r_1}, \boldsymbol{r_2}, \boldsymbol{r_3}) = U_3(f(\boldsymbol{r_1} - \boldsymbol{r_2})f(\boldsymbol{r_2} - \boldsymbol{r_3})$$
$$+f(\boldsymbol{r_2} - \boldsymbol{r_3})f(\boldsymbol{r_3} - \boldsymbol{r_1}) + f(\boldsymbol{r_3} - \boldsymbol{r_1})f(\boldsymbol{r_1} - \boldsymbol{r_2})). \tag{5.13}$$

The Fourier transform of $f(\boldsymbol{r})$ in momentum space is $\frac{2\pi}{k^2+k_s^2}$, representing a short-range interaction with a screening length $1/k_s$. We found that when the three-body interactions dominate over the Coulomb repulsion, a Moore-Read state is stabilized. As shown in Fig.(5.7), the ground states (marked in red) are valley polarized with sixfold quasi-degeneracy in one valley, and are separated from the excited states by an energy gap. The momenta of the ground states for 4×5 systems with 10 particles are $(k_1, k_2) = (0,0), (2,0), (1,0), (1,0), (3,0), (3,0)$ respectively, while those for 4×4 systems with 8 particles are $(k_1, k_2) = (0,0)$, consistent with the requirement of (2,2)-admissible states characterizing a Moore-Read state [157]. Consistent results are obtained for spectral flow and entanglement spectrum as well, as shown in Fig.(5.7) (c) and (d).

5.6 Discussions

We show that TMD Moiré superlattices can host fractional topological states via spontaneously breaking the time-reversal symmetry, using realistic parameters of TMD Moiré superlattices. Comparing with graphene, the spin-valley locking in TMD materials breaks the $SU(2)$ spin rotation symmetry and eliminates the spin wave Goldstone modes, which could help stabilize the FCI states. The valley contrasting Chern number in TMD Moiré superlattices also dictates the symmetry breaking states, hence the nature of fractionalized topological states, and also the low energy excitations in the FCI. The gapped nature of these states can be detected by trans-

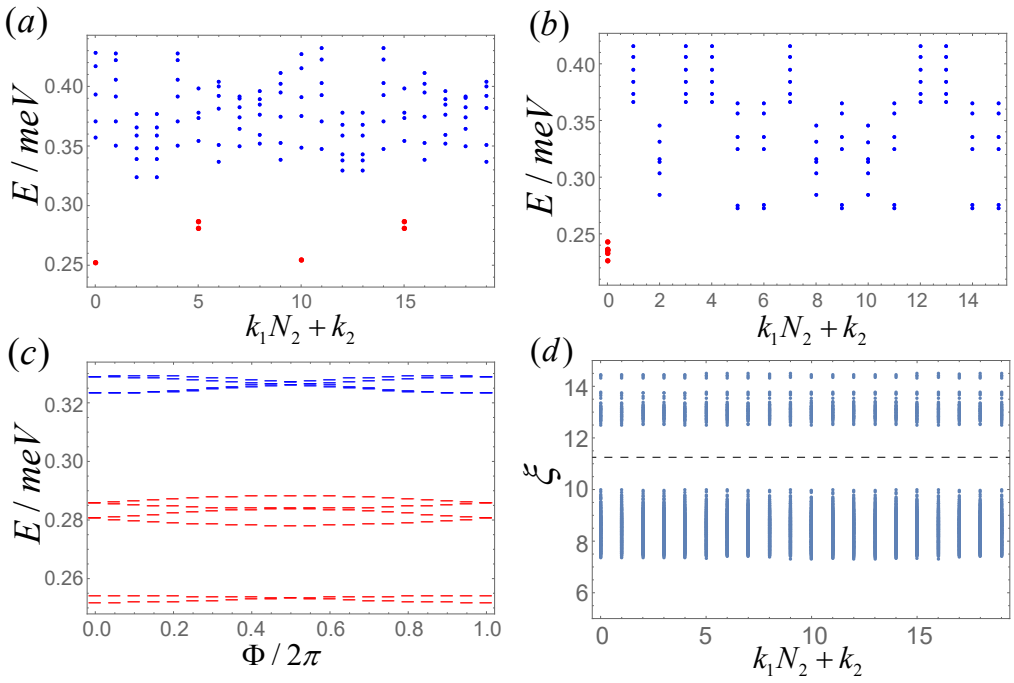

Figure 5.7: Signatures of Moore-Read states at $\theta = 1.38°$ with finite three-body interaction and vanishing two-body interaction. We choose $k_s a_M = 7$, and the three-body interaction strength when three particles are mutually separated by a_M is 0.003 meV. (a): Energy spectrum for 4×5 systems with 10 particles. The six ground states (labeled in red) are valley polarized and separated from excited states by a gap. (b): Energy spectrum for 4×4 systems with 8 particles. (c): The spectral flow for (a) under flux insertion along k_1 direction. The six ground states labeled in red are separated from excited states by a spectral gap. (d): Particle entanglement spectrum for (a) with $N_A = 4$. There are 3965 states below the entanglement gap, consistent with the counting via generalized Pauli exclusion rules.

port, optical measurements etc, and its topological nature can be accessed by Hall conductivity measurement. Due to the strong analogy between FCI and chiral spin liquids, it is plausible that Moiré superlattices may also help realize/stabilize exotic spin liquid phases [161, 162, 163] by unitizing the valley/layer pseudospin or real spin degrees of freedom.

CHAPTER VI

Summary

In this thesis, I explored different aspects of topological states of matter, especially the interplay between symmetry and topology. Comparing with the existing topological diagnosis scheme using symmetry representations [7, 10], I mainly focus on the scenarios where the symmetry representations themselves are not sufficient to determine the topological index.

This thesis is organized to cover the major aspects of my research, as well as an introduction for the non-experts to step into the field of topological phases. Chapter I started from the basic formulation of symmetry operators in tight-binding models, and then I introduced the concept of topology based on adiabatic deformation and gave some examples of topological indices, such as the Chern number and the FKM Z_2 topological index.

In Chapter II, by constructing a gauge-invariant quantity g defined on arbitrary curves in the Brillouin zone, we illustrated how the symmetry operator can be utilized to simplify the topological diagnosis even when the symmetry representations are not sufficient to determine the index. This method can be applied to systems with twofold rotation symmetry or mirror symmetry.

In Chapter III, we generalized the famous Pfaffian formula to higher-order topological insulators, which allows many important conclusions on first-order Z_2 topological

insulators to be generalized to higher-order topological insulators. This generalization is made possible by defining a superposition of symmetry operators Θ. It provides a gauge-independent way to compute the magneto-electric polarization P_3 or the effective axion field for a 3D insulator from a 2D subspace in the Brillouin zone.

In Chapter IV, we studied topological nodal line semimetals with nontrivial monopole charge in the presence of time-reversal, space-inversion and rotational symmetries. We systematically classified the appearance of different types of nodal lines based on the rotational symmetry, and we found that the interplay between time-reversal and crystalline symmetries gives rise to novel cage-like nodal structures beyond the description of Z_2 monopole charge.

In chapter V, we proposed to realize the long-sought fractional Chern insulator (FCI) states in the Moire superlattices formed by twisted homobilayer transition metal dichalcogenides. Utilizing realistic material parameters and the method of exact diagonalization, we find that at certain twisting angles and fractional filling, gapped fractional topological states, i.e., fractional Chern insulators, are naturally stabilized by simply introducing the Coulomb repulsion. This shows the Moire superlattices may be a plausible platform to realize the FCI phase with intrinsic topological order.

APPENDICES

APPENDIX A

Appendix for Gauge-invariant Line Quantity $g(\widetilde{k_a k_b})$ in Topological Insulators

A.1 Properties of $g(\widetilde{k_a k_b})$

Here we prove some equalities involving $g(\widetilde{k_a k_b})$ defined in Eq.(2.9). First we investigate the case when k_a and k_b are infinitely close to each other, denoted as k_1 and k_2. In this case we have $g(k_1, k_2) = \frac{\mathrm{Pf}[M(k_2)]}{\mathrm{Pf}[M(k_1)]} \det[W(k_1, k_2)]$ and $W(k_1, k_2)$ reduces to the overlap between the wave functions at k_1 and k_2: $W_{mn}(k_1, k_2) = \langle u_m(k_1)|u_n(k_2)\rangle$. $g(k_1, k_2)$ is invariant under gauge transformation $|u_m(k)\rangle \to U_{nm}(k)|u_n(k)\rangle$. Since under this transformation, $M_{mn}(k) = \langle u_m(k)|T|u_n(k)\rangle \to (U(k)^\dagger M(k) U(k)^*)_{mn}$, $W_{mn}(k_1, k_2) = \langle u_m(k_1)|u_n(k_2)\rangle \to (U(k_1)^\dagger W(k_1, k_2) U(k_2))_{mn}$, therefore

$$\begin{aligned} \mathrm{Pf}[M(k)] &\to \mathrm{Pf}[M(k)] \det[U(k)]^* \\ \det[W(k_1, k_2)] &\to \det[W(k_1, k_2)] \det[U(k_1)]^* \det[U(k_2)] \\ g(k_1, k_2) &= \frac{\mathrm{Pf}[M(k_2)]}{\mathrm{Pf}[M(k_1)]} \det[W(k_1, k_2)] \to g(k_1, k_2) \end{aligned} \tag{A.1}$$

This completes the proof that $g(k_1, k_2)$ is gauge-invariant. For a general path $\widetilde{k_a k_b}$, divide the path by small segments (k_i, k_{i+1}) and by definition in Eq.(2.9), $g(\widetilde{k_a k_b}) = \prod_i g(k_i, k_{i+1})$. For each small segment $g(k_i, k_{i+1})$ is gauge-invariant, therefore $g(\widetilde{k_a k_b})$ is gauge-invariant as well.

Next we prove Eq.(2.20). Suppose the system has an anti-unitary symmetry C such that it commutes with T and it is independent of k, define the sewing matrix of C as

$$R_{mn}(k) = \langle u_m(Ck)|C|u_n(k)\rangle, \tag{A.2}$$

Insert identity $\mathbf{1} = P_{occ}(k) + P_{unocc}(k) = \sum_{i\in occ} |u_i(k)\rangle\langle u_i(k)| + \sum_{i\in unocc} |u_i(k)\rangle\langle u_i(k)|$ to each $\mathbf{1}$ in the identity below:

$$\langle u_m(Ck)|T|u_n(Ck)\rangle = \langle u_m(Ck)|C\mathbf{1}T\mathbf{1}C^{-1}|u_n(Ck)\rangle, \tag{A.3}$$

where P_{occ} and P_{unocc} are projection to occupied and unoccupied bands respectively, m and n belong to occupied bands. Since $\langle u_m(Ck)|CP_{unocc}(k) = 0$, we can omit P_{unocc} in the insertion and get

$$\langle u_m(Ck)|T|u_n(Ck)\rangle = \sum_{i,j\in occ} \langle u_m(Ck)|C|u_i(k)\rangle\langle u_i(k)|T|u_j(k)\rangle^*\langle u_j(k)|C^{-1}|u_n(Ck)\rangle, \tag{A.4}$$

where the conjugation is due to the fact that T and C are anti-unitary. Notice that $\langle u_j(k)|C^{-1}|u_n(Ck)\rangle = \langle u_n(Ck)|C|u_j(k)\rangle$, the above equation implies

$$\begin{aligned} M(Ck) &= R(k)M(k)^*R(k)^T \\ \mathrm{Pf}[M(Ck)] &= \det[R(k)]\,\mathrm{Pf}[M(k)]^* \end{aligned} \tag{A.5}$$

To prove Eq.(2.20) we still need to compute $W(Ck_1, Ck_2)$. Using $|u_m(Ck)\rangle = R^\dagger_{nm}(k)$

$C|u_n(k)\rangle$ we get

$$\begin{aligned} W_{ij}(Ck_1, Ck_2) &= R_{in}(k_1)\langle Cu_n(k_1)|Cu_m(k_2)\rangle R^\dagger_{mj}(k_2)\rangle \\ &= R_{in}(k_1)\langle u_n(k_1)|u_m(k_2)\rangle^* R^\dagger_{mj}(k_2)\rangle \\ \det[W(Ck_1, Ck_2)] &= \det[W(k_1, k_2)]^* \det[R(k_1)] \det[R(k_2)]^* \end{aligned} \tag{A.6}$$

Therefore when C is anti-unitary we have:

$$\begin{aligned} g(Ck_1, Ck_2) &= \frac{\mathrm{Pf}[M(Ck_2)]}{\mathrm{Pf}[M(Ck_1)]} \det[W(Ck_1, Ck_2)] \\ &= \frac{\mathrm{Pf}[M(k_2)]^*}{\mathrm{Pf}[M(k_1)]^*} \det[W(k_1, k_2)]^* = g(k_1, k_2)^* \end{aligned} \tag{A.7}$$

If C is unitary instead, Eq.(A.4) will be changed to

$$\langle u_m(Ck)|T|u_n(Ck)\rangle = \sum_{i,j\in occ} \langle u_m(Ck)|C|u_i(k)\rangle\langle u_i(k)|T|u_j(k)\rangle\langle u_j(k)|C^{-1}|u_n(Ck)\rangle^*, \tag{A.8}$$

Using $\langle u_j(k)|C^{-1}|u_n(Ck)\rangle^* = \langle u_n(Ck)|C|u_j(k)\rangle$ for unitary symmetry C, we have

$$\begin{aligned} M(Ck) &= R(k)M(k)R(k)^T \\ \mathrm{Pf}[M(Ck)] &= \det[R(k)]\,\mathrm{Pf}[M(k)] \end{aligned} \tag{A.9}$$

For $W(Ck_1, Ck_2)$, Eq.(A.6) will be

$$\begin{aligned} W_{ij}(Ck_1, Ck_2) &= R_{in}(k_1)\langle Cu_n(k_1)|Cu_m(k_2)\rangle R^\dagger_{mj}(k_2)\rangle \\ &= R_{in}(k_1)\langle u_n(k_1)|u_m(k_2)\rangle R^\dagger_{mj}(k_2)\rangle \\ \det[W(Ck_1, Ck_2)] &= \det[W(k_1, k_2)] \det[R(k_1)] \det[R(k_2)]^* \end{aligned} \tag{A.10}$$

Therefore if C is unitary we have:

$$\begin{aligned} g(Ck_1, Ck_2) &= \frac{\mathrm{Pf}[M(Ck_2)]}{\mathrm{Pf}[M(Ck_1)]} \det[W(Ck_1, Ck_2)] \\ &= \frac{\mathrm{Pf}[M(k_2)]}{\mathrm{Pf}[M(k_1)]} \det[W(k_1, k_2)] = g(k_1, k_2) \end{aligned} \tag{A.11}$$

A general path $\widetilde{k_a k_b}$ can be divided by small segments (k_i, k_{i+1}) so that $g(\widetilde{k_a k_b}) = \prod_i g(k_i, k_{i+1})$. Eq.(2.20) is proved by applying Eq.(A.7) or (A.11) to each segment $g(k_i, k_{i+1})$.

A.2 Triviality of TRIM that are not invariant under C_2 or mirror symmetry

In this section we give a more detailed proof of the assertion that the Z_2 index ν_{2D} in the time-reversal invariant plane passing through X, Y, T, U in Fig.(2.2)(b) and X', Y, T, U' in Fig.(2.2)(d) are trivial. These 2D planes are shown in Fig.(A.1), which are obtained from a cut in Fig.(2.2)(b) and (d) respectively. This proof utilizes the interpretation of the line quantity $g(\widetilde{k_a k_b})$ as a measure of Pfaffian in the parallel transport gauge.

In Fig.(A.1)(a) the system has a two-fold rotational symmetry C_2 perpendicular to the plane which is inherited from the 3D system. However, the C_2 rotation centers are located at the black dots that bisect two TRIM. This type of C_2 operator is different from the conventional two-fold rotation that can be realized by a 2D lattice in real space, since in that case the rotation center in the momentum space will always locate at some TRIM. If we choose the origin to be at Y and denote the components of k along G_1 and G_2 direction as k_x and k_y respectively, the C_2 operator at the midpoint of $\overline{XY}$ generates a transformation $(k_x, k_y) \to (G_1/2 - k_x, -k_y)$, and time-reversal generates $(k_x, k_y) \to (-k_x, -k_y)$. Therefore the combined operation C_2T

gives $(k_x, k_y) \to (k_x - G_1/2, k_y)$. Define $\overline{g}(\mathbf{k}) = g(\mathbf{k}, \mathbf{k} + \mathbf{G}_2/2)$ for $\mathbf{k} \in \overline{XX_2}$, then from Eq.(2.20) the C_2T symmetry requires

$$\begin{aligned} &\overline{g}(\mathbf{k}) = \overline{g}(\mathbf{k} + \mathbf{G}_1/2)^* \\ &\mathrm{Im} \log \overline{g}(\mathbf{k}) = -\mathrm{Im} \log \overline{g}(\mathbf{k} + \mathbf{G}_1/2), \ \mathbf{k} \in \overline{XX_2} \end{aligned} \tag{A.12}$$

Denote the colored region in Fig.(A.1) as τ and use the same derivation that lead to Eq.(2.19), the Z_2 index in this plane is

$$\begin{aligned} \nu_{2D} &= \frac{1}{2\pi} \mathrm{Im} \int_{X_2}^{X} d\mathbf{k} \cdot \nabla \log \overline{g}(\mathbf{k}) \\ \overline{g}(\mathbf{k}) &= g(\mathbf{k}, \mathbf{k} + \mathbf{G}_2/2) \end{aligned} \tag{A.13}$$

From Eq.(A.12), the integrand in Eq.(A.13) at $\mathbf{k}$ cancels that at $\mathbf{k} + \mathbf{G}_1/2$, which leads to $\nu_{2D} = 0$. Therefore the plane has a trivial Z_2 index due to the C_2 symmetry.

In Fig.(A.1)(b) the system has mirror planes inherited from the 3D system located at the thin vertical lines. The mirror plane to the right has the transformation $(k_x, k_y) \to (G_1/2 - k_x, k_y)$. Define $\overline{g}(\mathbf{k}) = g(\mathbf{k}, \mathbf{k} + \mathbf{G}_2/2)$ for $\mathbf{k} \in \overline{X'X_3}$, from Eq.(2.20) the mirror symmetry requires

$$\overline{g}(\mathbf{k}) = \overline{g}(\mathbf{G}_1/2 - \mathbf{k}) \tag{A.14}$$

The Z_2 index from Eq.(2.19) is

$$\nu_{2D} = \frac{1}{2\pi} \mathrm{Im} \int_{X'}^{X_3} d\mathbf{k} \cdot \nabla \log \overline{g}(\mathbf{k}) \tag{A.15}$$

Therefore Eq.(A.14) requires the integrand at $\mathbf{k}$ to cancel that at $\mathbf{G}_1/2 - \mathbf{k}$, leading to $\nu_{2D} = 0$. Therefore the Z_2 index for this 2D plane is trivial due to the mirror

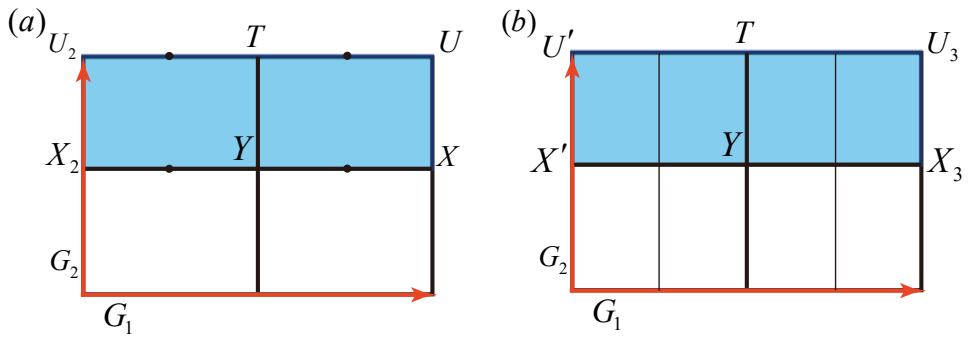

Figure A.1: The plot of time-reversal invariant planes obtained from a cut in Fig.(2.2)(b) and (d). We define the origin in these planes to be at Y. The black dots in (a) are two-fold rotation centers. The thin vertical lines in (b) are mirror planes. Note that none of these two-fold rotation centers or mirror planes pass through the origin at Y.

symmetry.

APPENDIX B

Appendix for Pfaffian Formalism for Higher-order Topological Insulators

B.1 Properties of matrices

In the main text we defined many matrices using symmetry operators. Here we prove some of their properties that are important for the proof in the main text. The definitions are:

$$B_{mn}(\mathbf{k}) = \langle u_m(C_4T\mathbf{k})|C_4T|u_n(\mathbf{k})\rangle \tag{B.1}$$

$$D_{mn}(\mathbf{k}) = \langle u_m(C_2\mathbf{k})|C_2|u_n(\mathbf{k})\rangle \tag{B.2}$$

$$M_{mn}(\mathbf{k}) = \langle u_m(\mathbf{k})|\Theta|u_n(\mathbf{k})\rangle, \quad \Theta = \frac{C_4T + C_4^{-1}T}{\sqrt{2}} \tag{B.3}$$

$$\omega_{mn}(\mathbf{k}) = \langle u_m(-\mathbf{k})|\Theta|u_n(\mathbf{k})\rangle \tag{B.4}$$

$$v_{mn}(\mathbf{k}) = \langle u_m(\mathbf{k})|S_4C_4T|u_n(\mathbf{k})\rangle \tag{B.5}$$

All of these matrices are $2N \times 2N$ where $2N$ is the number of occupied bands.

Proof of unitarity: in general if a gapped system has a symmetry P that is either unitary or antiunitary so that $PH(\mathbf{k})P^{-1} = H(P\mathbf{k})$, then $H(P\mathbf{k})P|u_n(\mathbf{k})\rangle =$

$PH(\mathbf{k})|u_n(\mathbf{k})\rangle = E_n(\mathbf{k})P|u_n(\mathbf{k})\rangle$ so that $P|u_n(\mathbf{k})\rangle$ is a superposition of eigenstate of $H(P\mathbf{k})$ with the same energy. If $|u_n(\mathbf{k})\rangle$ is in occupied bands, so should $P|u_n(\mathbf{k})\rangle$, then we have $P|u_n(\mathbf{k})\rangle = \sum_{m\in occ}|u_m(P\mathbf{k})\rangle\tilde{P}_{mn}(\mathbf{k})$ where $\tilde{P}_{mn}(\mathbf{k})$ is the coefficient for the superposition. Since $\tilde{P}_{mn}(\mathbf{k})$ is now the transformation matrix between two sets of normalized and orthogonal basis $\{P|u_n(\mathbf{k})\rangle\}$ and $\{|u_n(P\mathbf{k})\rangle\}$ that span the space of occupied bands, $\tilde{P}_{mn}(\mathbf{k}) = \langle u_m(P\mathbf{k})|P|u_n(\mathbf{k})\rangle$ is guaranteed to be unitary.

This fact shows immediately that matrices B, D and v above are unitary for every $\mathbf{k}$ as long as the system has the corresponding symmetry. $M(\mathbf{k})$ is unitary only at C_4T invariant points since $C_4T\mathbf{k} = C_4^{-1}T\mathbf{k} = \mathbf{k}$ there. $\omega(\mathbf{k})$ is unitary at straight lines $Z\overline{Z}$ and $A\overline{A}$ since $C_4T\mathbf{k} = C_4^{-1}T\mathbf{k} = -\mathbf{k}$ there.

Proof of Antisymmetry: we will show that M is antisymmetric for every $\mathbf{k}$ that is invariant under C_4, such that $C_4T\mathbf{k} = C_4^{-1}T\mathbf{k} = -\mathbf{k}$. Here are two distinct matrices related to C_4 that we want to clarify. For a N_{tot}-band system with $2N$ filled bands, the fourfold rotation can be represented by a $N_{tot} \times N_{tot}$ matrix $C_4(\mathbf{k})$ (the same as the $U_g^{\mathbf{k}}$ in Eq.(1.31)) which can have $\mathbf{k}$-dependence. This matrix is different from the $2N \times 2N$ sewing matrix $\langle u_m(C_4\mathbf{k})|C_4(\mathbf{k})|u_n(\mathbf{k})\rangle$ defined for occupied bands. The matrix $C_4(\mathbf{k})$ representing the fourfold rotation can depend on $\mathbf{k}$, and in this case $(\hat{C}_4)^4 = -1$ implies $C_4(C_4^3\mathbf{k})C_4(C_4^2\mathbf{k})C_4(C_4\mathbf{k})C_4(\mathbf{k}) = -1$. If $\mathbf{k}$ is invariant under the fourfold rotation, then this relation reduces to $(C_4(\mathbf{k}))^4 = -1$, i.e., the matrix $C_4(\mathbf{k})$ itself to the fourth power is the negative identity matrix. In this case the matrix representing the twofold rotation $C_2(\mathbf{k})$ satisfies $(C_2(\mathbf{k}))^2 = -1$. Then we can show that $\Theta^2 = T^2 = -1$. Since $(C_2)^2 = -1$, then $C_2 + C_2^{-1} = 0$ and $\Theta^2 = -(C_4 + C_4^{-1})^2/2 = -(C_2 + C_2^{-1} + 2)/2 = -1$. The anti-symmetric property of

$M(\mathbf{k})$ matrix for C_4-invariant momenta can be seen by:

$$\begin{aligned} M_{mn}(\mathbf{k}) &= \langle u_m(\mathbf{k})|\Theta|u_n(\mathbf{k})\rangle \\ &= \langle \Theta^2 u_n(\mathbf{k})|\Theta|u_m(\mathbf{k})\rangle \\ &= -\langle u_n(\mathbf{k})|\Theta|u_m(\mathbf{k})\rangle \\ &= -M_{nm}(\mathbf{k}) \end{aligned} \tag{B.6}$$

If the $N_{tot} \times N_{tot}$ matrix representing C_4 is independent of $\mathbf{k}$, then $M(\mathbf{k})$ is anti-symmetric for every $\mathbf{k}$ in the Brillouin zone.

In a similar way we can show that $v_{mn}(\mathbf{k}) = -v_{nm}(\mathbf{k})$ so that v is also antisymmetric. The same technique when applied to ω and B yields

$$\begin{aligned} \omega_{mn}(\mathbf{k}) &= -\omega_{nm}(-\mathbf{k}) \\ B_{mn}(\mathbf{k}) &= -\langle u_n(\mathbf{k})|C_4^{-1}T|u_m(C_4T\mathbf{k})\rangle \end{aligned} \tag{B.7}$$

Constrains from operator identities: consider the complete relation

$$\mathbf{1} = \sum_{i\in occ} |u_i(\mathbf{k})\rangle\langle u_i(\mathbf{k})| + \sum_{i\in uocc} |u_i(\mathbf{k})\rangle\langle u_i(\mathbf{k})|, \tag{B.8}$$

where *occ* and *uocc* refer to occupied and unoccupied bands. Since $(C_2)^2 = -1$, let $|u_m\rangle$ and $|u_n\rangle$ be in occupied bands, replace the $\mathbf{k}$ in the complete relation by $C_2\mathbf{k}$ and insert it to the $\mathbf{1}$ in identity $\langle u_m(\mathbf{k})|C_2\mathbf{1}C_2|u_n(\mathbf{k})\rangle = -\delta_{mn}$. The unoccupied part in the complete relation do not contribute since $C_2|u_n(\mathbf{k})\rangle$ belongs to the space spanned by occupied bands and have zero overlap with unoccupied bands. Therefore we get $\sum_{i\in occ} D_{mi}(C_2\mathbf{k})D_{in}(\mathbf{k}) = -\delta_{mn}$, which means

$$D(C_2\mathbf{k}) = -D^\dagger(\mathbf{k}) \tag{B.9}$$

We can also consider identity $C_2 = -(C_4T)^2$. Replace the $\mathbf{k}$ by $C_4T\mathbf{k}$ in complete relation and insert it to $\langle u_m(C_2\mathbf{k})|C_2|u_n(\mathbf{k})\rangle = -\langle u_m(C_2\mathbf{k})|C_4T\mathbf{1}C_4T|u_n(\mathbf{k})\rangle$. Note that T is antiunitary therefore a complex conjugation is needed, and we get

$$D(\mathbf{k}) = -B(C_4T\mathbf{k})B^*(\mathbf{k}) \tag{B.10}$$

Similarly for operator identity $S_4C_4T = -C_4^{-1}TS_4C_4TC_4T$, replace the $\mathbf{k}$ by $C_4T\mathbf{k}$ in complete relation and insert it to

$$\langle u_m(\mathbf{k})|S_4C_4T|u_n(\mathbf{k})\rangle = -\langle u_m(\mathbf{k})|C_4^{-1}T\mathbf{1}S_4C_4T\mathbf{1}C_4T|u_n(\mathbf{k})\rangle, \tag{B.11}$$

we get $v_{mn}(\mathbf{k}) = -\sum_{i,j\in occ}\langle u_m(\mathbf{k})|C_4^{-1}T|u_i(C_4T\mathbf{k})\rangle v^*_{ij}(C_4T\mathbf{k})B_{jn}(\mathbf{k})$. Using Eq.(B.7) we have

$$v(\mathbf{k}) = B^{\mathrm{T}}(\mathbf{k})v^*(C_4T\mathbf{k})B(\mathbf{k}) \tag{B.12}$$

$$\mathrm{Pf}[v(\mathbf{k})] = \mathrm{Pf}[v(C_4T\mathbf{k})]^* \det[B(\mathbf{k})] \tag{B.13}$$

If we replace S_4C_4T by Θ, the above derivations are still true and we will get

$$M(\mathbf{k}) = B^{\mathrm{T}}(\mathbf{k})M^*(C_4T\mathbf{k})B(\mathbf{k}) \tag{B.14}$$

$$\mathrm{Pf}[M(\mathbf{k})] = \mathrm{Pf}[M(C_4T\mathbf{k})]^* \det[B(\mathbf{k})] \tag{B.15}$$

Determinant equalities: we will show that $\det[B(\mathbf{K})] = \det[M(\mathbf{K})]$ for $\mathbf{K} \in K^4$ and $\det[B(\tilde{k})] = \det[\omega(\tilde{k})]$ for $\tilde{k}$ at straight lines $Z\overline{Z}$ and $A\overline{A}$. Since $C_4T\mathbf{K} =$

$C_4^{-1}T\mathbf{K} = \mathbf{K},\ C_4T\tilde{k} = C_4^{-1}T\tilde{k} = -\tilde{k}$, using Eq.(B.7) we get

$$\begin{aligned} M_{mn}(\mathbf{K}) &= (\langle u_m(\mathbf{K})|C_4T|u_n(\mathbf{K})\rangle + \langle u_m(\mathbf{K})|C_4^{-1}T|u_n(\mathbf{K})\rangle)/\sqrt{2} \\ &= (B(\mathbf{K}) - B^{\mathrm{T}}(\mathbf{K}))/\sqrt{2} \\ \omega_{mn}(\tilde{k}) &= (\langle u_m(-\tilde{k})|C_4T|u_n(\tilde{k})\rangle + \langle u_m(-\tilde{k})|C_4^{-1}T|u_n(\tilde{k})\rangle)/\sqrt{2} \\ &= (B(\tilde{k}) - B^{\mathrm{T}}(-\tilde{k}))/\sqrt{2} \end{aligned} \tag{B.16}$$

When there is no accidental degeneracy, we can find a gauge where $B(\mathbf{k})$ is block diagonal with each block being $B_r(\mathbf{k}) \in SU(2)$. Therefore $M(\mathbf{K})$ and $\omega(\tilde{k})$ are also block diagonal. Since $C_2\tilde{k} = \tilde{k}$, Eq.(B.9) implies each block of D is $D_r(\tilde{k}) = i\hat{n}(\tilde{k}) \cdot \sigma$. Then Eq.(B.10) gives $B_r(-\tilde{k}) = -(i\hat{n}(\tilde{k}) \cdot \sigma)B_r^{\mathrm{T}}(\tilde{k})$. Let $\hat{n}'(\tilde{k}) = (n_x, -n_y, n_z)$, Eq.(B.16) leads to

$$\begin{aligned} \omega_r(\tilde{k}) &= B_r(\tilde{k})\frac{1 + i\hat{n}'(\tilde{k}) \cdot \sigma}{\sqrt{2}} \\ \det[\omega_r(\tilde{k})] &= \det[B_r(\tilde{k})] \det\left[\frac{1 + i\hat{n}'(\tilde{k}) \cdot \sigma}{\sqrt{2}}\right] = \det[B_r(\tilde{k})] \\ \det[\omega(\tilde{k})] &= \det[B(\tilde{k})] \end{aligned} \tag{B.17}$$

Now we have proved the $\det[\omega(\tilde{k})] = \det[B(\tilde{k})]$ for the gauge in which $\det[B] = 1$. But since $\det[B(\tilde{k})]$ and $\det[\omega(\tilde{k})]$ change in the same way under gauge transformation, they should be equal in any gauge. At C_4T invariant due to $\omega(\mathbf{K}) = M(\mathbf{K})$, we also have $\det[B(\mathbf{K})] = \det[M(\mathbf{K})]$.

B.2 Properties of the degree of map

We consider a general smooth map $G : T^3 \to SU(2)$. The degree of this map is

$$\deg[G] = -\frac{1}{24\pi^2}\int \mathrm{d}^3\mathbf{k}\epsilon^{ijk}\,\mathrm{Tr}\left[\left(G\partial_iG^\dagger\right)\left(G\partial_jG^\dagger\right)\left(G\partial_kG^\dagger\right)\right] \tag{B.18}$$

One can show that the degree is quantized to integer and thus invariant for small perturbation of the map [48]. The degree is addictive, which means if there is another map $G' : T^3 \to SU(2)$, then

$$\deg[GG'] = \deg[G] + \deg[G'] \tag{B.19}$$

Therefore $G^{-1} = G^\dagger$ always has the opposite degree to G since their product is constant. Taking a complex conjugation to Eq.(B.18) we get the degree of G^*. Since $\deg[G]$ is real, this means G^* has the same degree as G. Combining these facts we get

$$\deg[G^\dagger] = -\deg[G], \quad \deg[G^*] = \deg[G], \quad \deg[G^{\mathrm{T}}] = -\deg[G] \tag{B.20}$$

If we perform a rotation or rotoinversion in the $\mathbf{k}$ space T^3 given by $s : T^3 \to T^3$ so that $s\mathbf{k} = \mathbf{k}'$, the degree of the transformed map $G \circ s$ can be obtained by a change of variable in Eq.(B.18). During the change of variable the volume element $\mathrm{d}^3\mathbf{k}$ will bring a factor of $|\det\left[\frac{\partial(k_x,k_y,k_z)}{\partial(k'_x,k'_y,k'_z)}\right]|$ and the partial derivatives will introduce a factor of $\det\left[\frac{\partial(k'_x,k'_y,k'_z)}{\partial(k_x,k_y,k_z)}\right]$, therefore the overall effect is to introduce a factor of $\mathrm{sign}\left(\det\left[\frac{\partial(k'_x,k'_y,k'_z)}{\partial(k_x,k_y,k_z)}\right]\right)$, which leads to

$$\begin{aligned}
& \deg[G \circ s] \\
= \; & -\frac{1}{24\pi^2}\int \mathrm{d}^3\mathbf{k}\epsilon^{ijk}\,\mathrm{Tr}\left[\left(G(s\mathbf{k})\partial_i G(s\mathbf{k})^\dagger\right)\left(G(s\mathbf{k})\partial_j G(s\mathbf{k})^\dagger\right)\left(G(s\mathbf{k})\partial_k G(s\mathbf{k})^\dagger\right)\right] \\
= \; & \mathrm{sign}\left(\det\left[\frac{\partial(k'_x,k'_y,k'_z)}{\partial(k_x,k_y,k_z)}\right]\right)\deg[G]
\end{aligned} \tag{B.21}$$

In particular if the transformation s is C_4T so that $\mathbf{k}' = (k_y, -k_x, -k_z)$, then we get $\det\left[\frac{\partial(k'_x,k'_y,k'_z)}{\partial(k_x,k_y,k_z)}\right] = -1$. Therefore

$$\deg[G(C_4T\mathbf{k})] = -\deg[G(\mathbf{k})] \tag{B.22}$$

APPENDIX C

Appendix for Topological Nodal Line Semimetals

C.1 Definition of the Γ matrices

In this section we write down the explicit form of Γ matrices that we adopted. This set of matrices is not unique, and is sensitive to the choice of bases. For our convenience, we will use the following basis.

$$\begin{aligned}
\Gamma_1 =& \tau_z \otimes \sigma_0, \\
\Gamma_2 =& \tau_x \otimes \sigma_z, \\
\Gamma_3 =& \tau_x \otimes \sigma_x, \\
\Gamma_4 =& \tau_x \otimes \sigma_y, \\
\Gamma_5 =& \Gamma_1\Gamma_2\Gamma_3\Gamma_4 = -\tau_y \otimes \sigma_0,
\end{aligned} \tag{C.1}$$

Here τ_i and σ_i with $i = 0, x, y, z$ are the 2×2 identity and Pauli matrices where

$$\begin{aligned}
\tau_0 =&\sigma_0 = \begin{pmatrix} 1 & 0 \\ 0 & 1 \end{pmatrix}, \ \tau_x = \sigma_x = \begin{pmatrix} 0 & 1 \\ 1 & 0 \end{pmatrix}, \\
\tau_y =&\sigma_y = \begin{pmatrix} 0 & -i \\ i & 0 \end{pmatrix}, \ \tau_z = \sigma_z = \begin{pmatrix} 1 & 0 \\ 0 & -1 \end{pmatrix}
\end{aligned} \tag{C.2}$$

In the dual basis, we have

$$\begin{aligned}
\tilde{\Gamma}_1 =&\tau_z \otimes \sigma_0, \\
\tilde{\Gamma}_2 =&\Sigma_{14} = -\tau_y \otimes \sigma_y, \\
\tilde{\Gamma}_3 =&i\Gamma_2\Gamma_3\Gamma_4 = -\tau_x \otimes \sigma_0, \\
\tilde{\Gamma}_4 =&-\Sigma_{12} = \tau_y \otimes \sigma_z, \\
\tilde{\Gamma}_5 =&\tau_y \otimes \sigma_x
\end{aligned} \tag{C.3}$$

In both these two bases, $TI = K$ with K being the complex conjugation, although the explicit form of T and I are model-dependent and not universal.

C.2 Reduced Hamiltonian

Here we consider a four-band model as discussed in the main text, and prove that they can be reduced to Hamiltonian H_1 or H_2.

First, we start from a generic four-band model without assuming the time-reversal or space-inversion symmetry. As shown in the main text, we can write the Hamiltonian in terms of the sixteen matrices that we choose, which are Γ matrices and their products.

$$H = a\Gamma_1 + b_1\Gamma_2 + b_2\Gamma_3 + c_1\Sigma_{14} + c_2 i\Gamma_2\Gamma_3\Gamma_4 + \ldots \tag{C.4}$$

where a, b_1, b_2, ... are real functions of the momentum $\mathbf{k}$. For a system made of four orbitals, where two bands constructed by the first two orbitals are inverted with the other two bands constructed by the last two orbitals, one of these 16-matrices is special and we choose it to be the Γ_1 matrix

$$\Gamma_1 = \begin{pmatrix} +1 & 0 & 0 & 0 \\ 0 & +1 & 0 & 0 \\ 0 & 0 & -1 & 0 \\ 0 & 0 & 0 & -1 \end{pmatrix} \tag{C.5}$$

This matrix marks the band inversion. If we turn off all other terms, when the coefficient of this matrix [i.e. a in Eq. (C.4)] is positive (negative) the first two orbits have positive (negative) energy. Thus, the double band inversion that we consider in the manuscript is represented by the change of sign in the coefficient a. For a small band inversion at Γ, a is positive near the Γ point, and it changes sign as we move away from Γ. These two regions (with $a > 0$ and $a < 0$ respectively) are separated by a 2D manifold, on which $a = 0$. For a small band inversion at Γ, this 2D manifold has the topology of a sphere.

The eigenvalues of a Hamiltonian can be computed via the eigen-equation. $\det(H - \epsilon I) = 0$. For a four-band model, this equation is a fourth-order equation of ϵ. Because the absolute value of energy plays little role in topology, we can make the Hamiltonian traceless by deducting its trace part, without changing any topological features. For a traceless Hamiltonian, the eigen-equation must take the following structure

$$\epsilon^4 + q\epsilon^2 + r\epsilon + s = 0 \tag{C.6}$$

where q, r and s depend on the 16 coefficients in Eq. (C.4). Here, the ϵ^3 term is absent, because its coefficient is the trace of H, which we set to zero.

For a system with two conduction and two valence bands, we can always make the two conduction bands degenerate, and same can be done to the valence bands. As long as we don't introducing new band crossings in this procedure, the topological information remains. For nodal lines with nontrivial monopole charge, this procedure shrinks a nodal line into a nodal point with four-fold degeneracy.

After this procedure, our fourth-order eigen-equation has two set of degenerate solutions, i.e. two conduction bands with identical eigen-energy $+\epsilon$ and two valence bands with $-\epsilon$. In other words, our eigen-equation shall have two pairs of equal real roots. For a quartic equation shown above, this requires the following conditions: (a) the discriminant is zero

$$\Delta = 16q^4s - 4q^3r^2 - 128q^2s^2 + 144qr^2s - 27r^4 + 256s^3 = 0 \tag{C.7}$$

and (b) $q < 0$ and (c) $q^2 = 4s$. For a generic fourth order equation, these three conditions are independent. However, as an eigen-equation of a Hermitian matrix, the last condition (c) is sufficient to guarantee (a) and (b). This is because for an Hermitian matrix, all roots of the eigen-equation have to be real, and this constraint makes (c) sufficient to ensure the other two.

In general, the condition $q^2 = 4s$ here is a very complicated equation. In terms of the 16 coefficients in Eq. (C.4), this equation is a quartic equation for those coefficients and it involves nearly 200 terms. However, luckily, such a complicated equation can be simplified in the form shown in Eq. (C.9), i.e., the sum of 15 squares equals to 0. Because all the coefficients of Eq. (C.4) are real, sum of squares being zero means that every single square needs to be zero, which gives us 15 quadratic equations [Eq. (C.10)-(C.24)]. These 15 equations are not independent. For the problem that we considers in the manuscript, due to the time-reversal and space-inversion symmetry, the Hamiltonian can be made real [i.e. $b_1' = b_2' = c_1' = c_2' = e' = f' = 0$ in Eq.(C.8)].

For such a real Hamiltonian, it turns out that if we assume that conduction and valance bands are both degenerate and H is traceless (i.e. $q^2 = 4s$), these 15 equations allow us to have 5 free parameters in Eq. (C.4), which are the 5 terms that we shown in this equation. The rest of coefficients can all be computed from these 15 equations and thus they are not independent parameters anymore. This is the reason why we selected to show these 5 terms in our Hamiltonian.

Furthermore, we can further reduce the number of free parameters here by 2, by turning off either $b_{1/2}$ or $c_{1/2}$. For a double-band inversion that we consider here in most part of the k-space, we have $a \neq 0$, and it it is easy to check that here we can turn off all other coefficients in H, and the system will remain gapped and non-singular. On the other hand, for the 2D manifold with $a = 0$, only two options are available: (a) $b_1^2 + b_2^2 \neq 0$ while all other matrices have zero coefficients or (b) $c_1^2 + c_2^2 \neq 0$ while all other matrices have zero coefficients. Except for these two options, the 15 equations we mentioned above will tell us that certain coefficients must diverge, due to terms like c_1/a.

In summary, when we make the two conduction and two valence bands into degenerate pairs (without introducing new band crossings between conduction and valence bands), we can turn off any terms except for $a\Gamma_1$ in our Hamiltonian as long as $a \neq 0$. If $a = 0$, we have to choose from the two options shown above. As a result, for a Γ point band inversion, if the $a = 0$ manifold follows the option (a), we can turn off all other terms except for a, b_1 and b_2 in the whole k-space without introducing any singularity or gap closing. On the other hand, if the $a = 0$ manifold follows option (b), then we can turn off all terms except for a, c_1 and c_2.

In either case, by making the conduction/valance bands degenerate, we can turn off almost all the terms in Eq. (C.4) and only keep three of them, which are H_1 or H_2.

C.3 Conditions for band degeneracy

Consider a generic 4×4 tracless Hermitian Hamiltonian H with matrix elements:

$$\begin{aligned} H_{11} &= a + d_1,\ H_{22} = a - d_1,\ H_{33} = -a + d_2,\ H_{44} = -a - d_2, \\ H_{12} &= e + e'i + f + f'i,\ H_{13} = -(c_2 + ic_2') + b_1 + b_1'i, \\ H_{14} &= b_2 + b_2'i + c_1 + c_1'i, H_{23} = b_2 + b_2'i - (c_1 + c_1'i), \\ H_{24} &= -(c_2 + ic_2') - (b_1 + ib_1'),\ H_{34} = e + e'i - (f + f'i) \end{aligned} \tag{C.8}$$

Here i is the imaginary number unit and the other letters represent generic real numbers. The condition for degenerate bands $q^2 = 4s$ can be written as

$$0 = q^2/4 - s = \sum_{i=1}^{15} \Delta_i^2 \tag{C.9}$$

where

$$\Delta_1 = a(d_1 - d_2) - 2(b_1 c_2 + b_1' c_2') \tag{C.10}$$

$$\Delta_2 = a(d_1 + d_2) + 2(b_2 c_1 + b_2' c_1') \tag{C.11}$$

$$\Delta_3 = 2(c_2' c_1 - c_1' c_2 + a f') \tag{C.12}$$

$$\Delta_4 = 2(-b_1 c_1 - b_1' c_1' + a e) \tag{C.13}$$

$$\Delta_5 = 2(-b_2 c_2 - b_2' c_2' + a f) \tag{C.14}$$

$$\Delta_6 = 2(b_2 b_1' - b_2' b_1 + a e') \tag{C.15}$$

$$\Delta_7 = -2e' c_2' + 2f b_1 - b_2(d_1 - d_2) \tag{C.16}$$

$$\Delta_8 = -2e' c_2 - 2f b_1' + b_2'(d_1 - d_2) \tag{C.17}$$

$$\Delta_9 = -2e c_2 + 2f' b_1' + c_1(d_1 - d_2) \tag{C.18}$$

$$\Delta_{10} = -2e c_2' - 2f' b_1 + c_1'(d_1 - d_2) \tag{C.19}$$

$$\Delta_{11} = 2e b_2' - 2e' c_1 + b_1'(d_1 + d_2) \tag{C.20}$$

$$\Delta_{12} = 2e b_2 + 2e' c_1' + b_1(d_1 + d_2) \tag{C.21}$$

$$\Delta_{13} = -2f c_1 - 2f' b_2' - c_2(d_1 + d_2) \tag{C.22}$$

$$\Delta_{14} = -2f c_1' + 2f' b_2 - c_2'(d_1 + d_2) \tag{C.23}$$

$$\Delta_{15} = 2ef + 2e' f' + (d_1^2 - d_2^2)/2 \tag{C.24}$$

Because all the terms here are real, the sum of squares equals to zero implies $\Delta_i = 0$ for any i.

C.4 lattice models

In this section, we show the lattice models that we used to generate the figures of nodal-lines in Fig. 4.4. First we define some functions for representations in different

point groups for future convenience:

$$
\begin{aligned}
C_{3i}: \quad \Gamma_1^+: \quad f_1 &= \cos k_1 + \cos k_2 + \cos k_3 \\
\Gamma_1^+: \quad f_2 &= \cos k_1' + \cos k_2' + \cos k_3', \\
\Gamma_2^-: \quad f_3 &= \sin(k_1 + k_z) + \ w^2 \sin(k_3 + k_z) \ - w \sin(-k_2 + k_z) \\
\Gamma_2^-: \quad f_4 &= \sin(k_1' + k_z) + \ w^2 \sin(k_3' + k_z) \ - w \sin(-k_2' + k_z) \\
\Gamma_1^-: \quad f_5 &= \sin(k_1 + k_z) + \ \sin(k_3 + k_z) + \sin(-k_2 + k_z) \\
\Gamma_1^-: \quad f_6 &= \sin(k_1' + k_z) + \ \sin(k_3' + k_z) + \ \sin(-k_2' + k_z) \\
C_{6h}: \quad \Gamma_2^-: \quad f_7 &= (\cos k_1 - w_6^2 \cos k_2 + w_6^4 \cos k_3) \sin k_z \\
\Gamma_4^-: \quad f_8 &= \sin k_1 - \sin k_2 + \sin k_3 \\
\Gamma_4^-: \quad f_9 &= \sin k_1' - \sin k_2' + \sin k_3' \\
\Gamma_4^+: \quad f_{10} &= (\sin k_1 - \sin k_2 + \sin k_3) \sin k_z \\
\Gamma_5^-: \quad f_{11} &= \sin k_1 + w_6^2 \sin k_2 + w_6^4 \sin k_3
\end{aligned}
\tag{C.25}
$$

$$
\begin{aligned}
k_1 &= k_x, \ k_2 = \frac{1}{2} k_x + \frac{\sqrt{3}}{2} k_y, \ k_3 = -\frac{1}{2} k_x + \frac{\sqrt{3}}{2} k_y \\
k_1' &= \frac{3}{2} k_x + \frac{\sqrt{3}}{2} k_y, \ k_2' = \sqrt{3} k_y, \ k_3' = -\frac{3}{2} k_x + \frac{\sqrt{3}}{2} k_y \\
w &= e^{\frac{i\pi}{3}}, \quad w_6 = e^{\frac{i\pi}{6}}
\end{aligned}
\tag{C.26}
$$

Here the functions defined with $k_{1,2,3}$ are for nearest-neighbour hoppings, and the functions with $k'_{1,2,3}$ are for next-nearest neighbour hoppings.

C.4.1 Family 1, C_i and C_{3i}

For systems with C_i (C_{3i}) symmetry, we consider a triclinic (hexagonal) lattice with four orbits per site and the symmetry of these four orbits are Γ_1^+, Γ_1^+, Γ_1^- and Γ_1^-. Using these four orbits as the basis for our Hamiltonian, we have $T = K$ and

$I = \tau_z \otimes \sigma_0$ and the Hamiltonian is

$$H = a\ \tau_z \otimes \sigma_0 + b_1\ \tau_y \otimes \sigma_z + b_2\ \tau_y \otimes \sigma_x - c_1\ \tau_x \otimes \sigma_y \tag{C.27}$$

For the system with the C_i symmetry shown in Fig. 4.4, the parameters are:

$$\begin{aligned} a &= 1.5(\cos k_x + 1.2\cos k_y) + 1.5\cos k_z - 2.5 \\ b_1 &= \sin k_y + 0.5\sin k_z \\ b_2 &= \sin k_x - \sin k_y \\ c_1 &= 0.3(\sin k_z + 0.5\sin k_y) \end{aligned} \tag{C.28}$$

Here, only nearest-neighbor hoppings are needed, and the longer-range hoppings are set to zero.

The parameters for the C_{3i} system are:

$$\begin{aligned} a &= f_1 + f_2 + 4\cos k_z - 6 \\ b_1 &= 0.2 f_6 \\ b_2 &= 0.4 f_5 \\ c_1 &= 0.7\sin k_z \end{aligned} \tag{C.29}$$

where f_2 and f_6 are from next-nearest neighbor hoppings and all others are from nearest neighbor hoppings.

C.4.2 Family 4, $C_{2h},\ C_{4h},\ C_{6h}$

Here, same as before, we put four orbits on each lattice site with symmetry Γ_1^+, Γ_2^+, Γ_1^- and Γ_2^- for C_{2h} and C_{4h}, and Γ_1^+, Γ_4^+, Γ_1^-, Γ_4^- for C_{6h}. Using these four orbits as the basis for our Hamiltonian, we have $T = K$, $P = \tau_z \otimes \sigma_0$. The two-fold rotation

is $C_2 = \tau_0 \otimes \sigma_z$ for C_{2h}, while the four-fold rotation is $C_4 = \tau_0 \otimes \sigma_z$ for C_{4h} and $C_6 = \tau_0 \otimes \sigma_z$ for C_{6h}.

The Hamiltonian is

$$H = a\ \tau_0 \otimes \sigma_z + b_1\ \tau_0 \otimes \sigma_x - b_2\ \tau_x \otimes \sigma_y + g\ \tau_z \otimes\ \sigma_0 \tag{C.30}$$

The parameters for a system with C_{2h} symmetry are

$$\begin{aligned} a &= \cos_x + \cos k_y + 1.5 \cos k_z - 2 \\ b_1 &= \sin k_x \sin k_z \\ b_2 &= \sin k_y \\ g &= 0.3 \end{aligned} \tag{C.31}$$

Here, only nearest-neighbor hoppings are needed, and the longer-range hoppings are set to zero.

The parameters for the nodal lines in C_{4h} are:

$$\begin{aligned} a &= \cos_x + \cos k_y + 1.5 \cos k_z - 2 \\ b_1 &= \cos k_x - \cos k_y \\ b_2 &= \sin k_z(\cos(k_x + k_y) - \cos(k_x - k_y)) \\ g &= 0.2 \end{aligned} \tag{C.32}$$

The b_2 above is from next-nearest neighbor hopping while all the other terms are from nearest neighbor hopping.

The parameters for the nodal lines in C_{6h} are:

$$\begin{aligned} a &= f_1 + f_2 + 4\cos k_z - 6 \\ b_1 &= 5f_{10} \\ b_2 &= f_9 \\ g &= 0.4 \end{aligned} \tag{C.33}$$

where f_2 and f_9 are from next-nearest neighbor hoppings and all other terms are from nearest neighbor hoppings.

C.4.3 Family 5, C_{3i}

Here, we put four orbits with symmetry Γ_2^+, Γ_3^+, Γ_2^-, Γ_3^- on each lattice site, and use these four orbits as the basis of the Hamiltonian. As a result, we have $T = \tau_0 \otimes \sigma_x K$, $P = \tau_z \otimes \sigma_0$. Rotation operators are given by the representations $C_3 = \mathrm{diag}(\omega^2, -\omega, \omega^2, -\omega)$, where $\omega = e^{i\frac{\pi}{3}}$ and diag refers to a diagonal matrix. The Hamiltonian for the nodal lines is:

$$\begin{aligned} H &= a\ \tau_z \otimes \sigma_0 + b_1\ \tau_y \otimes \sigma_y + b_2\ \tau_y \otimes \sigma_x + c_1\ \tau_x \otimes \sigma_z + c_2\ \tau_y \otimes \sigma_0 \\ a &= f_1 + 0.3f_2 + 4\cos k_z - 4 \\ b_1 + ib_2 &= (1 - g_0)(0.5f_3 + 0.3f_4) \\ c_1 &= 0.4g_0 f_5 \\ c_2 &= 0.2g_0 f_6 \end{aligned} \tag{C.34}$$

The figure with $Q_1 = 1$ has $g_0 = 0.4$ and the one with $Q_2 = 3$ has $g_0 = 0.8$. The terms f_2, f_4 and f_6 are from next-nearest neighbor hoppings and the rests are from nearest neighbor.

C.4.4 Family 5, C_{4h}

Here, the four orbits have symmetry Γ_3^+, Γ_4^+, Γ_3^-, Γ_4^- and thus $C_4 = \mathrm{diag}(i, -i, i, -i)$, $T = \tau_0 \otimes \sigma_x K$, and $P = \tau_z \otimes \sigma_0$. The Hamiltonian is

$$\begin{aligned} H &= a\ \tau_z \otimes \sigma_0 + b_1\ \tau_y \otimes \sigma_y + b_2\ \tau_y \otimes \sigma_x + c_1\ \tau_x \otimes \sigma_z \\ a &= \cos k_x + \cos k_y + 1.5 \cos k_z - 2 \\ b_1 &= (1 - g_0)\left(\sin k_z(\cos k_x - \cos k_y) + 0.2 \sin k_z(\cos(k_x + k_y) - \cos(k_x - k_y))\right) \\ b_2 &= (1 - g_0)\left(0.2 \sin k_z(\cos k_x - \cos k_y) + \sin k_z(\cos(k_x + k_y) - \cos(k_x - k_y))\right) \\ c_1 &= g_0 \sin k_z \end{aligned} \tag{C.35}$$

The figure with $Q_1 = 2$ has $g_0 = 0.25$ and the one with $Q_2 = 0$ has $g_0 = 0.7$. As g_0 becomes larger, the two nodal lines with nontrivial monopole charge move towards the $k_z = 0$ plane and annihilate with each other. Terms proportional to $(\cos k_x - \cos k_y)$ are from nearest neighbor hoppings and those proportional to $(\cos(k_x + k_y) - \cos(k_x - k_y))$ are from next-nearest neighbor hoppings.

C.4.5 Family 5, C_{6h}

Here, the four orbits have symmetry Γ_2^+, Γ_3^+, Γ_2^-, Γ_3^-, and $C_6 = \mathrm{diag}(-w_6^2, w_6^4, -w_6^2, w_6^4)$ with $w_6 = e^{\frac{i\pi}{6}}$. $T = \tau_0 \otimes \sigma_x K$, $P = \tau_z \otimes \sigma_0$. The Hamiltonian is

$$\begin{aligned} H &= a\ \tau_z \otimes \sigma_0 + b_1\ \tau_y \otimes \sigma_y + b_2\ \tau_y \otimes \sigma_x + c_1\ \tau_x \otimes \sigma_z \\ a &= f_1 + f_2 + 4 \cos k_z - 6 \\ b_1 + i b_2 &= (1 - g_0) f_7 \\ c_1 &= g_0 \sin k_z \end{aligned} \tag{C.36}$$

where f_2 is from next-nearest neighbor hopping and all other terms are from nearest neighbor hoppings. The figure with $Q_1 = 2$ has $g_0 = 0.04$ and the one with $Q_2 = 0$

has $g_0 = 0.6$. The two extra-robust nodal lines annihilate as g_0 grows.

C.4.6 Family 6, C_{6h}

Here, the four orbits have symmetry Γ_2^+, Γ_3^+, Γ_5^-, Γ_6^-. $C_6 = \mathrm{diag}(-w_6^2, w_6^4, w_6^2, -w_6^4)$. The Hamiltonian is:

$$\begin{aligned} H &= a\ \tau_z \otimes \sigma_0 + b_1\ \tau_y \otimes \sigma_y + b_2\ \tau_y \otimes \sigma_x + c_1\ \tau_x \otimes \sigma_z + c_2\ \tau_y \otimes \sigma_0, \\ a &= f_1 + f_2 + 4\cos k_z - 6 \\ b_1 + ib_2 &= (1 - g_0) f_{11} \\ c_1 &= g_0 f_8 \\ c_2 &= g_0 f_9 \end{aligned} \tag{C.37}$$

Here, f_2 and f_9 are from next-nearest neighbor hoppings, while all other terms are from nearest neighbor hoppings. The figure with $Q_1 = 3$ has $g_0 = 0.9$ and the one with $Q_2 = 1$ has $g_0 = 0.5$.

BIBLIOGRAPHY

BIBLIOGRAPHY

[1] Per-Olov Löwdin. On the non-orthogonality problem connected with the use of atomic wave functions in the theory of molecules and crystals. *The Journal of Chemical Physics*, 18(3):365–375, 1950.

[2] A. Alexandradinata, Xi Dai, and B. Andrei Bernevig. Wilson-loop characterization of inversion-symmetric topological insulators. *Phys. Rev. B*, 89:155114, Apr 2014.

[3] Andreas W W Ludwig. Topological phases: classification of topological insulators and superconductors of non-interacting fermions, and beyond. *Physica Scripta*, T168:014001, dec 2015.

[4] Zhijun Wang, A. Alexandradinata, R. J. Cava, and B. Andrei Bernevig. Hourglass fermions. *Nature*, 532(7598):189–194, Apr 2016.

[5] Gregory H. Wannier. The structure of electronic excitation levels in insulating crystals. *Phys. Rev.*, 52:191–197, Aug 1937.

[6] Nicola Marzari, Arash A. Mostofi, Jonathan R. Yates, Ivo Souza, and David Vanderbilt. Maximally localized wannier functions: Theory and applications. *Rev. Mod. Phys.*, 84:1419–1475, Oct 2012.

[7] Barry Bradlyn, L. Elcoro, Jennifer Cano, M. G. Vergniory, Zhijun Wang, C. Felser, M. I. Aroyo, and B. Andrei Bernevig. Topological quantum chemistry. *Nature*, 547:298 EP –, Jul 2017.

[8] Wladimir A. Benalcazar, Tianhe Li, and Taylor L. Hughes. Quantization of fractional corner charge in C_n-symmetric higher-order topological crystalline insulators. *Phys. Rev. B*, 99:245151, Jun 2019.

[9] Adrien Bouhon, Tomá š Bzdušek, and Robert-Jan Slager. Geometric approach to fragile topology beyond symmetry indicators. *Phys. Rev. B*, 102:115135, Sep 2020.

[10] Hoi Chun Po, Ashvin Vishwanath, and Haruki Watanabe. Symmetry-based indicators of band topology in the 230 space groups. *Nat. Commun*, 8(1):50, 2017.

[11] A. J. Heeger, S. Kivelson, J. R. Schrieffer, and W. P. Su. Solitons in conducting polymers. *Rev. Mod. Phys.*, 60:781–850, Jul 1988.

[12] D. J. Thouless, M. Kohmoto, M. P. Nightingale, and M. den Nijs. Quantized hall conductance in a two-dimensional periodic potential. *Phys. Rev. Lett.*, 49:405–408, Aug 1982.

[13] K. v. Klitzing, G. Dorda, and M. Pepper. New method for high-accuracy determination of the fine-structure constant based on quantized hall resistance. *Phys. Rev. Lett.*, 45:494–497, Aug 1980.

[14] Cui-Zu Chang, Jinsong Zhang, Xiao Feng, Jie Shen, Zuocheng Zhang, Minghua Guo, Kang Li, Yunbo Ou, Pang Wei, Li-Li Wang, Zhong-Qing Ji, Yang Feng, Shuaihua Ji, Xi Chen, Jinfeng Jia, Xi Dai, Zhong Fang, Shou-Cheng Zhang, Ke He, Yayu Wang, Li Lu, Xu-Cun Ma, and Qi-Kun Xue. Experimental observation of the quantum anomalous hall effect in a magnetic topological insulator. *Science*, 340(6129):167–170, 2013.

[15] Michael Victor Berry. Quantal phase factors accompanying adiabatic changes. *Proceedings of the Royal Society of London. A. Mathematical and Physical Sciences*, 392(1802):45–57, 1984.

[16] C. L. Kane and E. J. Mele. Z_2 topological order and the quantum spin hall effect. *Phys. Rev. Lett.*, 95:146802, Sep 2005.

[17] Liang Fu and C. L. Kane. Time reversal polarization and a Z_2 adiabatic spin pump. *Phys. Rev. B*, 74:195312, Nov 2006.

[18] C. L. Kane and E. J. Mele. Quantum spin hall effect in graphene. *Phys. Rev. Lett.*, 95:226801, Nov 2005.

[19] Liang Fu, C. L. Kane, and E. J. Mele. Topological insulators in three dimensions. *Phys. Rev. Lett.*, 98:106803, Mar 2007.

[20] Xiao-Liang Qi and Shou-Cheng Zhang. Topological insulators and superconductors. *Rev. Mod. Phys.*, 83:1057–1110, Oct 2011.

[21] M. Z. Hasan and C. L. Kane. Colloquium: Topological insulators. *Rev. Mod. Phys.*, 82:3045–3067, Nov 2010.

[22] Liang Fu and C. L. Kane. Topological insulators with inversion symmetry. *Phys. Rev. B*, 76:045302, Jul 2007.

[23] Xiao-Liang Qi, Taylor L. Hughes, and Shou-Cheng Zhang. Topological field theory of time-reversal invariant insulators. *Phys. Rev. B*, 78:195424, Nov 2008.

[24] Markus König, Steffen Wiedmann, Christoph Brüne, Andreas Roth, Hartmut Buhmann, Laurens W. Molenkamp, Xiao-Liang Qi, and Shou-Cheng Zhang. Quantum spin hall insulator state in hgte quantum wells. *Science*, 318(5851):766–770, 2007.

[25] D. Hsieh, D. Qian, L. Wray, Y. Xia, Y. S. Hor, R. J. Cava, and M. Z. Hasan. A topological dirac insulator in a quantum spin hall phase. *Nature*, 452(7190):970–974, Apr 2008.

[26] B. Andrei Bernevig, Taylor L. Hughes, and Shou-Cheng Zhang. Quantum spin hall effect and topological phase transition in hgte quantum wells. *Science*, 314(5806):1757–1761, 2006.

[27] Chen Fang, Matthew J. Gilbert, and B. Andrei Bernevig. Bulk topological invariants in noninteracting point group symmetric insulators. *Phys. Rev. B*, 86:115112, Sep 2012.

[28] Liang Fu. Topological crystalline insulators. *Phys. Rev. Lett.*, 106:106802, Mar 2011.

[29] Timothy H. Hsieh, Hsin Lin, Junwei Liu, Wenhui Duan, Arun Bansil, and Liang Fu. Topological crystalline insulators in the snte material class. *Nature Communications*, 3:982 EP –, 07 2012.

[30] Ching-Kai Chiu, Jeffrey C. Y. Teo, Andreas P. Schnyder, and Shinsei Ryu. Classification of topological quantum matter with symmetries. *Rev. Mod. Phys.*, 88:035005, Aug 2016.

[31] Jorrit Kruthoff, Jan de Boer, Jasper van Wezel, Charles L. Kane, and Robert-Jan Slager. Topological classification of crystalline insulators through band structure combinatorics. *Phys. Rev. X*, 7:041069, Dec 2017.

[32] Eslam Khalaf, Hoi Chun Po, Ashvin Vishwanath, and Haruki Watanabe. Symmetry indicators and anomalous surface states of topological crystalline insulators. *Phys. Rev. X*, 8:031070, Sep 2018.

[33] Seishiro Ono and Haruki Watanabe. Unified understanding of symmetry indicators for all internal symmetry classes. *Phys. Rev. B*, 98:115150, Sep 2018.

[34] Zhida Song, Tiantian Zhang, Zhong Fang, and Chen Fang. Quantitative mappings between symmetry and topology in solids. *Nature Communications*, 9(1):3530, 2018.

[35] Tiantian Zhang, Yi Jiang, Zhida Song, He Huang, Yuqing He, Zhong Fang, Hongming Weng, and Chen Fang. Catalogue of topological electronic materials. *Nature*, 566(7745):475–479, 2019.

[36] Feng Tang, Hoi Chun Po, Ashvin Vishwanath, and Xiangang Wan. Comprehensive search for topological materials using symmetry indicators. *Nature*, 566(7745):486–489, 2019.

[37] M. G. Vergniory, L. Elcoro, Claudia Felser, Nicolas Regnault, B. Andrei Bernevig, and Zhijun Wang. A complete catalogue of high-quality topological materials. *Nature*, 566(7745):480–485, 2019.

[38] A. Alexandradinata and B. Andrei Bernevig. Berry-phase description of topological crystalline insulators. *Phys. Rev. B*, 93:205104, May 2016.

[39] Alexander Lau, Jeroen van den Brink, and Carmine Ortix. Topological mirror insulators in one dimension. *Phys. Rev. B*, 94:165164, Oct 2016.

[40] Guido van Miert and Carmine Ortix. Excess charges as a probe of one-dimensional topological crystalline insulating phases. *Phys. Rev. B*, 96:235130, Dec 2017.

[41] Rui-Xing Zhang and Chao-Xing Liu. Topological magnetic crystalline insulators and corepresentation theory. *Phys. Rev. B*, 91:115317, Mar 2015.

[42] Sander H. Kooi, Guido van Miert, and Carmine Ortix. Classification of crystalline insulators without symmetry indicators: Atomic and fragile topological phases in twofold rotation symmetric systems. *Phys. Rev. B*, 100:115160, Sep 2019.

[43] Jorrit Kruthoff, Jan de Boer, and Jasper van Wezel. Topology in time-reversal symmetric crystals. *Phys. Rev. B*, 100:075116, Aug 2019.

[44] Jiabin Yu, Zhi-Da Song, and Chao-Xing Liu. Gapless criterion for crystals from effective axion field, 2020.

[45] Heqiu Li and Kai Sun. Topological insulators and higher-order topological insulators from gauge-invariant one-dimensional lines. *Phys. Rev. B*, 102:085108, Aug 2020.

[46] Rui Yu, Xiao Liang Qi, Andrei Bernevig, Zhong Fang, and Xi Dai. Equivalent expression of F_2 topological invariant for band insulators using the non-abelian berry connection. *Phys. Rev. B*, 84:075119, Aug 2011.

[47] Alexey A. Soluyanov and David Vanderbilt. Smooth gauge for topological insulators. *Phys. Rev. B*, 85:115415, Mar 2012.

[48] Frank Schindler, Ashley M. Cook, Maia G. Vergniory, Zhijun Wang, Stuart S. P. Parkin, B. Andrei Bernevig, and Titus Neupert. Higher-order topological insulators. *Sci. Adv*, 4(6), 2018.

[49] Junyeong Ahn and Bohm-Jung Yang. Symmetry representation approach to topological invariants in $C_{2z}t$-symmetric systems. *Phys. Rev. B*, 99:235125, Jun 2019.

[50] Benjamin J. Wieder and B. Andrei Bernevig. The Axion Insulator as a Pump of Fragile Topology.

[51] Motohiko Ezawa. Strong and weak second-order topological insulators with hexagonal symmetry and F_3 index. *Phys. Rev. B*, 97:241402, Jun 2018.

[52] Motohiko Ezawa. Magnetic second-order topological insulators and semimetals. *Phys. Rev. B*, 97:155305, Apr 2018.

[53] Chen Fang and Liang Fu. New classes of three-dimensional topological crystalline insulators: Nonsymmorphic and magnetic. *Phys. Rev. B*, 91:161105, Apr 2015.

[54] Guido van Miert and Carmine Ortix. Higher-order topological insulators protected by inversion and rotoinversion symmetries. *Phys. Rev. B*, 98:081110, Aug 2018.

[55] Eslam Khalaf. Higher-order topological insulators and superconductors protected by inversion symmetry. *Phys. Rev. B*, 97:205136, May 2018.

[56] Sander H. Kooi, Guido van Miert, and Carmine Ortix. Inversion-symmetry protected chiral hinge states in stacks of doped quantum hall layers. *Phys. Rev. B*, 98:245102, Dec 2018.

[57] Dumitru Călugăru, Vladimir Juričić, and Bitan Roy. Higher-order topological phases: A general principle of construction. *Phys. Rev. B*, 99:041301, Jan 2019.

[58] Wladimir A. Benalcazar, B. Andrei Bernevig, and Taylor L. Hughes. Quantized electric multipole insulators. *Science*, 357(6346):61–66, 2017.

[59] Wladimir A. Benalcazar, B. Andrei Bernevig, and Taylor L. Hughes. Electric multipole moments, topological multipole moment pumping, and chiral hinge states in crystalline insulators. *Phys. Rev. B*, 96:245115, Dec 2017.

[60] Dániel Varjas, Fernando de Juan, and Yuan-Ming Lu. Bulk invariants and topological response in insulators and superconductors with nonsymmorphic symmetries. *Phys. Rev. B*, 92:195116, Nov 2015.

[61] Motohiko Ezawa. Second-order topological insulators and loop-nodal semimetals in transition metal dichalcogenides xte2 (x = mo, w). *Sci. Rep*, 9(1):5286, 2019.

[62] Zhijun Wang, Benjamin J. Wieder, Jian Li, Binghai Yan, and B. Andrei Bernevig. Higher-order topology, monopole nodal lines, and the origin of large fermi arcs in transition metal dichalcogenides $x\mathrm{te}_2$ ($x = \mathrm{Mo}, \mathrm{W}$). *Phys. Rev. Lett.*, 123:186401, Oct 2019.

[63] Zhida Song, Zhong Fang, and Chen Fang. $(d-2)$-dimensional edge states of rotation symmetry protected topological states. *Phys. Rev. Lett.*, 119:246402, Dec 2017.

[64] Akishi Matsugatani and Haruki Watanabe. Connecting higher-order topological insulators to lower-dimensional topological insulators. *Phys. Rev. B*, 98:205129, Nov 2018.

[65] Josias Langbehn, Yang Peng, Luka Trifunovic, Felix von Oppen, and Piet W. Brouwer. Reflection-symmetric second-order topological insulators and superconductors. *Phys. Rev. Lett.*, 119:246401, Dec 2017.

[66] Changming Yue, Yuanfeng Xu, Zhida Song, Hongming Weng, Yuan-Ming Lu, Chen Fang, and Xi Dai. Symmetry-enforced chiral hinge states and surface quantum anomalous hall effect in the magnetic axion insulator bi2-xsmxse3. *Nat. Phys*, 15(6):577–581, 2019.

[67] Chen-Hsuan Hsu, Peter Stano, Jelena Klinovaja, and Daniel Loss. Majorana kramers pairs in higher-order topological insulators. *Phys. Rev. Lett.*, 121:196801, Nov 2018.

[68] Raquel Queiroz and Ady Stern. Splitting the hinge mode of higher-order topological insulators. *Phys. Rev. Lett.*, 123:036802, Jul 2019.

[69] Haoran Xue, Yahui Yang, Fei Gao, Yidong Chong, and Baile Zhang. Acoustic higher-order topological insulator on a kagome lattice. *Nat. Mater*, 18(2):108–112, 2019.

[70] Frank Schindler, Zhijun Wang, Maia G. Vergniory, Ashley M. Cook, Anil Murani, Shamashis Sengupta, Alik Yu Kasumov, Richard Deblock, Sangjun Jeon, Ilya Drozdov, Hélène Bouchiat, Sophie Guéron, Ali Yazdani, B. Andrei Bernevig, and Titus Neupert. Higher-order topology in bismuth. *Nat. Phys*, 14(9):918–924, 2018.

[71] Sayed Ali Akbar Ghorashi, Xiang Hu, Taylor L. Hughes, and Enrico Rossi. Second-order dirac superconductors and magnetic field induced majorana hinge modes. *Phys. Rev. B*, 100:020509, Jul 2019.

[72] Zhong Wang, Xiao-Liang Qi, and Shou-Cheng Zhang. Equivalent topological invariants of topological insulators. *New J. Phys*, 12(6):065007, jun 2010.

[73] Junyeong Ahn, Dongwook Kim, Youngkuk Kim, and Bohm-Jung Yang. Band topology and linking structure of nodal line semimetals with Z_2 monopole charges. *Phys. Rev. Lett.*, 121:106403, Sep 2018.

[74] Xiao-Liang Qi, Rundong Li, Jiadong Zang, and Shou-Cheng Zhang. Inducing a magnetic monopole with topological surface states. *Science*, 323(5918):1184–1187, 2009.

[75] Andrew M. Essin, Joel E. Moore, and David Vanderbilt. Magnetoelectric polarizability and axion electrodynamics in crystalline insulators. *Phys. Rev. Lett.*, 102:146805, Apr 2009.

[76] Nicodemos Varnava and David Vanderbilt. Surfaces of axion insulators. *Phys. Rev. B*, 98:245117, Dec 2018.

[77] Takahiro Fukui and Yasuhiro Hatsugai. Quantum spin hall effect in three dimensional materials: Lattice computation of z2 topological invariants and its application to bi and sb. *J. Phys. Soc. Jpn*, 76(5):053702, 2007.

[78] Alexey A. Soluyanov and David Vanderbilt. Wannier representation of F_2 topological insulators. *Phys. Rev. B*, 83:035108, Jan 2011.

[79] Heqiu Li and Kai Sun. Pfaffian formalism for higher-order topological insulators. *Phys. Rev. Lett.*, 124:036401, Jan 2020.

[80] Liang Fu, C. L. Kane, and E. J. Mele. Topological insulators in three dimensions. *Phys. Rev. Lett.*, 98:106803, Mar 2007.

[81] Shuichi Murakami. Phase transition between the quantum spin hall and insulator phases in 3d: emergence of a topological gapless phase. *New Journal of Physics*, 9(9):356–356, sep 2007.

[82] Xiangang Wan, Ari M. Turner, Ashvin Vishwanath, and Sergey Y. Savrasov. Topological semimetal and fermi-arc surface states in the electronic structure of pyrochlore iridates. *Phys. Rev. B*, 83:205101, May 2011.

[83] A. A. Burkov and Leon Balents. Weyl semimetal in a topological insulator multilayer. *Phys. Rev. Lett.*, 107:127205, Sep 2011.

[84] S. M. Young, S. Zaheer, J. C. Y. Teo, C. L. Kane, E. J. Mele, and A. M. Rappe. Dirac semimetal in three dimensions. *Phys. Rev. Lett.*, 108:140405, Apr 2012.

[85] Takahiro Morimoto and Akira Furusaki. Weyl and dirac semimetals with z_2 topological charge. *Phys. Rev. B*, 89:235127, Jun 2014.

[86] N. P. Armitage, E. J. Mele, and Ashvin Vishwanath. Weyl and dirac semimetals in three-dimensional solids. *Rev. Mod. Phys.*, 90:015001, Jan 2018.

[87] Chen Fang, Yige Chen, Hae-Young Kee, and Liang Fu. Topological nodal line semimetals with and without spin-orbital coupling. *Phys. Rev. B*, 92:081201, Aug 2015.

[88] Chen Fang, Hongming Weng, Xi Dai, and Zhong Fang. Topological nodal line semimetals. *Chinese Physics B*, 25(11):117106, nov 2016.

[89] Tomá š Bzdušek and Manfred Sigrist. Robust doubly charged nodal lines and nodal surfaces in centrosymmetric systems. *Phys. Rev. B*, 96:155105, Oct 2017.

[90] Gang Xu, Hongming Weng, Zhijun Wang, Xi Dai, and Zhong Fang. Chern semimetal and the quantized anomalous hall effect in $hgcr_2se_4$. *Phys. Rev. Lett.*, 107:186806, Oct 2011.

[91] Guang Bian, Tay-Rong Chang, Hao Zheng, Saavanth Velury, Su-Yang Xu, Titus Neupert, Ching-Kai Chiu, Shin-Ming Huang, Daniel S. Sanchez, Ilya Belopolski, Nasser Alidoust, Peng-Jen Chen, Guoqing Chang, Arun Bansil, Horng-Tay Jeng, Hsin Lin, and M. Zahid Hasan. Drumhead surface states and topological nodal-line fermions in tltase$_2$. *Phys. Rev. B*, 93:121113, Mar 2016.

[92] Heqiu Li, Chen Fang, and Kai Sun. Diagnosis of topological nodal lines with nontrivial monopole charge in the presence of rotation symmetries. *Phys. Rev. B*, 100:195308, Nov 2019.

[93] Zhida Song, Tiantian Zhang, and Chen Fang. Diagnosis for nonmagnetic topological semimetals in the absence of spin-orbital coupling. *Phys. Rev. X*, 8:031069, Sep 2018.

[94] Hoi Chun Po, Haruki Watanabe, and Ashvin Vishwanath. Fragile topology and wannier obstructions. *Phys. Rev. Lett.*, 121:126402, Sep 2018.

[95] Barry Bradlyn, Zhijun Wang, Jennifer Cano, and B. Andrei Bernevig. Disconnected elementary band representations, fragile topology, and wilson loops as topological indices: An example on the triangular lattice. *Phys. Rev. B*, 99:045140, Jan 2019.

[96] Kai Sun, Hong Yao, Eduardo Fradkin, and Steven A. Kivelson. Topological insulators and nematic phases from spontaneous symmetry breaking in 2d fermi systems with a quadratic band crossing. *Physical Review Letters*, 103(4):046811–, 07 2009.

[97] Mildred S Dresselhaus, Gene Dresselhaus, and Ado Jorio. *Group theory: application to the physics of condensed matter*. Springer, 2010.

[98] George F Koster, John Dimmock, Robert Wheeler, and Hermann Statz. *Properties of the thirty-two point groups*. The MIT Press, 1963.

[99] Xiao-Gang Wen. Colloquium: Zoo of quantum-topological phases of matter. *Rev. Mod. Phys.*, 89:041004, Dec 2017.

[100] D. C. Tsui, H. L. Stormer, and A. C. Gossard. Two-dimensional magnetotransport in the extreme quantum limit. *Phys. Rev. Lett.*, 48:1559–1562, May 1982.

[101] R. B. Laughlin. Anomalous quantum hall effect: An incompressible quantum fluid with fractionally charged excitations. *Phys. Rev. Lett.*, 50:1395–1398, May 1983.

[102] J. K. Jain. Composite-fermion approach for the fractional quantum hall effect. *Phys. Rev. Lett.*, 63:199–202, Jul 1989.

[103] Gregory Moore and Nicholas Read. Nonabelions in the fractional quantum hall effect. *Nuclear Physics B*, 360(2):362–396, 1991.

[104] N. Read and E. Rezayi. Beyond paired quantum hall states: Parafermions and incompressible states in the first excited landau level. *Phys. Rev. B*, 59:8084–8092, Mar 1999.

[105] Evelyn Tang, Jia-Wei Mei, and Xiao-Gang Wen. High-temperature fractional quantum hall states. *Phys. Rev. Lett.*, 106:236802, Jun 2011.

[106] Kai Sun, Zhengcheng Gu, Hosho Katsura, and S. Das Sarma. Nearly flatbands with nontrivial topology. *Phys. Rev. Lett.*, 106:236803, Jun 2011.

[107] Titus Neupert, Luiz Santos, Claudio Chamon, and Christopher Mudry. Fractional quantum hall states at zero magnetic field. *Phys. Rev. Lett.*, 106:236804, Jun 2011.

[108] N. Regnault and B. Andrei Bernevig. Fractional chern insulator. *Phys. Rev. X*, 1:021014, Dec 2011.

[109] D. N. Sheng, Zheng-Cheng Gu, Kai Sun, and L. Sheng. Fractional quantum hall effect in the absence of landau levels. *Nature Communications*, 2(1):389, Jul 2011.

[110] Siddharth A. Parameswaran, Rahul Roy, and Shivaji L. Sondhi. Fractional quantum Hall physics in topological flat bands. *Comptes Rendus Physique*, 14(9):816–839, November 2013.

[111] Emil J. Bergholtz and Zhao Liu. Topological flat band models and fractional chern insulators. *International Journal of Modern Physics B*, 27(24):1330017, September 2013. Publisher: World Scientific Publishing Co.

[112] Yang-Le Wu, B. Andrei Bernevig, and N. Regnault. Zoology of fractional chern insulators. *Phys. Rev. B*, 85:075116, Feb 2012.

[113] Yuan Cao, Valla Fatemi, Ahmet Demir, Shiang Fang, Spencer L. Tomarken, Jason Y. Luo, Javier D. Sanchez-Yamagishi, Kenji Watanabe, Takashi Taniguchi, Efthimios Kaxiras, Ray C. Ashoori, and Pablo Jarillo-Herrero. Correlated insulator behaviour at half-filling in magic-angle graphene superlattices. *Nature*, 556(7699):80–84, April 2018.

[114] Yuan Cao, Valla Fatemi, Shiang Fang, Kenji Watanabe, Takashi Taniguchi, Efthimios Kaxiras, and Pablo Jarillo-Herrero. Unconventional superconductivity in magic-angle graphene superlattices. *Nature*, 556(7699):43–50, April 2018.

[115] Xiaobo Lu, Petr Stepanov, Wei Yang, Ming Xie, Mohammed Ali Aamir, Ipsita Das, Carles Urgell, Kenji Watanabe, Takashi Taniguchi, Guangyu Zhang, Adrian Bachtold, Allan H. MacDonald, and Dmitri K. Efetov. Superconductors, orbital magnets and correlated states in magic-angle bilayer graphene. *Nature*, 574(7780):653–657, October 2019.

[116] Matthew Yankowitz, Shaowen Chen, Hryhoriy Polshyn, Yuxuan Zhang, K. Watanabe, T. Taniguchi, David Graf, Andrea F. Young, and Cory R. Dean. Tuning superconductivity in twisted bilayer graphene. *Science*, 363(6431):1059–1064, 2019.

[117] Alexander Kerelsky, Leo J McGilly, Dante M Kennes, Lede Xian, Matthew Yankowitz, Shaowen Chen, K Watanabe, T Taniguchi, James Hone, Cory Dean, et al. Maximized electron interactions at the magic angle in twisted bilayer graphene. *Nature*, 572(7767):95–100, 2019.

[118] Yuan Cao, Debanjan Chowdhury, Daniel Rodan-Legrain, Oriol Rubies-Bigordà, Kenji Watanabe, Takashi Taniguchi, T Senthil, and Pablo Jarillo-Herrero. Strange metal in magic-angle graphene with near planckian dissipation. *arXiv preprint arXiv:1901.03710*, 2019.

[119] Hryhoriy Polshyn, Matthew Yankowitz, Shaowen Chen, Yuxuan Zhang, K Watanabe, T Taniguchi, Cory R Dean, and Andrea F Young. Large linear-in-temperature resistivity in twisted bilayer graphene. *Nature Physics*, 15(10):1011–1016, 2019.

[120] Yonglong Xie, Biao Lian, Berthold Jäck, Xiaomeng Liu, Cheng-Li Chiu, Kenji Watanabe, Takashi Taniguchi, B Andrei Bernevig, and Ali Yazdani. Spectroscopic signatures of many-body correlations in magic-angle twisted bilayer graphene. *Nature*, 572(7767):101–105, 2019.

[121] Yuhang Jiang, Xinyuan Lai, Kenji Watanabe, Takashi Taniguchi, Kristjan Haule, Jinhai Mao, and Eva Y Andrei. Charge order and broken rotational symmetry in magic-angle twisted bilayer graphene. *Nature*, 573(7772):91–95, 2019.

[122] Youngjoon Choi, Jeannette Kemmer, Yang Peng, Alex Thomson, Harpreet Arora, Robert Polski, Yiran Zhang, Hechen Ren, Jason Alicea, Gil Refael, et al. Electronic correlations in twisted bilayer graphene near the magic angle. *Nature Physics*, 15(11):1174–1180, 2019.

[123] U. Zondiner, A. Rozen, D. Rodan-Legrain, Y. Cao, R. Queiroz, T. Taniguchi, K. Watanabe, Y. Oreg, F. von Oppen, Ady Stern, E. Berg, P. Jarillo-Herrero, and S. Ilani. Cascade of phase transitions and Dirac revivals in magic-angle graphene. *Nature*, 582(7811):203–208, June 2020. Number: 7811 Publisher: Nature Publishing Group.

[124] Dillon Wong, Kevin P. Nuckolls, Myungchul Oh, Biao Lian, Yonglong Xie, Sangjun Jeon, Kenji Watanabe, Takashi Taniguchi, B. Andrei Bernevig, and Ali Yazdani. Cascade of electronic transitions in magic-angle twisted bilayer graphene. *Nature*, 582(7811):198–202, June 2020. Number: 7811 Publisher: Nature Publishing Group.

[125] Kevin P. Nuckolls, Myungchul Oh, Dillon Wong, Biao Lian, Kenji Watanabe, Takashi Taniguchi, B. Andrei Bernevig, and Ali Yazdani. Strongly correlated Chern insulators in magic-angle twisted bilayer graphene. *Nature*, 588(7839):610–615, December 2020. Number: 7839 Publisher: Nature Publishing Group.

[126] Minhao He, Yuhao Li, Jiaqi Cai, Yang Liu, K. Watanabe, T. Taniguchi, Xiaodong Xu, and Matthew Yankowitz. Symmetry breaking in twisted double bilayer graphene. *Nature Physics*, pages 1–5, September 2020. Publisher: Nature Publishing Group.

[127] Xiaomeng Liu, Zeyu Hao, Eslam Khalaf, Jong Yeon Lee, Yuval Ronen, Hyobin Yoo, Danial Haei Najafabadi, Kenji Watanabe, Takashi Taniguchi, Ashvin Vishwanath, and Philip Kim. Tunable spin-polarized correlated states in twisted double bilayer graphene. *Nature*, 583(7815):221–225, July 2020. Number: 7815 Publisher: Nature Publishing Group.

[128] Emma C. Regan, Danqing Wang, Chenhao Jin, M. Iqbal Bakti Utama, Beini Gao, Xin Wei, Sihan Zhao, Wenyu Zhao, Zuocheng Zhang, Kentaro Yumigeta, Mark Blei, Johan D. Carlström, Kenji Watanabe, Takashi Taniguchi, Sefaattin Tongay, Michael Crommie, Alex Zettl, and Feng Wang. Mott and generalized Wigner crystal states in WSe 2 /WS 2 moiré superlattices. *Nature*, 579(7799):359–363, March 2020. Number: 7799 Publisher: Nature Publishing Group.

[129] Lei Wang, En-Min Shih, Augusto Ghiotto, Lede Xian, Daniel A. Rhodes, Cheng Tan, Martin Claassen, Dante M. Kennes, Yusong Bai, Bumho Kim, Kenji Watanabe, Takashi Taniguchi, Xiaoyang Zhu, James Hone, Angel Rubio, Abhay N. Pasupathy, and Cory R. Dean. Correlated electronic phases in twisted bilayer transition metal dichalcogenides. *Nature Materials*, 19(8):861–866, August 2020. Number: 8 Publisher: Nature Publishing Group.

[130] Ming Xie and A. H. MacDonald. Nature of the correlated insulator states in twisted bilayer graphene. *Phys. Rev. Lett.*, 124:097601, Mar 2020.

[131] Fengcheng Wu and Sankar Das Sarma. Collective excitations of quantum anomalous hall ferromagnets in twisted bilayer graphene. *Phys. Rev. Lett.*, 124:046403, Jan 2020.

[132] Ying Su and Shi-Zeng Lin. Current-induced reversal of anomalous hall conductance in twisted bilayer graphene. *Phys. Rev. Lett.*, 125:226401, Nov 2020.

[133] Ya-Hui Zhang, Dan Mao, Yuan Cao, Pablo Jarillo-Herrero, and T. Senthil. Nearly flat chern bands in moiré superlattices. *Phys. Rev. B*, 99:075127, Feb 2019.

[134] Cécile Repellin, Zhihuan Dong, Ya-Hui Zhang, and T. Senthil. Ferromagnetism in narrow bands of moiré superlattices. *Phys. Rev. Lett.*, 124:187601, May 2020.

[135] Aaron L. Sharpe, Eli J. Fox, Arthur W. Barnard, Joe Finney, Kenji Watanabe, Takashi Taniguchi, M. A. Kastner, and David Goldhaber-Gordon. Emergent ferromagnetism near three-quarters filling in twisted bilayer graphene. *Science*, 365(6453):605–608, 2019.

[136] M. Serlin, C. L. Tschirhart, H. Polshyn, Y. Zhang, J. Zhu, K. Watanabe, T. Taniguchi, L. Balents, and A. F. Young. Intrinsic quantized anomalous hall effect in a moiré heterostructure. *Science*, 2019.

[137] Guorui Chen, Aaron L Sharpe, Eli J Fox, Ya-Hui Zhang, Shaoxin Wang, Lili Jiang, Bosai Lyu, Hongyuan Li, Kenji Watanabe, Takashi Taniguchi, et al. Tunable correlated chern insulator and ferromagnetism in trilayer graphene/boron nitride moir\'e superlattice. *arXiv preprint arXiv:1905.06535*, 2019.

[138] Patrick J. Ledwith, Grigory Tarnopolsky, Eslam Khalaf, and Ashvin Vishwanath. Fractional chern insulator states in twisted bilayer graphene: An analytical approach. *Phys. Rev. Research*, 2:023237, May 2020.

[139] Cécile Repellin and T. Senthil. Chern bands of twisted bilayer graphene: Fractional chern insulators and spin phase transition. *Phys. Rev. Research*, 2:023238, May 2020.

[140] Ahmed Abouelkomsan, Zhao Liu, and Emil J. Bergholtz. Particle-hole duality, emergent fermi liquids, and fractional chern insulators in moiré flatbands. *Phys. Rev. Lett.*, 124:106803, Mar 2020.

[141] Zhao Liu, Ahmed Abouelkomsan, and Emil J. Bergholtz. Gate-Tunable Fractional Chern Insulators in Twisted Double Bilayer Graphene. *arXiv:2004.09522 [cond-mat]*, April 2020. arXiv: 2004.09522.

[142] Patrick Wilhelm, Thomas C. Lang, and Andreas M. Läuchli. Interplay of Fractional Chern Insulator and Charge-Density-Wave Phases in Twisted Bilayer Graphene. *arXiv:2012.09829 [cond-mat]*, December 2020. arXiv: 2012.09829.

[143] Heqiu Li, Umesh Kumar, Kai Sun, and Shi-Zeng Lin. Spontaneous fractional chern insulators in transition metal dichalcogenides moire superlattices, 2021.

[144] Yang Xu, Song Liu, Daniel A. Rhodes, Kenji Watanabe, Takashi Taniguchi, James Hone, Veit Elser, Kin Fai Mak, and Jie Shan. Correlated insulating states at fractional fillings of moiré superlattices. *Nature*, 587(7833):214–218, November 2020. Number: 7833 Publisher: Nature Publishing Group.

[145] Chenhao Jin, Zui Tao, Tingxin Li, Yang Xu, Yanhao Tang, Jiacheng Zhu, Song Liu, Kenji Watanabe, Takashi Taniguchi, James C. Hone, Liang Fu, Jie Shan, and Kin Fai Mak. Stripe phases in WSe2/WS2 moir\'e superlattices. *arXiv:2007.12068 [cond-mat]*, July 2020. arXiv: 2007.12068.

[146] You Zhou, Jiho Sung, Elise Brutschea, Ilya Esterlis, Yao Wang, Giovanni Scuri, Ryan J. Gelly, Hoseok Heo, Takashi Taniguchi, Kenji Watanabe, Gergely Zaránd, Mikhail D. Lukin, Philip Kim, Eugene Demler, and Hongkun Park. Signatures of bilayer Wigner crystals in a transition metal dichalcogenide heterostructure. *arXiv:2010.03037 [cond-mat]*, October 2020. arXiv: 2010.03037.

[147] Xiong Huang, Tianmeng Wang, Shengnan Miao, Chong Wang, Zhipeng Li, Zhen Lian, Takashi Taniguchi, Kenji Watanabe, Satoshi Okamoto, Di Xiao, Su-Fei Shi, and Yong-Tao Cui. Correlated Insulating States at Fractional Fillings of the WS2/WSe2 Moir\'e Lattice. *arXiv:2007.11155 [cond-mat]*, November 2020. arXiv: 2007.11155.

[148] Fengcheng Wu, Timothy Lovorn, Emanuel Tutuc, and A. H. MacDonald. Hubbard model physics in transition metal dichalcogenide moiré bands. *Phys. Rev. Lett.*, 121:026402, Jul 2018.

[149] Fengcheng Wu, Timothy Lovorn, Emanuel Tutuc, Ivar Martin, and A. H. MacDonald. Topological insulators in twisted transition metal dichalcogenide homobilayers. *Phys. Rev. Lett.*, 122:086402, Feb 2019.

[150] Michael Levin and Ady Stern. Fractional topological insulators. *Phys. Rev. Lett.*, 103:196803, Nov 2009.

[151] Mark Hillery and Leonard D. Mlodinow. Quantization of electrodynamics in nonlinear dielectric media. *Phys. Rev. A*, 30:1860–1865, Oct 1984.

[152] Di Xiao, Gui-Bin Liu, Wanxiang Feng, Xiaodong Xu, and Wang Yao. Coupled spin and valley physics in monolayers of mos_2 and other group-vi dichalcogenides. *Phys. Rev. Lett.*, 108:196802, May 2012.

[153] Rafi Bistritzer and Allan H. MacDonald. Moiré bands in twisted double-layer graphene. *PNAS*, 108(30):12233–12237, July 2011.

[154] Jong Yeon Lee, Eslam Khalaf, Shang Liu, Xiaomeng Liu, Zeyu Hao, Philip Kim, and Ashvin Vishwanath. Theory of correlated insulating behaviour and spin-triplet superconductivity in twisted double bilayer graphene. *Nature Communications*, 10(1):5333, Nov 2019.

[155] Nick Bultinck, Shubhayu Chatterjee, and Michael P. Zaletel. Mechanism for anomalous hall ferromagnetism in twisted bilayer graphene. *Phys. Rev. Lett.*, 124:166601, Apr 2020.

[156] Ady Stern. Fractional Topological Insulators: A Pedagogical Review. *Annual Review of Condensed Matter Physics*, 7(1):349–368, March 2016. Publisher: Annual Reviews.

[157] B. Andrei Bernevig and N. Regnault. Emergent many-body translational symmetries of abelian and non-abelian fractionally filled topological insulators. *Phys. Rev. B*, 85:075128, Feb 2012.

[158] S. L. Sondhi, A. Karlhede, S. A. Kivelson, and E. H. Rezayi. Skyrmions and the crossover from the integer to fractional quantum hall effect at small zeeman energies. *Phys. Rev. B*, 47:16419–16426, Jun 1993.

[159] Shubhayu Chatterjee, Matteo Ippoliti, and Michael P. Zaletel. Skyrmion Superconductivity: DMRG evidence for a topological route to superconductivity. *arXiv:2010.01144 [cond-mat]*, October 2020. arXiv: 2010.01144.

[160] Chetan Nayak, Steven H. Simon, Ady Stern, Michael Freedman, and Sankar Das Sarma. Non-abelian anyons and topological quantum computation. *Rev. Mod. Phys.*, 80:1083–1159, Sep 2008.

[161] Krishna Kumar, Kai Sun, and Eduardo Fradkin. Chern-simons theory of magnetization plateaus of the spin-$\frac{1}{2}$ quantum xxz heisenberg model on the kagome lattice. *Phys. Rev. B*, 90:174409, Nov 2014.

[162] Krishna Kumar, Kai Sun, and Eduardo Fradkin. Chiral spin liquids on the kagome lattice. *Phys. Rev. B*, 92:094433, Sep 2015.

[163] W. Zhu, Shou-Shu Gong, Tian-Sheng Zeng, Liang Fu, and D. N. Sheng. Interaction-driven spontaneous quantum hall effect on a kagome lattice. *Phys. Rev. Lett.*, 117:096402, Aug 2016.